Modelling and validation of inter-particle forces and torques for coarse-grained discrete element method

Dissertation by

Yuze HU

July 2024

For the Degree of

Doctor of Philosophy

Graduate School of Engineering,
Osaka University
Suita, Osaka, Japan

Abstract

Discrete element method (DEM) has been widely employed for the analysis of granular materials in various fields for several decades. However, the application of DEM to large-scale systems is still challenging due to its extremely high computational cost. Coarse-grain models are often used to speed-up DEM simulation in which the particle size is artificially increased. This can reduce the number of particles in the system and increase the time step interval, both of which can lead to a significant reduction of computational cost. In this study, a novel coarse-grain model is developed and validated, which is named the scaled-up particle (SUP) model.

In the SUP model, the forces and torques acting on the original particles are first estimated using the original particle parameters and variables, and then directly scaled. The scaling laws are derived in such a way that the bulk momentum change can be equivalent. The crucial aspect lies in evaluating the original particle variables, e.g., particle overlap and separation distance, from those of the coarse-grained particles, which are required to estimate the inter-particle forces and torques of the original particles. In this work, it is proposed to evaluate the particle overlap and separation distance using geometric similarity so that the same mass of the original and coarse-grained particles can be accommodated homogeneously in a fixed space, i.e., control volume. This is different from most, if not all, of the coarse-grain models in the literature. In this work, the SUP model is validated by examining the following three aspects: inter-particle force accuracy, inter-particle torque accuracy and applicability to various particle size distributions (PSDs).

To assess the accuracy of inter-particle forces, the proposed model is applied to simulate diverse systems where particles experience the contact force, capillary force and surface adhesion force. It is demonstrated that the proposed model can provide an almost identical stress-strain curve of the original particles during uniaxial compression of a packed particle bed, which is almost solely determined by the contact force. It is also shown that the proposed model can successfully capture the change of the flow regime of wet particles in a vertical mixer by increasing the surface tension and decreasing the liquid volume. Furthermore, the proposed model can reasonably replicate the original velocity distributions of cohesive particles with the Johnson-Kendall-Roberts surface adhesion forces in the same vertical mixer. These results suggest that the proposed model can be applied to various types of inter-particle forces. Finally, it is demonstrated from the periodic boundary box simulation that the critical time step interval above which the simulation becomes unstable is linearly proportional to the scale factor, i.e., the size ratio between the coarse-grained and original particles.

The accuracy of the inter-particle torques is discussed by simulating the formation of particle beds and heaps under gravity, where the coefficient of rolling resistance plays an important role. Two rolling resistance models are examined: the elastic-plastic spring-dashpot model and the constant directional torque model. It is found that the proposed model can reproduce the bulk density and angle of repose of the original particles well regardless of the rolling resistance models used. This implies the applicability of the proposed model to various types of inter-particle torques. It is also shown that the results are less sensitive to the scale factor compared to other models in the literature.

Regarding the applicability to various PSDs, the bulk density of particle beds with binary and log-normal PSDs have been simulated. It is proven that the proposed model can well capture the variation of the original bulk density caused by the size distributions.

It is concluded that the SUP model proposed in the present study is valid for a wide range of static and dynamic behaviours of granular materials.

Acknowledgements

I would like to start by acknowledging my supervisor, Professor Toshitsugu Tanaka. He welcomed me as a PhD student and has consistently supported me throughout my research and personal challenges. At each meeting, his warm smile and readiness to assist never fail to inspire me. His generous support has been instrumental in helping me navigate the challenges of studying and living in a foreign country on my own. I feel fortunate to have met Tanaka-sensei and to have had the opportunity to be his student.

Then, I would like to express my gratitude to Dr. Kimiaki Washino, who has provided me with a lot of advice and valuable comments over the past four years. He continued to provide me with extremely detailed guidance for my research, and I also learned from him the importance of being meticulous and serious as a researcher. The opportunity to meet Washino-sensei and learn from him has been incredibly fortunate for me.

I am grateful to Dr. Takuya Tsuji for welcoming me into the laboratory and for his insightful discussions and comments on my research. Although we did not communicate frequently, his politeness, gentleness, and professionalism were evident through his thoughtful comments and suggestions.

In addition to expressing my deep gratitude towards my supervisor, I would like to extend my appreciation to the members of the dissertation committees, Professor Akihiro Nakatani and Professor Shintaro Takeuchi, for their insightful comments and questions that polished my understanding to continuum mechanics and fluid physics.

I am grateful to JST (JST SPRING, Grant No. JPMJSP2138) for the financial support provided for this work. This research received partial support from computational resources offered by the Research Institute for Information Technology at Kyushu University and the supercomputer of ACCMS at Kyoto University.

I would like to express my sincere appreciation to all the friendly members of the

Tanaka & Tsuji Laboratory at Osaka University. Your support and assistance have been invaluable to me. Additionally, I extend my heartfelt thanks to all the friends who have accompanied me on this journey, both offline and online. Your companionship and shared experiences have brought joy and comfort during the most challenging times. Whether we were together in person or connected through digital means, your friendship has been a source of strength and encouragement to me.

Finally, I would like to extend my deepest and most heartfelt gratitude to my parents and all of my family members for their unwavering support and encouragement throughout these years.

List of publications

This dissertation is the original work conducted by Yuze Hu under the supervision of Professor Toshitsugu Tanaka and Dr. Kimiaki Washino. As a result of this research, two journal articles have been published, along with three oral presentations and one poster presentation at conferences.

Journal articles:

- Yuze Hu, Ei L. Chan, Takuya Tsuji, Toshitsugu Tanaka, Kimiaki Washino, Geometric similarity on interparticle force evaluation for scaled-up DEM particles, Powder Technology, Volume 404, 2022, 117483.

- Yuze Hu, Ei L. Chan, Jun-ichi Watanabe, Masahiro Takezawa, Takuya Tsuji, Toshitsugu Tanaka, Kimiaki Washino, Inter-particle torque scaling in coarse grained DEM with rolling resistance and particle size distributions, Powder Technology, Volume 438, 2024, 119612.

Oral presentations in conferences: (Yuze Hu is the presenter)

- Yuze Hu, Kimiaki Washino, Takuya Tsuji and Toshitsugu Tanaka, "Study on the evaluation of particle interaction forces in coarse-grained DEM models", *Proceedings of 2021 SPTJ Summer Symposium*, Volume 56th, pp. 24-25, Oct. 2021.

- Yuze Hu, Ei L. Chan, Kimiaki Washino, Takuya Tsuji and Toshitsugu Tanaka, "Geometric similarity for interparticle force evaluation in upscaled discrete particle simulation", *The 8th Asian Particle Technology Symposium*, Session 2[R3]01, Oct. 2021.

- Yuze Hu, Toshitsugu Tanaka, Takuya Tsuji, Kimiaki Washino, "Scaling of inter-particle torques in coarse-grained DEM with rolling resistance and particle size distributions", *Proceedings of 2024 SPTJ Spring Meeting*, pp. 104-105, May. 2024.

Poster presentation in conference: (Yuze Hu is the presenter)

- Yuze Hu, Kimiaki Washino, Takuya Tsuji and Toshitsugu Tanaka, "Study on the scaling law of rolling resistance in coarse-grained DEM models", *Proceedings of 2022 SPTJ Autumn Meeting*, Volume 2022, pp. 94-95, Dec. 2022.

Contents

List of Figures

List of Tables

Chapter 1

Introduction

1.1 Background

1.1.1 Granular materials

Granular materials are the second most manipulated material in industry after water [1]. They are ubiquitous in nature and play a crucial role in various industries, including food, mining, agriculture, as well as pharmaceutical industries [2]. In the chemical industry, it has been estimated that approximately half of the products and three-quarters of the raw materials are in granular form [3]. They are also fundamental to various phenomena in the fields of civil and geotechnical engineering, such as soil liquefaction [4], erosion [5, 6], sediment transport [7, 8, 9], landslides [10, 11, 12, 13], and debris flow [14, 15, 16].

Furthermore, the understanding of powders characteristics is crucial for effective control and optimisation of industrial processes. For instance, in the pharmaceutical industry, powder technology plays a crucial role that directly impacts drug development, manufacturing processes, and final product quality control. The physical and chemical properties of powders, such as particle size, shape, surface energy, and flowability, significantly affect the stability, bioavailability, and release characteristics of drugs [17, 18, 19, 20, 21].

Granular materials can exhibit either solid-like or fluid-like behaviour. Similar to liquids, granular materials can conform to the shape of their container. However, granular materials also exhibit solid-like characteristics when stacked together. Granular materials

are typically classified by their macroscopic properties, such as flowability, the angle of repose, and bulk density. These macroscopic properties are generally influenced by various microscopic characteristics of individual particles, as mentioned, which include particle size, shape, and surface conditions.

In engineering applications, phenomena can be classified based on their length scales, which encompass the macroscopic level (centimetres to metres), the microscopic level (micrometres to centimetres), and the molecular level (1 to 1,000 nanometres) [22]. It is worth noting that the majority of granular materials commonly used in laboratory experiments typically range in size from approximately 100 to 3000 μm [23]. The length scale of particles is also widely recognised as a crucial property of granular materials, and various classifications based on particle size have been proposed [3]. For example, Richards [24, 25] proposed a classification for granular materials based on their mean particle sizes, as shown in Table 1.1. The granular material investigated and discussed in this study roughly falls within the size range between the granular powder and granular solid listed in Table 1.1, i.e. 10 to 3000 μm.

Table 1.1: The granular material classifications according to mean particle size [24, 25, 3].

Particle size range	Name of material	Name of individual component
0.1 μm - 1.0 μm	Ultra-fine powder	Ultra-fine particle
1.0 μm - 10 μm	Superfine powder	Superfine particle
10 μm - 100 μm	Granular powder	Granular particle
0.1 mm - 3.0 mm	Granular solid	Granule
3.0 mm - 10 mm	Broken solid	Grain

The flowability of granular materials in fluidisation process is significantly influenced by the average particle size, making it a good example for studying this phenomenon. Based on the difference in density between particles and fluid ($\rho_{\mathrm{p}} - \rho_{\mathrm{f}}$), as well as the mean particle size (d_{sv}), Geldart [26] classified granular solids into four groups, as shown in Figure 1.1. The difference of fluidisation behaviour across different groups is significant, which is illustrated in Figure 1.2 [26, 27]. The smallest Group C particles exhibit limited

fluidisation due to their high cohesion, which is attributed to their small size and makes them the most difficult to fluidise. The particles in Group A and the larger particles in Group B exhibit good fluidisation characteristics, although their fluidisation behaviours are different from each other. Particles in Group A exhibit dense phase expansion after minimum fluidisation and before the onset of bubbles. Group B particles form bubbles at the onset of minimum fluidisation. The largest particles, classified as Group D, exhibit a spouting behaviour rather than achieving complete fluidisation. These Group D particles, being the largest in size, tend to form stable spouts that are characteristic of spouting fluidised beds.

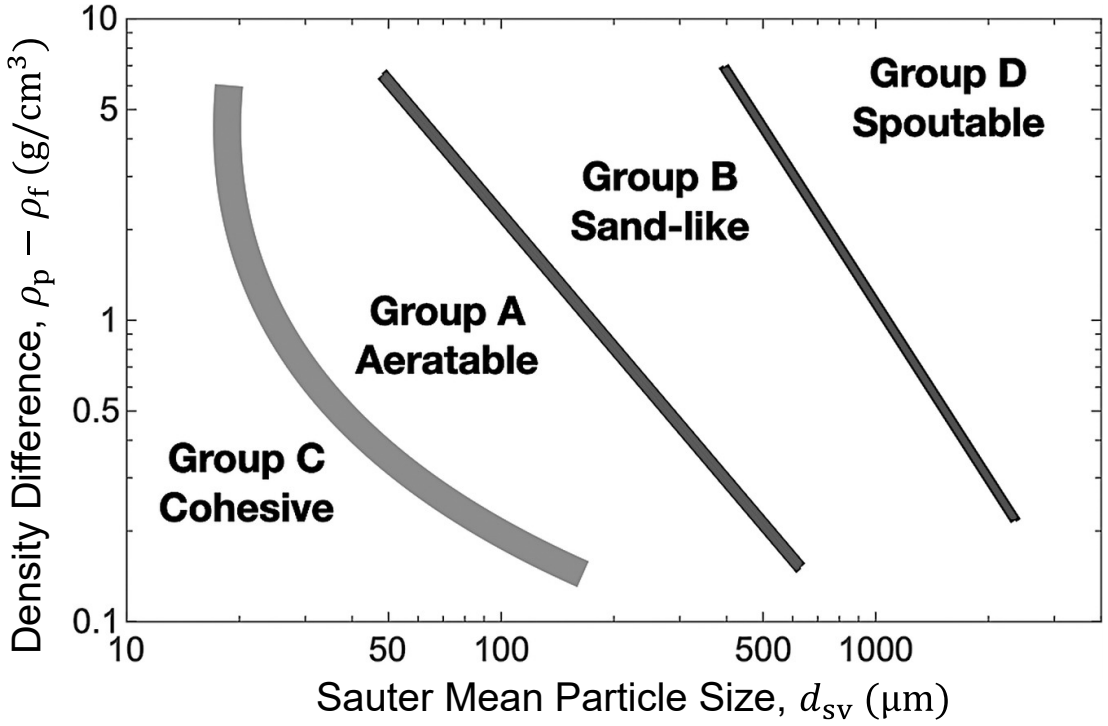

Figure 1.1: The Geldart's classification [26] of particle fluidisation (excerpt from [27]).

The flow regime and average particle size in the mentioned fluidisation instances are highly correlated, which indicate the analysis of bulk particles behaviour is challenging. Here, the definition of the mentioned term "bulk particles" can be briefly explained as follows: A bulk solid is composed of numerous individual particles [28, 29], in which the solid particles can be called bulk particles [28].

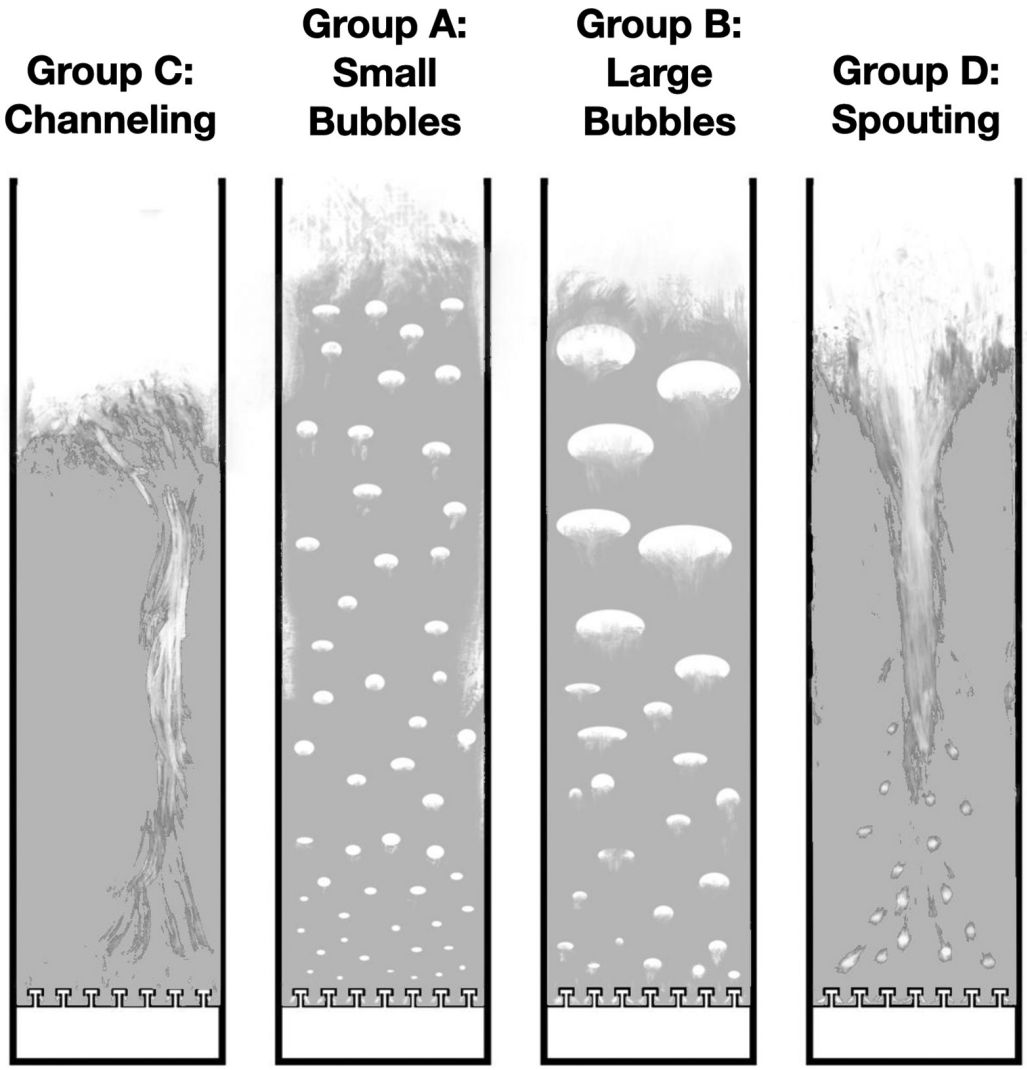

Figure 1.2: The illustration shows the fluidised bed in Groups A, B, C, and D of Geldart's classification [26] (excerpt from [27]).

The flow of granular material is considered to lack scale separation [30], which makes it more complex than the flow of conventional fluids, such as liquid and gas. Comparing the flow of granular materials with that of conventional fluids helps us understand the concept. A significant difference between granular flow and the flow of conventional fluids comes from the size difference between granular particles and fluid molecules. For a liquid, e.g. water, there can be eight, nine or even more orders of magnitude difference between the flow scale and the size of individual molecules [31]. In contrast, with much smaller size separations, the temporal and spatial scales of individual granular particles are usually comparable to the granular bulk flow of particles, where granular particles usually forms rigid regions under the effect of external stress [32, 33]. Here, the use of "bulk" in term "bulk flow" emphasises the collective movement of particles as a whole rather than their individual or random movements [34, 32, 33].

The size of granular particles falls within the range between microscopic and macroscopic, which makes the influence of conventional temperature on particle motion negligible while dynamical effects become more significant [35]. Consequently, the interactions among particles, such as energy dissipation due to surface friction and inelastic collisions, assume greater significance and cannot be ignored. The micro properties of particles govern the interactions between individual particles, which influence the behaviour of granular material at a macroscopic level. This phenomenon is commonly referred to as the micro-macro transition in granular particle behaviour [36, 37, 38, 39].

1.1.2 Micro-macro transition of granular materials

The micro-macro transition, which refers to the correlation between particle-level interactions and macroscopic behaviours of granular materials, remains poorly understood and requires further investigation. Various microscopic factors at the particle level can influence the macroscopic behaviours of bulk particles. This section introduces three crucial microscopic factors, namely inter-particle forces, rolling resistance, and particle size

distributions, and explains how they influence the macroscopic behaviour.

1.1.2.1 Inter-particle forces

Various inter-particle forces can influence the motion of individual particles and thereby macroscopic motion of granular materials, such as contact forces [40, 41], van der Waals forces [42, 43, 44, 45], electrostatic forces [46, 47, 48, 49], and liquid bridge forces [50, 51, 52, 53]. The mentioned inter-particle forces are briefly introduced as follows:

- **Contact forces**: Contact forces result from the interactions of electrons on or near the surfaces of objects [54]. In the length scale of granular materials, contact forces between particles can be regarded as originating from surface deformations at the points of contact [55]. Depending on the material of the contact surface, various theories can be used to evaluate the contact forces between particles. The Hertz contact theory is a typical example, which is based on the analysis of deformation in smooth, elastic spheres under frictional contact and predicts both normal and shear forces [40].

- **van der Waals forces**: van der Waals force at the atom scale arise from transient shifts in electron density, resulting in charge imbalances that can attract or repel neighbouring atoms. The more detailed information of the origin of van der Waals forces can be found in literature [43, 56]. At the scale that particle diameter is less than 50 microns, van der Waals forces are regarded as the primary force of adhesion. These van der Waals forces can be increased as a result of particle and/or surface deformations, which increase the contact area of particles [57]. The Johnson-Kendall-Roberts (JKR) contact theory takes it into consideration and describes the adhesion contact between soft and slightly deformable materials [44, 58, 45].

- **Electrostatic forces**: In the process of handling granular materials, triboelectrification is a significant surface phenomenon [47, 49]. The relative movement of

particles and their collisions with surfaces, which creates conditions for the generation of electrostatic charge. Charged particles set up electrostatic fields which influence particle trajectories and dynamics [47]. The electrostatic attraction forces among charged particles can result in the adhesion of granular materials on the walls of processing equipment and the agglomeration of particles [46, 48, 49].

- **Liquid bridge forces**: In a humid environment, each particle is regarded as surrounded by a film of liquid. The liquid bridge force arises when a liquid forms a bridge between two solid surfaces, which is regarded as one kind of important cohesion force among wet particles [50, 51, 52, 53]. The total liquid bridge force can be expressed as the sum of the liquid bridge viscous forces and capillary force. The presence of a liquid film results in an increased frictional force between the particles, which is caused by the higher viscosity of the liquid within the contact region compared to the surrounding gas [59]. The viscous forces of a liquid bridge are particularly significant when the viscosity of the liquid is high, thus greatly impacting the flowability of particles [60]. The computation of viscous force of liquid bridge has been extensively discussed in previous studies by Washino et al. [61, 62]. On the other hand, the capillary force is a sum of the surface tension along with three-phase contact line and the force due to the Laplace pressure [63, 64]. The method for evaluating the capillary force can be found in Section 2.3.2.1, specifically in Equation (2.31).

It is a typical instance of the micro-macro transition of granular materials that inter-particle cohesion forces can cause particle lumps and greatly change the flow regime of particles. Figure 1.3 illustrates the comparison of granular flow with cohesive and non-cohesive particles. The lumps can be observed in the snapshot of cohesive particles, whereas they cannot be seen in the case of non-cohesive particles. Understanding such influences from inter-particle forces to the macroscopic behaviour of granular materials is

crucial for optimising the handling process of granular materials.

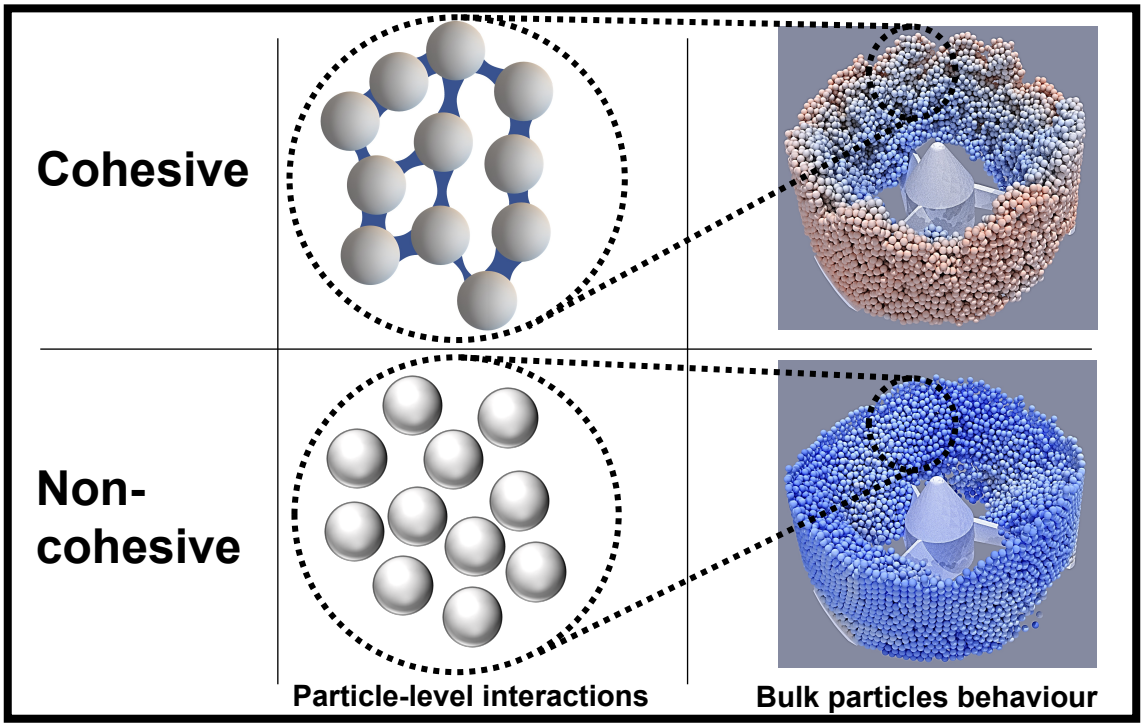

Figure 1.3: The inter-particle forces (cohesion force) influence the behaviour of bulk particles. The colours represent particle velocity, with red indicating the higher velocity and blue indicating the lower velocity.

1.1.2.2 Rolling resistance

Rolling resistance is a typical mechanism for the dissipation of rotational energy of granular materials at the particle-level scale, which is also considered as a torque that impedes the attempt to roll one body on the surface of another body [65]. The rolling resistance can arise from various sources, including micro-slip and friction on the contact surface [55, 66, 67], plastic deformation around the contact point [55, 68], viscous hysteresis [68, 69, 70, 71, 72, 73, 74, 75, 76], and surface adhesion [77, 78, 65, 79, 80, 81]. The mechanisms of rolling resistance have been well reviewed in the literature [82], and are briefly introduced as follows:

- **Micro-slip**: Micro-slip (or creep) at the interface may occur when the rolling bodies have different elastic constants. The resistance of micro-slip depends on both the difference between the elastic constants and the sliding friction coefficient. The micro-slip rolling resistance is typically very small for most material pairs. Micro-slip can also occur due to differences in curvatures at the contact point, but this is usually negligible [55].

- **Plastic deformation**: As shown in Figure 1.4, plastic deformation is a significant source of energy dissipation during the rolling contact of particles, making it a crucial factor in rolling resistance. As shown in Figure 1.5, the torque of rolling resistance primarily arises from the plastic deformation of materials ahead of the sphere, where the deformed surface supports the front half of the contact circle with the sphere [68]. Rather than at the interface, the plastic deformation energy dissipation usually occurs inside the solid material, specifically at the location where maximum shear stress is generated by contact.

- **Viscous hysteresis**: Viscous hysteresis is a significant energy dissipation mechanism during rolling contact between viscoelastic particles. Viscoelastic materials, e.g. rubber, absorb more energy during loading than they release during unloading.

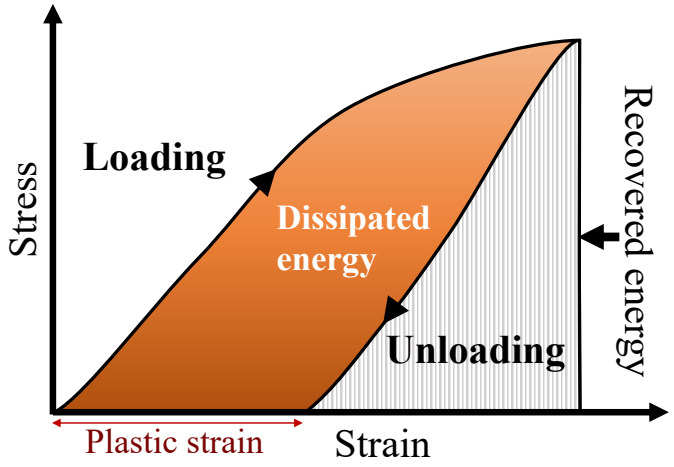

Figure 1.4: The stress-strain curve for loading and unloading plastic materials. After unloading, the plastic strain is retained, while the orange-coloured area indicates energy dissipation.

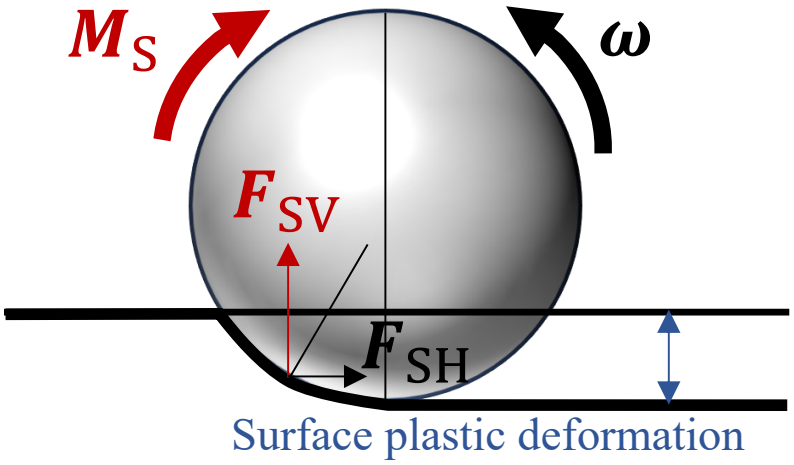

Figure 1.5: The plastic deformed surface supports the front half of the contact circle. $\boldsymbol{F}_{\mathrm{SV}}$ indicates the support force in the vertical direction, and $\boldsymbol{F}_{\mathrm{SH}}$ is in the horizontal direction. $\boldsymbol{M}_{\mathrm{S}}$ is the torque arising from the support force, which opposes the angular velocity $\boldsymbol{\omega}$ at that moment.

Figure 1.6 (a) illustrates the load cycle of viscoelastic materials, where the area enclosed by loading and unloading paths on the stress-strain graph is referred to as the hysteresis area. The stresses in the loading region are greater than the stresses in the unloading region for the same strain. As depicted in Figure 1.6 (b), the rotation induces an asymmetric stress distribution on the contact surfaces of the particle due to viscous hysteresis, which generates a torque reversing in the direction of the angular velocity. The energy lost during deformation can be considerable and can be significantly influenced by temperature and deformation rate [70, 75].

- **Surface adhesion**: The adhesion rolling resistant torque, as shown in Figure 1.7, is mainly attributed to the asymmetric contact area of adhesion contact [65].

The rolling resistance of individual particles, as shown in Figure 1.8, can influence the overall flowability of bulk granular materials significantly. The high rolling resistance may lead to the formation of lumps or agglomerates within the bulk particles.

1.1.2.3 Particle size distributions

The size of particles is a crucial microscopic characteristic. The real granular materials are often non-uniform in size and have particle size distributions (PSDs), which can make particle interactions even more complex. It has been found that the packing density of a multi-particle system increases when the particle size distribution is extended [83], and this change in packing state also influences the stress distribution [84, 85].

As shown in Figure 1.9, particles with a wide size distribution typically exhibit higher bulk density than mono-dispersed particles, as small particles can fill in the spaces between larger particles. Size segregation [86, 87, 88, 89, 90] may occur for various reasons, such as the percolation of small particles into the void between large particles [89, 90] and the different kinetic energy dissipation rates of particles with different sizes [86]. While this

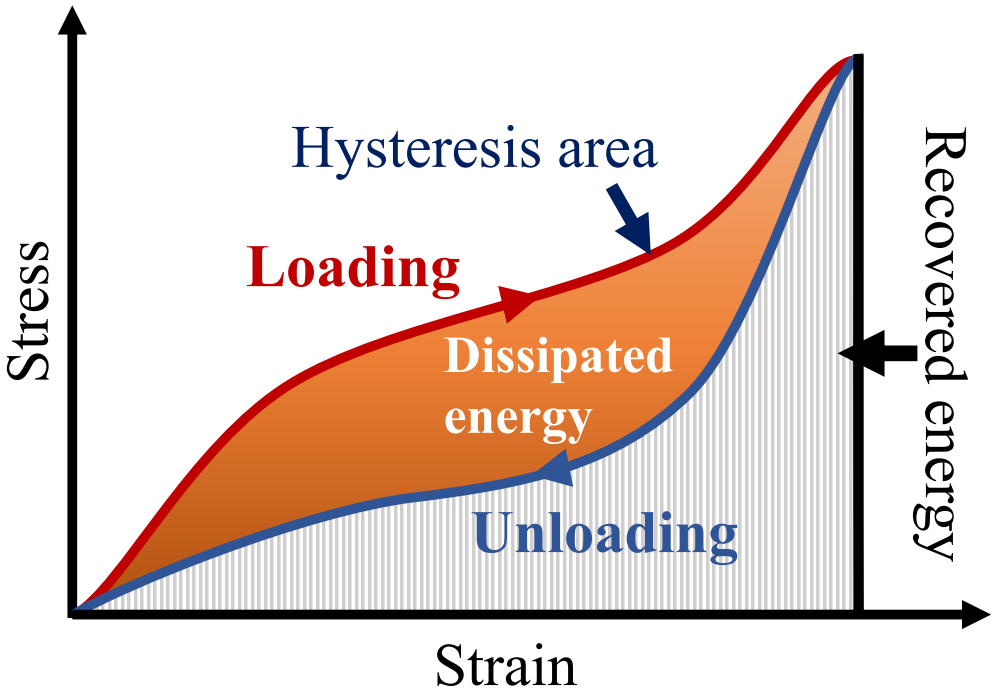

(a) The energy dissipation of viscous hysteresis.

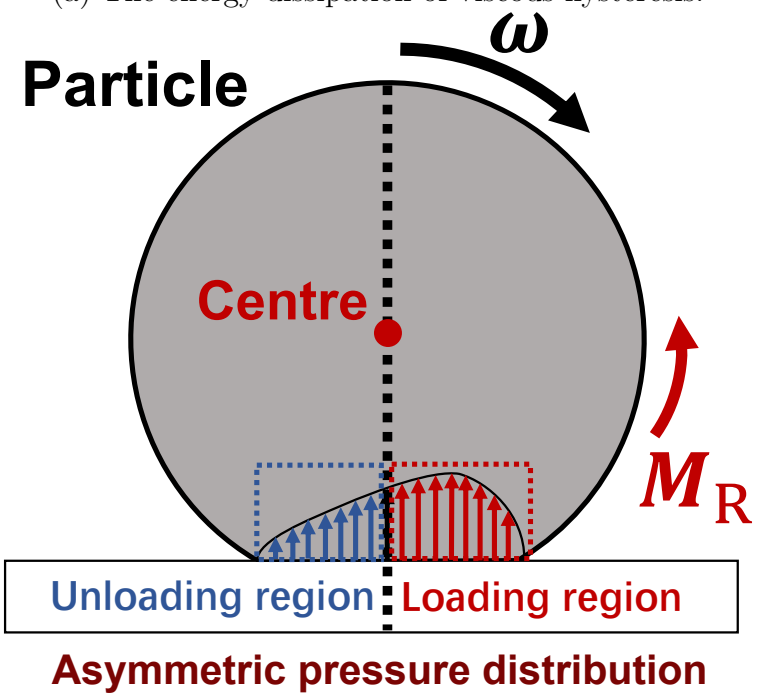

(b) The asymmetric pressure distribution between the loading and unloading regions.

Figure 1.6: The load loop of viscoelastic materials, where the orange area indicates the dissipated energy of viscous hysteresis. The stress on the loading path is higher than the unloading path with the same strain (a). It results in the asymmetric pressure distributions between loading region and unloading region, and generates the torque of rolling resistance $\boldsymbol{M}_{\mathrm{R}}$ (b).

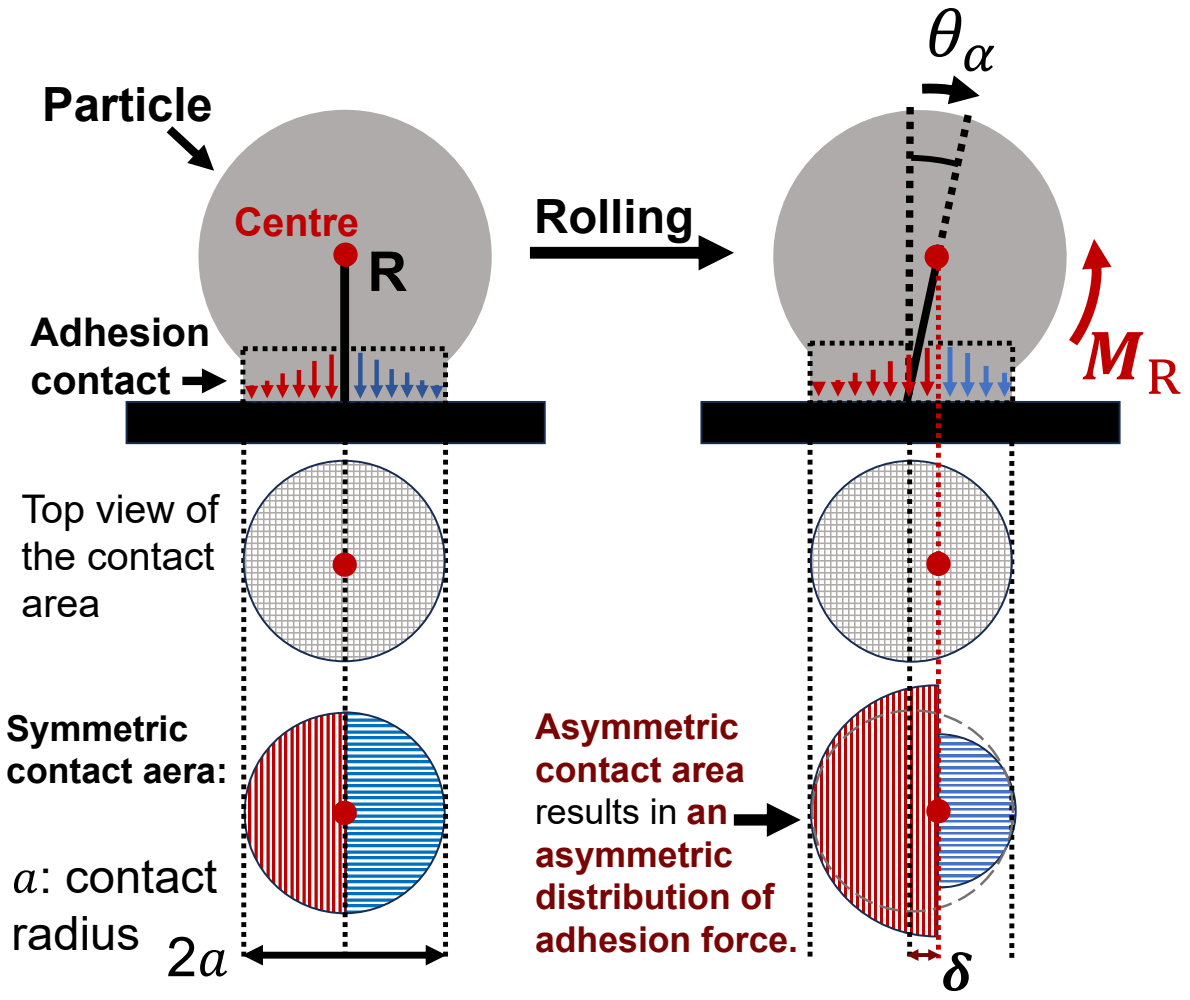

Figure 1.7: The torque of rolling resistance arises from the asymmetric distribution of adhesion forces, which explains the mechanism of adhesion rolling resistance. The red points indicate the centre of the particle, M_{R} represents the torque of rolling resistance, a is the radius of the adhesion contact area, θ_α denotes angular motion, and $\delta = R\theta_\alpha$ represents the distance moved by the contact point. The asymmetric contact in the figure is an exaggerated illustration. The actual δ is relatively small, and the distribution of the asymmetric contact area on both sides of the axis will not be discontinued.

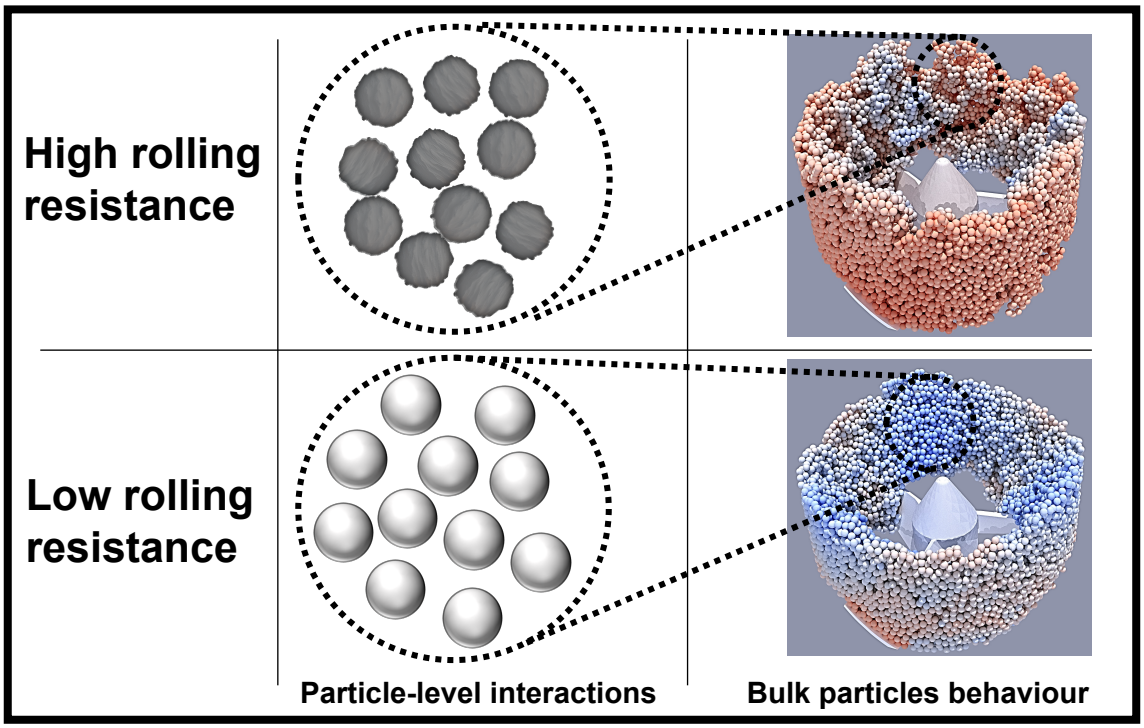

Figure 1.8: The behaviour of bulk particles is influenced by particle rolling resistance. The colours represent particle velocity, with red indicating the higher velocity and blue indicating the lower velocity.

phenomenon is undesirable in many applications, it is also actively utilised for particle separation and recycling. A deeper understanding of the microscopic mechanism of PSDs can help to improve the processes related to particle segregation, mixing, compression, and so forth.

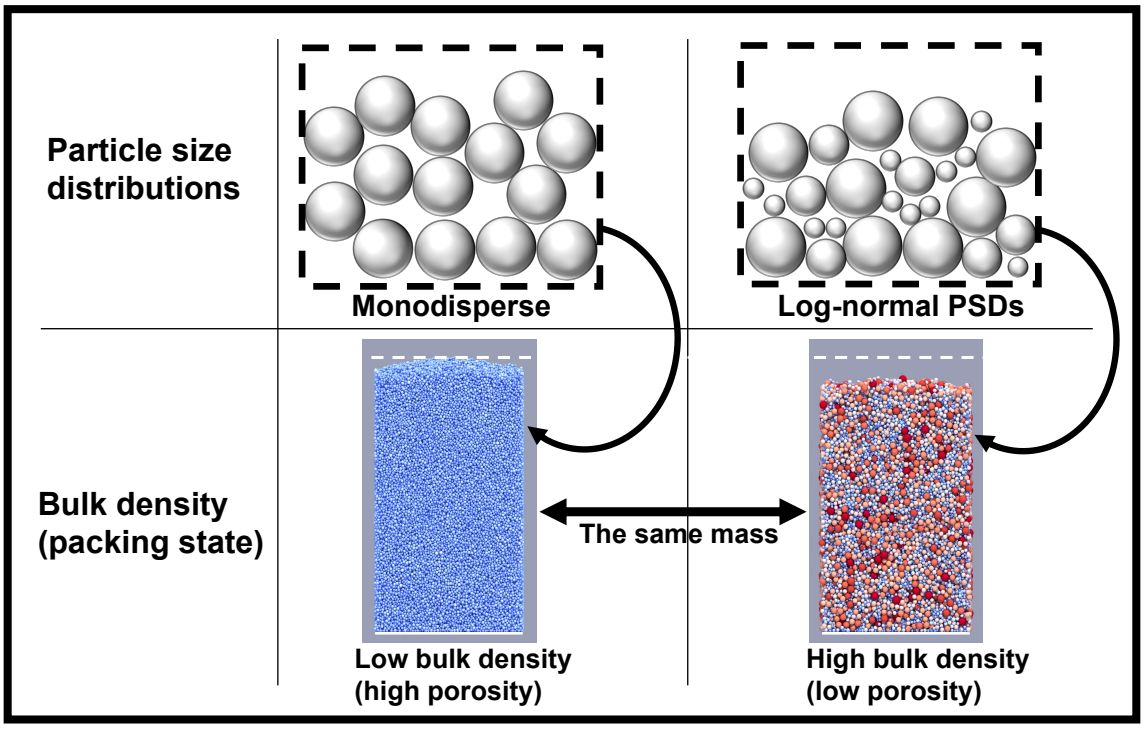

Figure 1.9: Particle size distributions can influence the packing states with the same mass of particles. The colours represent particle size, with red indicating the larger particles and blue indicating the smaller particles.

1.2 Modelling approaches of granular materials

Currently, empirical knowledge of granular materials is frequently employed in practical applications to improve the design of relevant equipment and process conditions. However, this often requires a significant number of trial-and-error attempts and incurs both time and financial costs. To understand the mechanisms of macro-scale phenomena, such as lumping and the transition of flow patterns in granular materials, it is necessary to investigate micro-level interactions, i.e. particle-level interactions. Nevertheless,

conducting experiments to study these mechanisms poses challenges due to difficulties in measuring particle interactions and observing internal behaviour. Computer simulations can be a powerful alternative for gaining more insight into these processes.

As illustrated in Figure 1.10, granular materials can be modelled either as a continuum, where the relationship between stresses and strains is determined through a constitutive model, or as separate particles with resolved interactions at the particle level size.

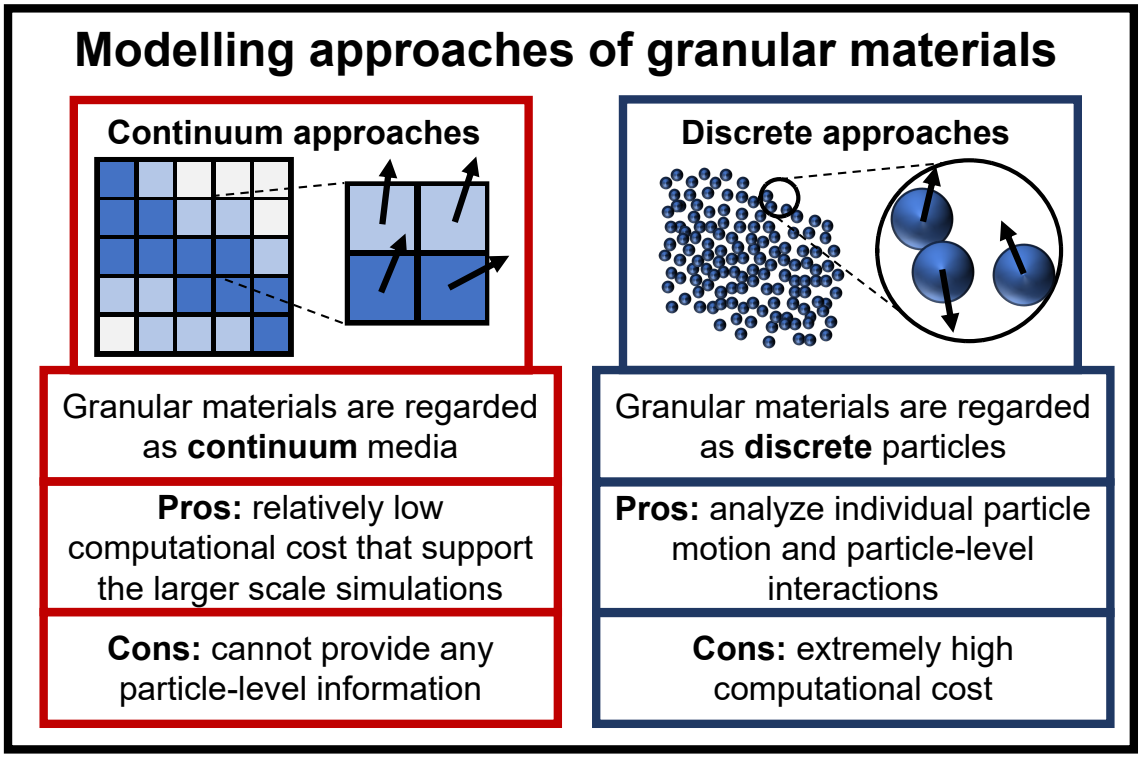

Figure 1.10: The classification of approaches for modelling granular materials.

To simulate granular materials using continuum approaches, the bulk discrete particles are represented as a continuum governed by constitutive laws. These constitutive laws are typically formulated as differential equations that establish relationships between mechanical field variables, i.e. stress and strain. In continuum modelling of granular materials, the granular material is assumed to be distributed continuously throughout its volume without explicitly considering individual particle contacts, similar to how the Eulerian method in computational fluid dynamics (CFD). In this modelling approach, the

length scale of the computation domain typically exceeds the size of individual particles, where one grid is considered to contain multiple particles. Continuum models do not analyse the motion of individual particles or the interactions between them, which means they cannot provide any particle-level information. It restricts the application of continuum models in modelling granular materials. A more detailed introduction to continuum models for modelling granular materials is presented in Section 1.2.1.

According to the discrete nature of granular materials, discrete approaches represent them as a group of individual particles. It provides more detailed insights at the particle-level and may be a more suitable approach for investigating the particle-level mechanisms that influence the behaviour of bulk particles. However, the computational cost of discrete approaches is extremely high when tracing a large number of particles, which limits the applications of discrete approaches. More specific introductions to discrete approaches are presented in Section 1.2.2.

1.2.1 Continuum approaches

Numerous studies on granular flow relevant to industry have focused on gas-solid two-phase flows, particularly fluidised beds [91, 92, 93, 94, 95, 96, 97]. The Eulerian–Eulerian two-fluid model (TFM) is one of the continuum approaches for describing gas-solid two-phase flows. This model was first applied to gas-particle flow systems in the 1960s [98, 91, 99], where the flow field of the particles is obtained by solving the local-averaged governing equation and the disperse phase constitutive equation simultaneously. The complete model of TFM was later proposed by Drew in the early 1980s [100]. The fundamental concept of the TFM is to consider the gas phase and solid phase as continuous and fully interpenetrating [93]. Consequently, constitutive models should be formulated for the solid phase in order to describe its fluid-like properties, such as viscosity, particle pressure, and temperature. For instance, the kinetic theory of granular flow (KTGF) [95, 101] has provided constitutive models for TFM. Within the framework of KTGF, the

granular viscosity is crucial in capturing the viscous behaviour of the dispersed solid phase, and neglecting the contribution from solid pressure would compromise numerical stability [102]. The TFM is known for its high computational efficiency, especially compared to discrete approaches, making it a suitable choice for simulating large-scale gas-solid flows. While TFM is capable of describing the macroscopic heterogeneities of gas-solid flow, accurately predicting fine-scale flow structures remains a challenge due to the simplifying assumptions and competing theories of TFM [103].

On the other hand, the continuum approaches can also be applied to model single-phase granular flow. The early stage studies of the continuum approaches involve the shallow flow of particles on sloping surfaces, which is used for modelling phenomena such as landslides and avalanches. The depth-averaged equations of motion are derived and developed to describe shallow granular flows on an inclined plane [104, 105, 106]. The depth-averaged models have several shortcomings and are only applicable to thin flowing layers compared to the lateral dimension [107]. The derivation of depth-averaged models, which are based on measurements from steady flow conditions, may make the models unsuitable for thick and transient granular material flows [108]. Therefore, it can be suggested that depth-averaged models are of limited use for modelling the complex dynamics of dense, transient granular material flows, such as those in silos. Consequently, some two-dimensional continuum models [109, 110, 111, 112] are used to simulate the flow behaviours of granular materials in plane silos and hoppers, where the transient analysis of stress fields in silos is conducted and the predicted wall pressures are in good agreement with that measured in experiments. More recently, three-dimensional continuum model simulations have also been used to simulate silo discharge [113, 114], including mass and funnel flow modes, flow rate, and wall pressure. The results generally agree with experimental findings, overcoming limitations of earlier continuum models. The advantage of continuum models for granular materials is their relatively low computational cost compared to discrete methods, making them widely used in previous simulations of granular

flows. However, there are some drawbacks that limit their application. The continuum approach suffers from difficulties in predicting free surfaces and moving boundaries due to its adoption of the Eulerian description. For instance, continuum models are unable to accurately model the filling process and packing structure of particles [115, 116], and the dynamic discharge process of silos [115, 117, 118]. Continuum models also do not allow for observation and study of individual particle behaviour at a granular scale [116, 117, 118], which can be modelled by discrete approaches [119].

The constitutive equation of single-phase granular materials in various continuum models relies on empirical parameters. It is well known that there is no universal constitutive model for continuum modelling that can accurately simulate the behaviour of granular materials during rapid, transitional, and slow flow [120, 121]. Therefore, different granular flow systems require determining distinct constitutive equations through experiments. Finally, continuum models of granular materials are difficult to incorporate the cohesion forces and rolling resistance between particles. Those particle-level interactions play a significant role in various processes that are related to granular materials in industry. The limitations of continuum models have led to an increasing interest in using discrete approaches to model the bulk behaviour of granular materials.

1.2.2 Discrete approaches

In the past few decades, the discrete element method (DEM) has been the most established discrete approach for modelling granular materials, which was originally developed by Cundall and Strack in 1979 [122]. DEM is a Lagrangian model that employs microscopic properties to directly calculate particle interactions and track the motion of individual particles. In the soft sphere model of DEM, particles can overlap at contact and the contact forces are determined by a model that relates the overlapping distance to the force. The motion of particles is determined by Newton's second law, which states that the total force on a particle equals its mass times its acceleration. The velocity and

displacement of the particles are obtained by numerically integrating Newton's second law of motion. Therefore, the motion of the particles is governed by interactions among particles and between particles and surrounding structures.

DEM naturally bridges the gap between particle-level interactions and the macroscopic properties and behaviours of bulk particles, which serves as an ideal tool for enhancing our understanding of the micro-macro transitions of granular materials [123, 124, 125, 39, 126]. The macroscopic properties of particles can be significantly influenced by various microscopic factors. Among these, three factors are particularly noteworthy and can be effectively captured through DEM simulations:

- **Inter-particle forces:** Previously, DEM was mostly used to simulate relatively coarse particles where only contact force [122, 92] and body (external) force [94, 127] are dominant due to its simplicity, and proven to provide comparable results to experimental data [128, 129]. Recently, an increasing number of researchers are trying to incorporate more complex inter-particle forces into DEM, such as capillary force [96, 130, 53, 131], viscous force [50, 132, 52, 61, 62], surface adhesion force [44, 133, 134, 135, 136], and electrostatic force [137, 138]. These attraction forces can cause agglomerates, lumps and/or wall make-ups, that are not observed with free-flowing particles.

- **Rolling resistance:** It is widely recognised that the rolling resistance exerts a significant influence on the macroscopic properties of powders [139, 140]. It is necessary for reproducing some physical phenomena such as shear band formation [141, 142] that may not be observed in freely rolling particles. Physically, rolling resistance can arise from various sources, e.g., micro-slip and friction on the contact surface, plastic deformation around the contact, viscous hysteresis and surface adhesion. Since spherical particles are often used in DEM because of the efficient contact detection and easy implementation, rolling resistance is sometimes employed to take

into account the particle non-sphericity [143]. Many models have been proposed in literature to evaluate the rolling resistance [144, 145, 146, 65, 147], some of which are well reviewed by Ai et al. [82].

- **Particle size distributions:** The size of particles is a crucial microscopic characteristic [3]. The actual granular materials often exhibit non-uniform sizes, known as particle size distributions (PSDs), which can introduce complexities in the simulation of granular materials. Although incorporating PSDs into DEM simulations may increase computational cost [148], it is conceptually not difficult due to their discrete nature [84, 86, 149, 150, 87, 151, 88, 152, 85, 153, 16, 154].

1.3 Speed-up methods of DEM

One of the significant challenges in DEM is the extremely high computational cost, which is typically proportional to the number of particles in the system and inversely proportional to the time step size. In general, industrial-scale equipment can contain far more than billions of particles. Despite the rapid advancement of computational power over the past decades, it remains challenging or practically impossible to complete large-scale simulations within an acceptable time frame. This makes it difficult to apply DEM to industrial-scale processes even with the computer power today. Therefore, various strategies have been implemented to speed-up DEM simulations including computation on graphics processsing units (GPU computation) [155, 149, 156, 157], domain decomposition [158, 159], particle stiffness reduction [45, 160, 161, 162, 163, 164] and coarse grain models [139, 165, 166, 167, 168, 169, 170, 171, 172, 154]. Coarse grain models employ artificially scaled-up particles that replicate bulk behaviour of the original particles, and DEM simulation with coarse grain model is called coarse-grained DEM in this study. Consequently, this approach allows for a reduction in the number of particles within the system and an increase in the time step size. Due to the potential to reduce the com-

putational cost by many orders of magnitude, the coarse grain models have gained great popularity.

1.4 Coarse grain models of DEM

In the coarse grain model, it is essential to appropriately scale the forces acting on the scaled-up particles. Chan and Washino [173] have classified coarse grain models into two categories: parameter scaling and direct force scaling. The parameter scaling involves the modification of physical particle properties to maintain kinematic similarity between the scaled-up and original particle systems [139, 168, 174, 175]. This approach is straightforward and does not require additional programming for implementation. However, the scaling criterion of each parameter is contingent upon the employed models, and may be complex or difficult to determine. On the other hand, the direct force scaling first evaluates the forces exerted on the original particles by using the original particle parameters and variables, which are then directly scaled [165, 169, 173]. In general, this approach tends to give simpler scaling laws than the parameter scaling which attracts increasing attention.

Several efforts have been made to discuss the scaling laws of forces. l is often used as the scale factor: the size ratio between the scaled-up and original particles. The pioneering work of Sakai and Koshizuka [165] proposed l^3 scaling for contact, fluid, and gravitational forces, which means that the forces acting on the scaled-up particle are l^3 times greater than those acting on the original particle. This keeps the same equations of motion between the original and scaled-up particles. Chu et al. [169] proposed a model that attempts to maintain the same total impulse, which also leads to l^3 scaling for fluid and gravitational forces. However, it is difficult to derive a scaling law for contact force in their model since it requires the contact duration a priori. Nevertheless, they suggested l^2 scaling based on the assumption that the contact duration is linearly proportional to the particle size.

A coarse grain model was proposed by Chan & Washino [173, 176] based on the continuum assumption of arbitrary particle flow, where the scaling laws are derived in a way that ensures an equivalent bulk momentum change in the control volume. It assumed a sufficient number of particles within one CV and ignoring fluctuations in particle velocities and inter-particle forces. The scaling laws can be widely applied to various types of forces and torques, as the derivations do not depend on any specific force or torque.

Based on the scaling laws proposed by Chan & Washino, the present study developed a new coarse grain model, it is named as the scaled-up particle (SUP) model. One of the most significant differences between the SUP model and conventional coarse grain models [165, 166, 169, 173, 176] lies in its reasonable estimation of both the overlap and separation distance between original particles, which are essential for estimating the forces and torques on these particles. The SUP model can be widely applied to various types of forces and torques, theoretically resulting in l^2 scaling for any inter-particle forces and l^3 scaling for any body forces.

1.5 Problems and research objectives

This study focuses on three problems which have not been sufficiently discussed in past studies on the coarse grain models. They are related to inter-particle forces, torques and particle size distributions, respectively:

- The first problem is how to evaluate the inter-particle forces acting on the scaled-up particles. The evaluation of inter-particle forces is related to how to evaluate the original particle variables. In the coarse grain model of DEM, the original particles are not explicitly simulated but represented by scaled-up particles. Therefore, particularly in the direct force scaling, it is important to properly evaluate the original particle variables related to the force estimation, such as the translational velocity, angular velocity, particle overlap and separation distance, from the corresponding

scaled-up particle variables. Sakai and Koshizuka [165] suggested to use the same translational velocity between the original and scaled-up particles, whilst the angular velocity of the original particle is taken to be l times larger than that of the scaled-up particle. These relationships are based on the conservation of the total kinetic energies in both the original and scaled-up particle systems. On the other hand, they assumed that the overlap of the original particle is the same as that of the scaled-up particle when estimating the contact force, which is not as well-grounded in theory. The same assumption is employed by Chan and Washino [173] for the separation distance to estimate the liquid bridge forces. However, to the best of the author's knowledge, there is no proper discussion in the literature regarding the validity of these assumptions.

- The second problem is the evaluation of inter-particle torques for the scaled-up particles. It is also important to properly scale the torques acting on particles so that the phenomena related to the original particle rotation can be replicated. In previous works of CFD-DEM, the fluid drag is considered as body force, and the torques of fluid drag force and gravity are usually neglected [158, 160, 8]. In the present work, however, the fluid drag is not taken into consideration, and only gravity acts as the body force. Since the spherical particle is employed and the relatively small size of single particle, the torque from gravity of single particle can be considered negligible and the torque of contact force is dominant. In many of the coarse grain models including those by Sakai and Koshizuka [165] and Chu et al. [169], the torques are computed in the standard procedure for DEM particles. In other words, the torques are given by using the particle radius and forces which are both already "scaled-up". The concept is very different in the SUP model. The torques on the original particles are first evaluated and then scaled so that the total change in angular momentum in control volumes remains the same. In this way, the scaling law of inter-particle torques coincides with that of inter-particle

forces. However, there is very limited discussion about the scaling laws of torques in literature.

- The third problem concerns the applicability of the SUP model to particles with size distributions. In the early stage of the model development [173, 176, 177], mono-dispersed and spherical particles are employed in the validation simulations for simplicity, which are also employed in Chapter 4, and 5. However, the theories used in the SUP model are generic and may be applicable to more complex systems. Washino et al. [178] have demonstrated that the SUP model can successfully replicate the original behaviour of a mixture of non-spherical particles. In principle, it is also expected that the SUP model can be used when there are particle size distributions as long as the continuum assumption is valid.

The objective of this study is to discuss the validity and applicability of coarse grain models in DEM for the three aforementioned problems:

- **Inter-particle forces evaluation:** Firstly, this study attempts to obtain a deeper understanding of the direct force scaling approach in the coarse grain model of DEM. Specifically, the focus is on evaluating original particle variables and it is recommended to use geometric similarity for both particle overlap and separation distance. Namely, they are scaled by the scale factor l to ensure the same amount of mass to be accommodated in a fixed space. Simulations of contact dominant uniaxial compression of a packed particle bed as well as wet and cohesive particle flows in a vertical mixer are presented to discuss the validity of the proposed method.

- **Inter-particle torques evaluation:** Another objective of the present work is to discuss the validity of the scaling law of inter-particle torques in the SUP model. Simulations of particle bed and heap formation are performed to measure the bulk density and angle of repose of original and scaled-up particles with rolling resistance. The influence of the coefficient of rolling resistance on the bulk density of particle

beds and the repose angle of particle heaps is being investigated. The results of the SUP model are compared with those obtained from other scaling laws and those of original simulations, to discuss the validity of torques scaling.

- **Particle size distributions:** Finally, to validate its capability in simulating particles with size distributions, the SUP model is employed to simulate particle beds with various PSDs. The simulation results of the SUP model are compared with those obtained from other scaling laws. The bulk density and average coordination number of particle beds with various PSDs are evaluated and compared to discuss the validity of the SUP model for particles with varying PSDs.

1.6 Thesis Outline

The organisation of this thesis is outlined as follows:

- In Chapter 2, the general concept of the discrete element method (DEM), as well as the inter-particle force models and inter-particle torque models used in this work, are introduced. Subsequently, the method for determining an appropriate time step for DEM simulation is introduced. Finally, the integration scheme employed in this work, i.e., the velocity Verlet scheme, to solve the motion equation of DEM particles is introduced.

- In Chapter 3, the general concept of the coarse grain model of DEM is introduced. Based on the employed scaling criterion, the coarse grain models of DEM can be classified into two types. The first type is parameter scaling, while the second type, known as direct force scaling, is employed in the present study. Subsequently, a novel coarse grain model is introduced, which is known as the scaled-up particle (SUP) model. The development and validation of the SUP model are the focus of this work. The concept, validity, and applicability of the SUP model are discussed

in Chapters 4, 5, and 6. Scaling of the critical time step in coarse grain models of DEM is introduced.

- The subject of Chapter 4 is to discuss the evaluation of inter-particle forces exerted on scaled-up particles, which is related to the evaluation of original particle variables: overlap and separation distance. A novel method (i.e. geometric similarity method) is proposed to evaluate the variables of original particle in coarse grain DEM simulation. Scaling laws of inter-particle forces are compared, and conventional method to evaluate the variables of original particles are compared with geometric similarity method. Finally, the simulations are conducted to validate the scaling of time step mentioned in Chapter3.

- The subject of Chapter 5 is the evaluation of inter-particle torques on scaled-up particles, along with a discussion on the influence of rolling resistance. Simulations are conducted to compare three combinations of scaling methods for inter-particle torques and forces, as well as to discuss the effect of rolling resistance on the bulk density of particle beds and repose angle of the particle heaps.

- In Chapter 6, the validation of the SUP model to different particle size distributions (PSDs) is presented. The bulk density of the particle beds was compared among various PSDs by simulating the particle bed. The employed PSDs in the validation simulations included a mixture of large and small particles, as well as log-normal particle size distributions.

- Chapter 7 is the conclusion chapter, which presents a comprehensive summary of the main findings of the present work and provides suggestions for future research.

Chapter 2

Discrete element method

2.1 Introduction

The fundamental principle of the discrete element method (DEM) is introduced in this chapter. In the present work, the inter-particle forces are explicitly modelled, and the positions and velocities of the particles are determined by solving Newton's equations of motion, which is called the soft-sphere model of DEM. The chapter begins with a thorough introduction to DEM, which is presented in Section 2.2.

The model used to describe the contact between particles is subsequently presented, along with an explanation of the fundamental principles of the soft-sphere model in Section 2.3, which includes both linear and non-linear spring-dashpot force models. In this study, the Hertz contact model and the Johnson-Kendall-Roberts (JKR) model are employed to describe particle contact, which is explained in Section 2.3.1. Inter-particle attraction force for DEM particles is investigated in the present work, the liquid bridge force and JKR surface adhesion force models are employed, which is explained in Section 2.3.2. The rolling resistance for DEM particles is employed in the present work, the models employed are introduced in Section 2.3.3.

The determination of an appropriate time step is crucial for conducting DEM simulations with stability and accuracy. The critical time step of DEM simulation is introduced in Section 2.4, while the integration scheme used to solve the equation of motion of par-

ticles is discussed in Section 2.5.

2.2 Discrete element method

Discrete element method has been widely used to simulate the flow, mixing, compaction, and other processing behaviours of granular materials. DEM is a promising numerical method to investigate the relationship between macroscopic properties and microscopic mechanisms of granular materials. The positions and velocities of individual particles in DEM are determined by solving Newton's equations of motion.

In the terms of particles collision checking, both hard-sphere and soft-sphere models have been employed in DEM. The hard-sphere model, proposed by Alder and Wainwright [179], was initially employed to calculate molecular dynamic motion. Subsequently, Campbell and Brennen [180] utilised this model to simulate two-dimensional flows of inelastic particles. Another model is the soft-sphere model, which was proposed by Cundall and Strack [122] and represents particle collisions as spring-dashpot interactions.

The computation of hard-sphere models is significantly faster than that of soft-sphere models because the solutions to impact equations are analytic. Pawel Kosinski et al. [181] classified the hard-sphere models based on the number of input parameters. A typical hard-sphere model is called one-parameter hard-sphere model, which assumes that particles are frictionless, rigid and cannot deform when they come into contact with each other. The only input parameter in the one-parameter hard-sphere model is the coefficient of restitution, which is typically defined as the ratio between the relative velocity of colliding particles along the normal to the plane of impact after collision and the same velocity measured prior to collision. The hard-sphere model shown in Figure 2.1 (a) is a classic example of a one-parameter hard-sphere model. This model assumes binary collisions that can partially conserve momentum and includes one parameter, the restitution coefficient, to adjust the momentum lost in a collision, while the collisions between particles occur instantaneously.

The two-parameter hard-sphere models incorporate the coefficients of restitution and friction, which are determined based on a comprehensive investigation into the collision dynamics between two bodies of arbitrary shape [182, 183, 184, 185, 186, 187, 188]. If the hard-sphere models are further extended, the augmentation of input parameters will correspondingly expand the range of phenomena explicable by the hard-sphere model [189, 190, 191, 181]. The applicability of typical hard-sphere models, however, is limited due to the challenges they face in considering complex particle-level phenomena. This becomes particularly evident when dealing with various types of interactions simultaneously, which may involve adhesion contact forces, capillary forces, and rolling resistance. On the other hand, the determination of the sequence of a group of binary collisions becomes complicated for dense particle systems with high collision frequency. Therefore, hard-sphere models are more suitable for simulating dilute particle systems with low collision frequency.

In the soft-sphere model, it is assumed that the particles maintain their geometric rigidity while undergoing deformations during a finite contact duration, as illustrated in Figure 2.1 (b). The accurate capture of particle contact deformation is crucial for the soft-sphere model, as it directly influences the calculation of inter-particle forces and torques. In contrast to the hard-sphere model, which sequentially solves a set of binary collisions, the soft-sphere model allows for simultaneous particle collisions. The soft-sphere model is suitable for investigating dense particle systems, where the effects of particle deformation and the complexity of frictional forces during contact are significant and cannot be ignored. In this study, the soft-sphere model is employed to describe the complex contact states among DEM particles, and a series of densely packed particle systems are investigated.

2.3 Soft-sphere model

The translational and rotational motion equations of Particle i interacting with adjacent Particle j, in accordance with Newton's second law of motion, are given by Equations

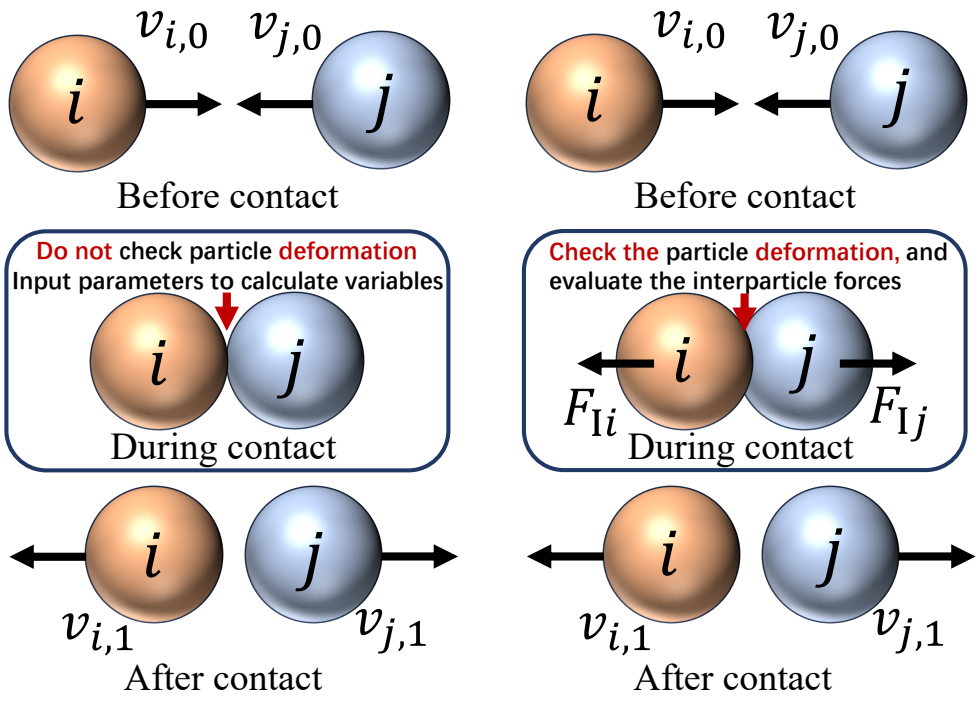

(a) Hard-sphere model (b) Soft-sphere model

Figure 2.1: Comparison of the hard-sphere and soft-sphere models of DEM. The hard-sphere model does not consider particle deformations (overlap) and evaluates particle variables, such as particle velocities after collision, using input parameters like the coefficient of restitution. On the other hand, the soft-sphere model considers deformation and evaluates inter-particle forces ($F_{\mathrm{I}i}$ and $F_{\mathrm{I}j}$) based on the deformation.

(2.1) and (2.2):

$$m_i \dot{\boldsymbol{v}}_i = \sum_j \boldsymbol{F}_{\mathrm{I}i,j} + m_i \boldsymbol{g} \tag{2.1}$$

$$I_i \dot{\boldsymbol{\omega}}_i = \sum_j (\boldsymbol{M}_{\mathrm{I}i,j} + \boldsymbol{M}_{\mathrm{R}i,j}) \tag{2.2}$$

In Equation (2.1), m_i represents the mass of Particle i, $\boldsymbol{v}_i$ denotes the translational velocity of Particle i, $\boldsymbol{F}_{\mathrm{I}i,j}$ represents the inter-particle force exerted on Particle i by Particle j, and $\boldsymbol{g}$ is the gravitational acceleration. The inter-particle force can be written as:

$$\boldsymbol{F}_{\mathrm{I}i,j} = \boldsymbol{F}_{\mathrm{C}i,j} + \boldsymbol{F}_{\mathrm{A}i,j} \tag{2.3}$$

where $\boldsymbol{F}_{\mathrm{C}}$ represents the contact force, the contact force model used in the present work is introduced in Section 2.3.1. $\boldsymbol{F}_{\mathrm{A}}$ is the inter-particle attraction force, which is introduced in Section 2.3.2.

In Equation (2.2), I_i is the moment of inertia, $\boldsymbol{\omega}_i$ is the angular velocity. $\boldsymbol{M}_{\mathrm{R}ij}$ is the torque from rolling resistance, which is defined in Section 2.3.3. $\boldsymbol{M}_{\mathrm{I}i,j}$ is the torque due to inter-particle force exerted on Particle i by Particle j, which is defined as:

$$\boldsymbol{M}_{\mathrm{I}i,j} = r_{\mathrm{p}} \boldsymbol{e}_{ni,j} \times \boldsymbol{F}_{\mathrm{I}i,j} \tag{2.4}$$

where r_{p} is the radius of the particle, $\boldsymbol{e}_{ni,j}$ is the unit vector from the centre of Particle i to Particle j. The solutions to Equations (2.1) and (2.2) are provided by the soft-sphere model presented in the subsequent section.

The soft-sphere model was initially proposed by Cundall and Strack [122], where the particle-particle collisions are simulated using springs, dashpots, and a frictional slider, as illustrated in Figure 2.2. In the normal direction, which refers to the vector connecting the centers of both particles, the spring represents the repulsion force due to elasticity, while the dashpot accounts for energy dissipation. In the tangential direction, which refers to the vector perpendicular to the normal direction, either the spring-dashpot or

the frictional slider is selectively used, with the former representing static friction and the latter indicating dynamic friction.

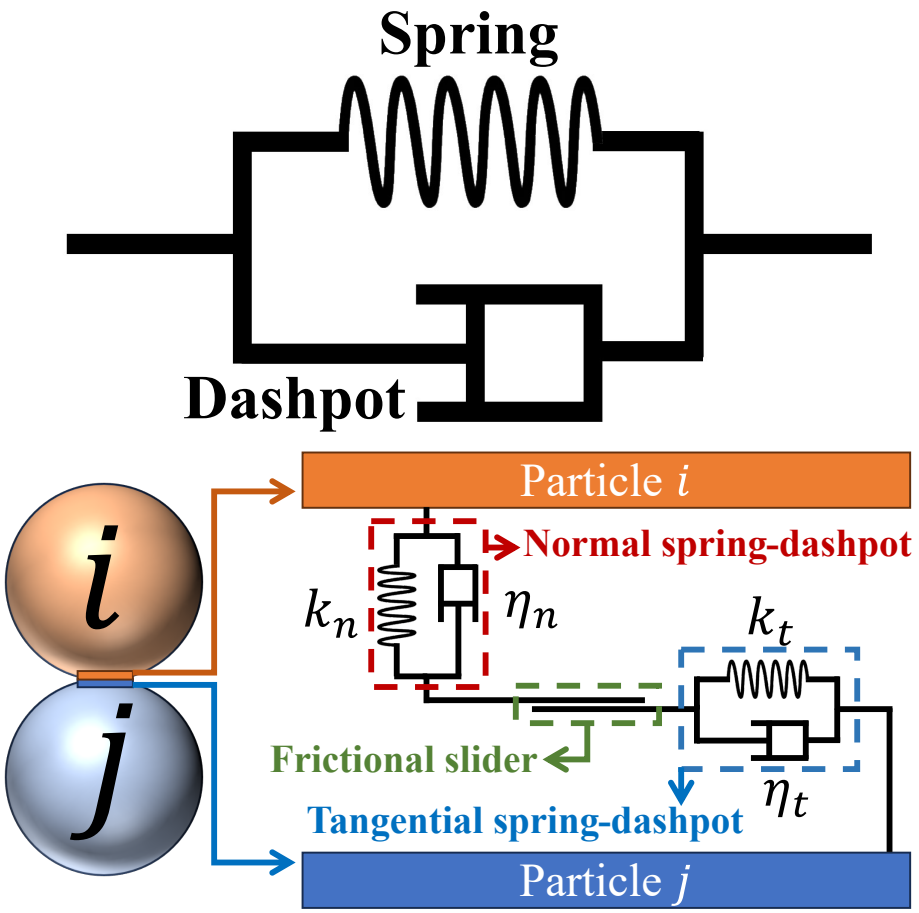

Figure 2.2: The soft-sphere model of DEM is illustrated in the schematic diagram. The collision forces in both the normal and tangential directions are calculated using springs, dashpots, and the frictional slider.

The normal force can be defined using either a linear-spring model or a non-linear spring model. In the pioneering work of the soft-sphere model, Cundall and Strack [122] employed a linear spring model, where the elastic repulsion force is linearly proportional to the displacement of the particle. For instance the elastic repulsion force in normal direction between Particle i and Particle j is given by:

$$\boldsymbol{F}_{\mathrm{C}ni,j} = (-k_n \delta_n - \eta_n \boldsymbol{v}_{ni,j} \cdot \boldsymbol{e}_{ni,j}) \boldsymbol{e}_{ni,j} \tag{2.5}$$

where k denotes the spring stiffness, δ_n represents the particle overlap, and η_n is the damping coefficient of the dashpot in the normal direction. $\boldsymbol{v}_{ni,j}$ denotes the relative velocity of Particle i to Particle j in the normal directions respectively.

The simulation time step can be determined simply by considering the eigenfrequency of a spring-mass system, which is independent of the particle collision velocity [94]. The precise description of the individual collision forces between spherical particles poses a challenge to the linear-spring model [192, 193].

In contrast to the linear spring model, a non-linear spring model can be described by the non-linear stiffness spring coefficient estimated based on material properties such as Young's modulus and Poisson's ratio. The non-linear spring model incorporates the Hertzian contact theory [194], which states that the elastic repulsion force is proportional to the particle displacement raised to the power of 3/2 that between particles of isotropic elastic material with perfectly smooth surfaces. The non-linear spring model can capture the dynamic behaviour of colliding particles in various systems. In the non-linear spring model, the normal force and tangential force exerted on Particle i upon contact with Particle j are given by equations (2.6) and (2.7), respectively.

$$\boldsymbol{F}_{\mathrm{C}ti,j} = (-k_n\delta_n^{3/2} - \eta_n\boldsymbol{v}_{ni,j}\cdot\boldsymbol{e}_{ni,j})\boldsymbol{e}_{ni,j} \tag{2.6}$$

$$\boldsymbol{F}_{\mathrm{C}ti,j} = \min[-k_t\delta_t - \eta_t(\boldsymbol{v}_{ti,j}\cdot\boldsymbol{e}_{tij}), -\mu_{\mathrm{s}}|\boldsymbol{F}_{\mathrm{C}ni,j}|]\boldsymbol{e}_{ti,j} \tag{2.7}$$

where μ_s is the sliding friction coefficient. The subscripts 'n' and 't' indicate the quantities for the normal and tangential directions, respectively. The variables k, δ, and η represent the spring stiffness coefficient, displacement, and damping coefficient correspondingly. $\boldsymbol{v}_{ni,j}$ and $\boldsymbol{v}_{ti,j}$ denote the relative velocity of Particle i to Particle j in the normal and tangential directions respectively. $\boldsymbol{e}_{ni,j}$ is the unit vector from the centre of Particle i to Particle j, and $\boldsymbol{e}_{ti,j}$ is the unit vector perpendicular to the unit vector $\boldsymbol{e}_{ni,j}$. The relative velocity in tangential $\boldsymbol{v}_{ti,j}$ can be evaluated based on the sum of the transnational and

rotational velocities as follows:

$$\boldsymbol{v}_{ti,j} = \boldsymbol{v}_{ni,j} - (\boldsymbol{v}_{ni,j} \cdot \boldsymbol{e}_{ni,j})\boldsymbol{e}_{ni,j} + r_p(\boldsymbol{\omega}_i + \boldsymbol{\omega}_j) \times \boldsymbol{e}_{ni,j} \tag{2.8}$$

where $\boldsymbol{\omega}$ is the rotational velocity. The unit vector in the tangential direction is given by:

$$\boldsymbol{e}_{ti,j} = \frac{\boldsymbol{v}_{ti,j}}{|\boldsymbol{v}_{ti,j}|} \tag{2.9}$$

When Particle i is simultaneously in contact with more than two particles, the total collision force and torque exerted on Particle i are computed as follows:

$$\sum_j \boldsymbol{F}_{\mathrm{C}i,j} = \sum_j (\boldsymbol{F}_{\mathrm{C}ni,j} + \boldsymbol{F}_{\mathrm{C}ti,j}) \tag{2.10}$$

$$\sum_j \boldsymbol{M}_{\mathrm{C}i,j} = \sum_j (r_{\mathrm{p}} \boldsymbol{e}_{ni,j} \times \boldsymbol{F}_{\mathrm{C}ti,j}) \tag{2.11}$$

The non-linear spring model, based on the Hertz contact theory [194], is applicable for small displacements and non-adhesive contacts. The Johnson-Kendall-Roberts (JKR) contact model [44] was proposed to describe adhesive contact, which is an extension of the Hertz model that introduces an attractive force component F_{adh} due to the surface energy γ of the two materials. The JKR model predicts that the contact area A is larger than what is predicted by the Hertz model. Additionally, it suggests that there exists a finite pull-off force, represented as F_{po}, when the surfaces separate. In addition to accounting for attraction forces caused by van der Waals effects, the JKR model is also used to describe materials where adhesion is due to capillary or liquid-bridge forces [45]. The present study also involves adhesive contacts, and the JKR model is utilised to describe these adhesive contacts.

2.3.1 Contact force

The normal contact force in the JKR theory and Hertz theory can be written as the same form that evaluating the normal contact force using the contact radius a as illustrated in Figure 2.3.

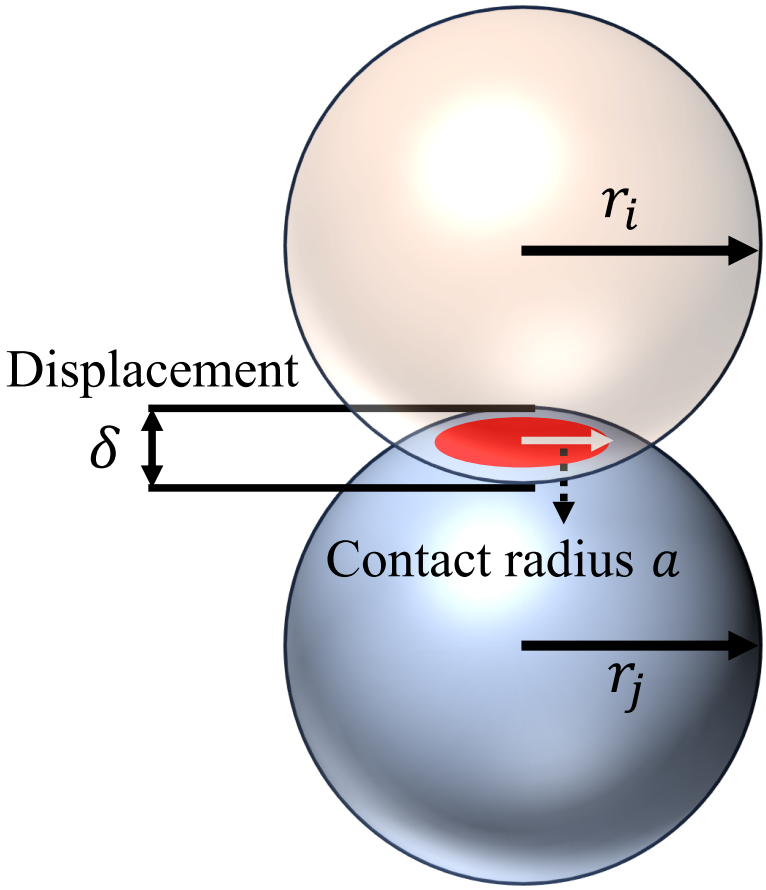

Figure 2.3: Schematics of contact between Particle i and Particle j. The contact area A is represented by the red-marked area.

The contact forces in the normal and tangential directions are given as follows:

$$\boldsymbol{F}_{\mathrm{C}ni,j} = -\left(\frac{4E^*}{3r^*}a^3 + \eta_n \boldsymbol{v}_{i,j} \cdot \boldsymbol{e}_{ni,j}\right)\boldsymbol{e}_{ni,j} \tag{2.12}$$

$$\boldsymbol{F}_{\mathrm{C}ti,j} = -\min(8G^*\sqrt{r^*\delta_n}\delta_t + \eta_t v_{\mathrm{s}},\ \mu_{\mathrm{s}}F_{\mathrm{N}})\boldsymbol{e}_{ti,j} \tag{2.13}$$

where δ is the particle overlap, i.e. particle deformation, η is the damping coefficient,

$\boldsymbol{v}_{i,j}$ is the relative velocity between Particle i and Particle j, v_s is the magnitude of the relative tangential velocity at the contact surface, μ_s is the sliding friction coefficient. F_N represents the normal load during sliding, which is being $|\boldsymbol{F}_{ni,j}|$. r^*, E^* and G^* are defined as:

$$\frac{1}{r^*} = \frac{1}{r_i} + \frac{1}{r_j} \tag{2.14}$$

$$\frac{1}{E^*} = \frac{1-\nu_i^2}{E_i} + \frac{1-\nu_j^2}{E_j} \tag{2.15}$$

$$\frac{1}{G^*} = \frac{2(2-\nu_i)(1+\nu_i)}{E_i} + \frac{2(2-\nu_j)(1+\nu_j)}{E_j} \tag{2.16}$$

where E is the Young's modulus and ν is the Poisson's ratio. In the Hertzian theory, the contact radius a is calculated as:

$$a = \sqrt{r^*\delta_n} \tag{2.17}$$

substituting Equation (2.17) into (2.12), the subsequent equation can be derived:

$$\boldsymbol{F}_{\mathrm{C}ni,j} = -\left(\frac{4}{3}E^*\sqrt{r^*}\delta_n^{3/2} + \eta_n \boldsymbol{v}_{i,j}\cdot\boldsymbol{e}_{ni,j}\right)\boldsymbol{e}_{ni,j} \tag{2.18}$$

when the particle material and particle size are determined, the coefficient before the first term of right side of Equation (2.18) is a constant, which is the normal spring coefficient in Equation (2.6):

$$k_n = \frac{4}{3}E^*\sqrt{r^*} \tag{2.19}$$

The substitution of Equation (2.19) into Equation (2.18) yields Equation (2.6), which mean the different expressions (calculating by overlap or contact area) can represent the same theory of contact.

When considering the interaction between two identical smooth spheres with radius r_i and Young's modulus E_i, the effective radius r^* and Young's modulus E^* are given by:

$$r^* = \frac{r_i}{2} \tag{2.20}$$

$$E^* = \frac{E_i}{2(1-\nu^2)} \tag{2.21}$$

substituting Equations (2.20) and (2.21) into Equation (2.19), and then the normal spring coefficient k_n can be rewritten as follows:

$$k_n = \frac{\sqrt{2r_i}E_i}{3(1-\nu^2)} \tag{2.22}$$

which is the the spring stiffness in the normal direction proposed in the Hertz model [194].

The JKR theory predicts a larger contact area than Hertz theory, where the contact radius a is given as the solution of a fourth-order polynomial, which is first given by Deng el al. [195]. Parteli et al. [196] proposed an analytical solution by employing a fourth-order expansion of this equation and determining the real root that exceeds the radius of contact patch in the classical Hertz model, resulting in:

$$a^4 - 2r^*\delta_n a^2 - \frac{4\pi\gamma r^{*2}}{E^*}a + r^{*2}\delta_n^2 = 0 \tag{2.23}$$

where γ is the surface energy of the particle. The damping coefficients in the normal and tangential directions are given as [92]:

$$\eta_n = -2\sqrt{\frac{5}{3}}\beta(m^*E^*)^{1/2}r^{*1/4}\delta_n^{1/4} \tag{2.24}$$

$$\eta_t = -4\sqrt{\frac{5}{3}}\beta(m^*G^*)^{1/2}r^{*1/4}\delta_n^{1/4} \tag{2.25}$$

$$\frac{1}{m^*} = \frac{1}{m_i} + \frac{1}{m_j} \tag{2.26}$$

where β is a function of the coefficient of restitution, e, and defined as:

$$\beta = \frac{\ln(e)}{\sqrt{\ln^2(e)+\pi^2}} \tag{2.27}$$

F_{N} is given by the magnitude of the normal contact force when the Hertzian theory is used. In the JKR theory, it is given by the effective normal force as [197, 198]:

$$F_{\mathrm{N}} = \left| 4\left(\frac{a}{a_0}\right)^3 - \left(\frac{a}{a_0}\right)^{3/2} + 2 \right| F_{\mathrm{po}} \tag{2.28}$$

where F_{po} is the pull-off force and a_0 is the contact radius at the equilibrium condition, which are defined as:

$$F_{\mathrm{po}} = 3\pi\gamma r^* \tag{2.29}$$

$$a_0 = \left(\frac{9\pi\gamma r^{*2}}{E^*}\right)^{1/3} \tag{2.30}$$

2.3.2 Attraction force

Various models for attraction force, $\boldsymbol{F}_{\mathrm{A}}$, have been proposed and applied in DEM, such as capillary force [96, 130, 53, 131], viscous force [50, 132, 52, 61, 62], surface adhesion force [44, 133, 134, 135, 136], and electrostatic force [137, 138]. In order to validate a new coarse grain model of DEM proposed in Chapter 3, which is further validated in Chapters 4 and 5, this work employs capillary force and JKR surface adhesion force to assess its applicability to different types of inter-particle attraction forces. These forces are summarised below.

2.3.2.1 Capillary force model

In various powder handling processes, such as wet granulation and coating, the addition of liquid to a powder flow is commonly employed to enhance particle cohesiveness and stickiness. During these processes, the state of the liquid may vary depending on the degree of space saturation between particles, as illustrated in Figure 2.4. When a small amount of liquid is dispersed into particles, it may form liquid bridges that create capillary forces between the particles. The liquid bridges are typically assumed to be symmetrical and pendular in shape.

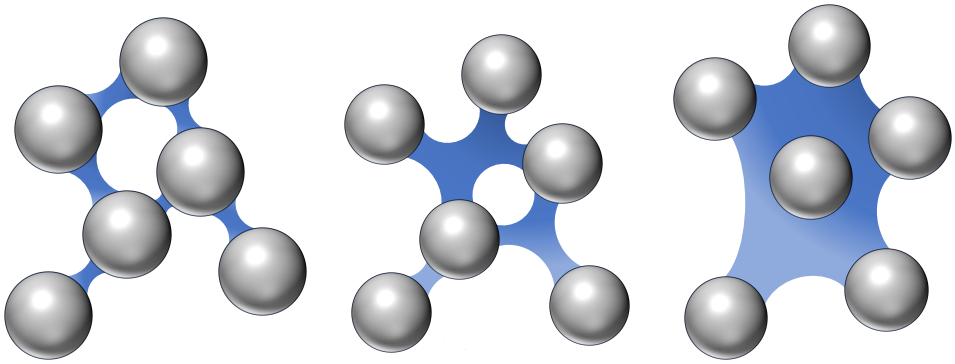

(a) Pendular (b) Funicular (3) Capillary

Figure 2.4: Liquid states in particle system with different degree of pore saturation: (a) pendular state, (b) funicular state and (c) capillary state.

When a static pendular liquid bridge is formed between two particles with an equal radius as shown in Figure 2.5, the particles are pulled towards each other by the capillary force. Theoretically the capillary force due to a static pendular bridge depends both on the shape of the bridge and the surface tension coefficient and is determined as follows [51]:

$$F_{\text{cap,theory}} = 2\pi r_{\text{p}}\gamma_{\text{L}} \sin\psi \sin(\theta + \psi) + \pi r_{\text{p}}^2 \Delta p \sin^2\psi \tag{2.31}$$

where r_{p} is the particle radius, γ_{L} is the surface tension coefficient, ψ is the half-filling angle and θ is the contact angle. The first term on the right-hand side of Equation (2.31) represents the contribution of surface tension along the solid-liquid-gas interface perimeter. The second term corresponds to the hydrostatic pressure force. The pressure difference across the liquid-gas interface, denoted as Δp, which is referred to as the Laplace pressure, can be mathematically described by the Laplace-Young equation [64] as follows:

$$\Delta p = \gamma_{\text{L}} \left(\frac{1}{r_1'} - \frac{1}{r_2'} \right) \tag{2.32}$$

where r_1' and r_2' are the curvature radii of the liquid bridge.

Due to its strong non-linearity in terms of surface curvature and the implicit body force on the interface, solving the Young-Laplace equation analytically is challenging [199].

Several approximate solutions of the Young-Laplace equation, which rely on the simplified shape of the liquid bridge, have been described in the literature [200, 201, 53, 202]. Fisher [200] proposed a simple approach to estimate the liquid bridge forces, which was based on a toroidal approximation that treated the meridional profile of the liquid-air interface as an arc of a circle [51]. Namely, the toroidal approximation approximates the curvature radii of a liquid bridge as an arc of a circle (Figure 2.6). To obtain a reasonable estimation, the capillary force is calculated using Lian's method [51]:

$$\begin{aligned} F_{cap} &= 2\pi r_2 \gamma_{\mathrm{L}} + \pi r_2^2 \Delta p \\ &= 2\pi r_2 \gamma_{\mathrm{L}} + \pi r_2^2 \gamma_{\mathrm{L}} \left(\frac{1}{r_1} - \frac{1}{r_2} \right) \end{aligned} \tag{2.33}$$

where r_1 and r_2 represent the approximated curvature radii at the neck of the liquid bridge. The non-dimensional capillary force $\hat{F}_{\mathrm{cap}}$ is defined as:

$$\hat{F}_{\mathrm{cap}} = \frac{F_{\mathrm{cap}}}{2\pi \gamma_{\mathrm{L}} r_{\mathrm{p}}} = \frac{\hat{r}_2(\hat{r}_1 + \hat{r}_2)}{2\hat{r}_1} \tag{2.34}$$

where $\hat{r}_1 = r_1/r_{\mathrm{p}}$ and $\hat{r}_2 = r_2/r_{\mathrm{p}}$.

The dimensionless volume of the liquid bridge, denoted as $\hat{\lambda}_{\mathrm{L}}$, is defined using the volume of the liquid bridge λ_{L} and the particle volume V_{p} as follows:

$$\hat{\lambda}_{\mathrm{L}} = \frac{\lambda_{\mathrm{L}}}{V_{\mathrm{p}}} \tag{2.35}$$

The integration of the contour of the liquid bridge yields $\hat{\lambda}_{\mathrm{L}}$ as follows:

$$\begin{aligned} \hat{\lambda}_{\mathrm{L}} &= 2\left\{ \frac{3}{4} \int_0^{\hat{x}_0} \left(\hat{r}_2 + \hat{r}_1 - \sqrt{\hat{r}_1^2 - x^2} \right)^2 \mathrm{d}x - \frac{3}{4} \int_{\hat{h}}^{\hat{x}_0} \left\{ 1 - (x - 1 - \hat{h})^2 \right\} \mathrm{d}x \right\} \\ &= \frac{3}{2} \left[\left\{ (\hat{r}_1 + \hat{r}_2)^2 + \hat{r}_1^2 \right\} \hat{x}_0 - \frac{1}{3}\hat{x}_0^3 - \hat{x}_0(\hat{r}_1 + \hat{r}_2)\sqrt{\hat{r}_1^2 - \hat{x}_0^2} - \hat{r}_1^2(\hat{r}_1 + \hat{r}_2)\zeta \right] \\ &\quad - \frac{3}{2} \left[(1 + \hat{h})\hat{x}_0^2 - \hat{h}(\hat{h} + 2)\hat{x}_0 - \frac{1}{3}\hat{x}_0^3 + \frac{1}{3}\hat{h}^3 + \hat{h}^2 \right] \end{aligned} \tag{2.36}$$

where h represents half of the separation distance between particles, and x_0 is the distance from the centre of the bridge to the three-phase contact line. The non-dimensional distances are defined as $\hat{h} = h/r_\mathrm{p}$ and $\hat{x_0} = x_0/r_\mathrm{p}$. Refer to Figure 2.6, there are following geometrical relations among the dimensions of liquid bridge:

$$\hat{x}_0 = \hat{r}_1 \cos(\psi + \theta) \tag{2.37}$$

$$\zeta = \frac{\pi}{2} - (\psi + \theta) \tag{2.38}$$

$$\hat{r}_1 = \frac{1 + \hat{h} - \cos\psi}{\cos(\psi + \theta)} \tag{2.39}$$

$$\hat{r}_2 = \frac{(1 + \hat{h})\{\sin(\psi + \theta) - 1\} + \cos\psi - \sin\theta}{\cos(\psi + \theta)} \tag{2.40}$$

The following equation is obtained through the substitution of Equations (2.37) and (2.38) into Equation (2.36):

$$\begin{aligned}\hat{\lambda}_L =& \frac{3}{2}\Bigg[\left\{(\hat{r}_1 + \hat{r}_2)^2 + \hat{r}_1^2\right\} \hat{r}_1 \cos(\psi + \theta) - (\hat{r}_1 + \hat{r}_2)\hat{r}_1^2 \sin(\psi + \theta)\cos(\psi + \theta) \\ & - \hat{r}_1^2(\hat{r}_1 + \hat{r}_2)\left\{\frac{\pi}{2} - (\psi + \theta)\right\} - (1 + \hat{h})\hat{r}_1^2 \cos^2(\psi + \theta) + \hat{h}(\hat{h} + 2)\hat{r}_1 \cos(\psi + \theta) \\ & - \frac{\hat{h}^2(\hat{h} + 3)}{3}\Bigg]\end{aligned} \tag{2.41}$$

where $\hat{r}_1$ and $\hat{r}_2$ can be determined by solving Equations (2.39), (2.40), and (2.41) simultaneously. The adhesion force of a liquid bridge can be obtained from r_1' and r_2' using Equation (2.35).

Lambert et al. conducted a comparative analysis of two approaches for modeling capillary force [131], namely the energetic approach and the Laplace equation based approach. They demonstrated the two approaches are equivalent in calculating capillary forces at equilibrium.

In the literature, many models of liquid bridge force have been proposed [96, 130, 53,

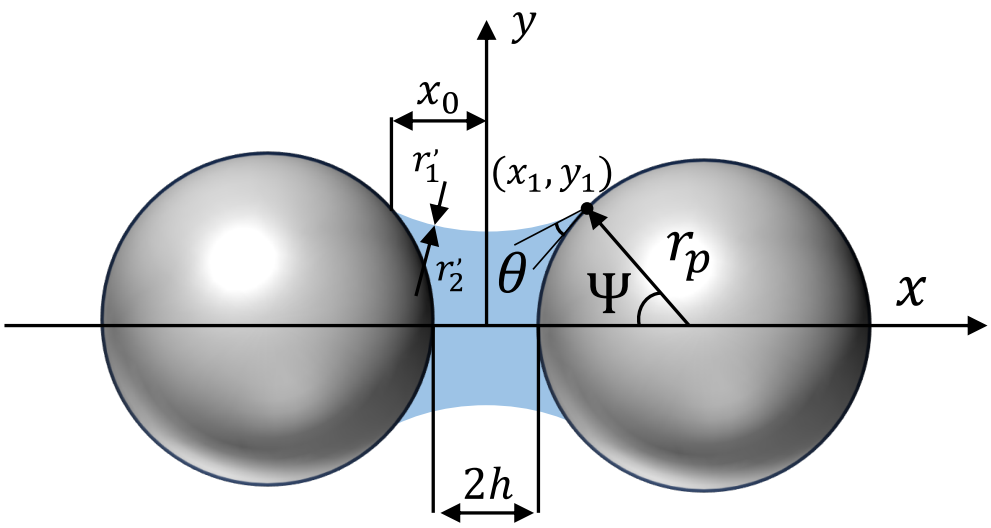

Figure 2.5: A static liquid bridge formed between two equal particles.

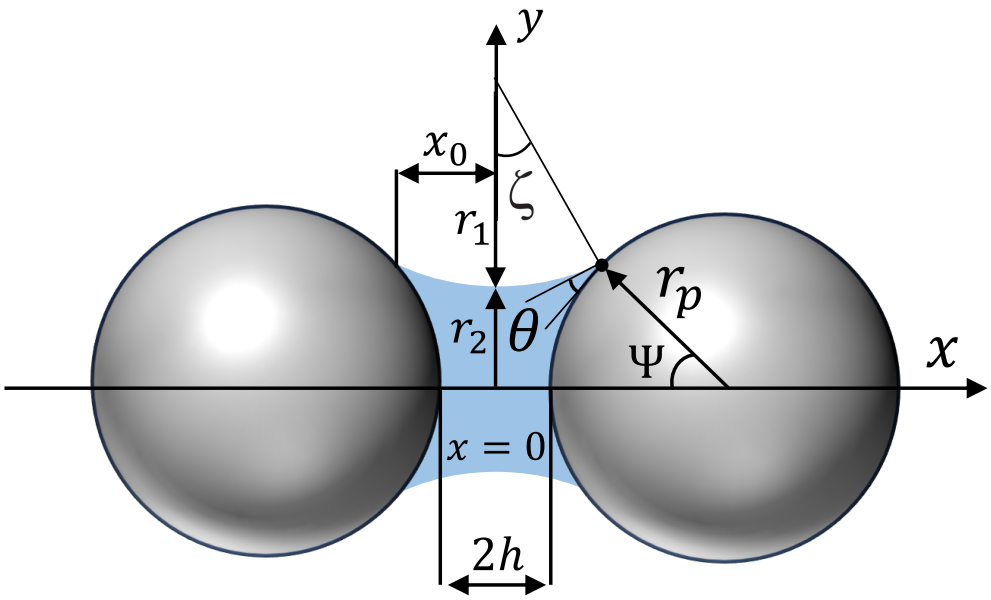

Figure 2.6: Toroidal approximation of a static liquid bridge formed between two equal particles.

131, 201]. In the context of this study, the chosen model is the Rabinovich-Lambert model [53, 131], which is expressed as follows:

$$\boldsymbol{F}_{\text{cap}} = C_{\text{cap}} \boldsymbol{e}_{ni,j} \tag{2.42}$$

$$C_{\text{cap}} = \frac{4\pi r^* \gamma_{\text{L}} \cos\theta}{1 + 1/(\sqrt{1 + \lambda_{\text{L}}/\pi r^* S^2} - 1)} \tag{2.43}$$

where λ_{L} is the liquid bridge volume, γ_{L} is the surface tension, θ is the contact angle and S is the separation distance. To avoid S from being excessively small or negative during particle contact, a lower cut-off value of the separation distance S_{min} is employed. The upper cut-off value is given by the following rupture distance [51]:

$$S_{\text{rup}} = (1 + 0.5\theta)\lambda_{\text{L}}^{1/3} \tag{2.44}$$

A liquid bridge is formed when the particles come into contact, and then breaks when the separation distance reaches the rupture distance. The pendular liquid bridge force model used is only valid when the liquid to solid volume ratio is small. Under the specific conditions employed in this study, the film thickness is a few microns if the thickness is considered to be uniform, which is much smaller than the size of the original particle employed in the present work (5000 microns). Considering that this study aims to validate whether the coarse grain model of DEM can replicate the original DEM, if the same assumption is adopted to both original and scaled-up particles, the difference in film thickness at a micro level should not pose a challenge to the coarse grain model of DEM. Therefore the film thickness is ignored in the approaching stage.

2.3.2.2 JKR surface adhesion force model

Many models have been proposed to explain the surface adhesion force [44, 133, 134] which commonly make use of the surface energy. One of the most frequently used models

in DEM is based on the JKR theory [44, 135, 136, 45, 196], which is valid when the following dimensionless Tabor parameter, λ_{T}, is sufficiently large [203]:

$$\lambda_{\mathrm{T}} = \left(\frac{4r^{*}\gamma^{2}}{E^{*2}D_{\mathrm{min}}^{3}} \right)^{1/3} \tag{2.45}$$

where D_{min} is the minimum atomic separation distance between the particles. In the JKR theory, the normal adhesion force is calculated by:

$$\boldsymbol{F}_{\mathrm{JKR}} = 4\sqrt{\pi\gamma E^{*}a^{3}}\boldsymbol{e}_{ni,j} \tag{2.46}$$

In the original JKR model, this force can be exerted until the contact breaks during the separation process with negative overlap. A simplified model used in many studies [204, 196, 45] is employed in this work where the contact is assumed to be broken as soon as the normal overlap becomes zero.

2.3.3 Rolling resistance

In literature, both "rolling resistance" and "rolling friction" are employed to refer to the torques generated at particle contacts that impede particle rotation. Following Ai et al. [82], this study adopts the term "rolling resistance" that encompasses such torques. Many rolling resistance models are available and used with DEM [144, 145, 146, 65]. The Elastic-Plastic Spring-Dashpot model (EPSD model) and the Constant Directional Torque model (CDT model) are employed in this work to represent different types of inter-particle torques. The two models are used in Chapter 5 to validate whether the scaling laws of inter-particle torques can be applied to different types of torques or not.

2.3.3.1 EPSD model

The model used here is referred to as the EPSD2 model in LIGGGHTS that uses rolling spring to give the torque. The torque is incrementally computed as:

$$\boldsymbol{M}_{\mathrm{R}}(t+\Delta t) = \min(|\boldsymbol{M}_{\mathrm{R}}(t) + \Delta\boldsymbol{M}_{\mathrm{R}}|, \mu_{\mathrm{r}} r^* F_{\mathrm{N}})\boldsymbol{e}_{\mathrm{r}} \tag{2.47}$$

$$\boldsymbol{e}_r = \frac{\boldsymbol{M}_{\mathrm{R}}(t) + \Delta\boldsymbol{M}_{\mathrm{R}}}{|\boldsymbol{M}_{\mathrm{R}}(t) + \Delta\boldsymbol{M}_{\mathrm{R}}|} \tag{2.48}$$

$$\Delta\boldsymbol{M}_{\mathrm{R}} = -k_{\mathrm{r}}\Delta\boldsymbol{\theta}_{\mathrm{r}} \tag{2.49}$$

$$k_{\mathrm{r}} = 8G^*\sqrt{r^*\delta_{\mathrm{n}}}r^{*2} \tag{2.50}$$

where t is the time, Δt is the time step, μ_{r} is the coefficient of rolling resistance and $\Delta\boldsymbol{\theta}_r$ is the incremental deformation angle vector.

2.3.3.2 CDT model

The CDT model applies a constant torque on a particle which is always against the relative rotation between the particles [144, 205]. The torque is computed as:

$$\boldsymbol{M}_{\mathrm{R}} = -\mu_r r^* F_{\mathrm{N}} \frac{\boldsymbol{\omega}_{\mathrm{rel}}}{|\boldsymbol{\omega}_{\mathrm{rel}}|} \tag{2.51}$$

where $\boldsymbol{\omega}_{\mathrm{rel}}$ is the relative angular velocity.

2.4 Critical time step for DEM

The stability of numerical integration in DEM simulations with particle-particle interaction is significantly influenced by the chosen time step. Generally, a smaller time step leads to enhanced calculation stability. The computational cost will become excessively high if the time step is too small, rendering it challenging to accomplish the simulation within a reasonable time scale. Hence, when selecting the time step for DEM simulation,

it is crucial to consider both computational stability and the computational cost.

The literature presents two approaches for determining the critical time step in DEM. The first approach proposed by Cundall and Strack [122] for the linear spring model is based on the oscillation period of the mass-spring-dashpot system. The second approach is based on the speed of Rayleigh waves. In the simulation, it is assumed that all energy is transferred by means of Rayleigh waves [55]. The contact mechanics of non-adhesive particles in sandpiles were investigated by Li et al. [129] through a comparative numerical-experimental study. They utilised a non-linear spring model and proposed the expression for the Rayleigh time step as follows:

$$\Delta t \leq \frac{\pi f r_{\min}}{0.8766 + 0.163\nu} \sqrt{\frac{2\rho(1+\nu)}{E}} \tag{2.52}$$

where $r_{\min}$ denotes the minimum radius of the employed particles, and f is a safety factor and typically takes a value between 0.1 and 0.2, ρ is the particle density.

2.5 Integration scheme

After calculating the forces exerted on particles and determining the accelerations based on Newton's second law, the velocities and positions of particles can be evaluated through numerical integration. Various integration schemes have been employed in the previous works, such as symplectic Euler, position Verlet and velocity Verlet. The derivation of these schemes is based on the approximation of the Taylor series, which can be expressed as follows:

$$f(t+\Delta t) = f(t) + \frac{f'(t)}{1!}\Delta t + \frac{f''(t)}{2!}\Delta t^2 + \frac{f^{(3)}(t)}{3!}\Delta t^3 + \cdots \tag{2.53}$$

A first-order Taylor approximation can be employed to derive the first derivative $f'(t)$,

which provides the equation of forward difference approximation:

$$f'(t) = \frac{f(t + \Delta t) - f(t)}{\Delta t} \tag{2.54}$$

The standard Euler method based on the forward difference approximation is utilised to compute the first derivative for determining the velocities and positions of particles in the subsequent time step $(t + \Delta t)$:

$$\boldsymbol{v}(t + \Delta t) = \boldsymbol{v}(t) + \boldsymbol{a}(t)\Delta t \tag{2.55}$$

The backward difference approximation for the first derivative is derived by writing the Taylor series for the function at the previous time step, $f(t - \Delta t)$:

$$f'(t) = \frac{f(t) - f(t - \Delta t)}{\Delta t} \tag{2.56}$$

The symplectic Euler method differs from the standard Euler method in its calculation of position, as it employs a backward difference approximation. The new position can be expressed as follows:

$$\boldsymbol{x}(t + \Delta t) = \boldsymbol{x}(t) + \boldsymbol{v}(t)\Delta t \tag{2.57}$$

The position Verlet method is based on the central difference approximation. The first and second derivatives in Equation (2.53) are expressed as the Taylor polynomials of degree two and three, respectively. The position Verlet scheme is a second-order integrator and exhibits greater stability compared to the symplectic Euler scheme [206]. In which, the first derivative can be rewritten by the central difference approximation using Taylor polynomial of degree two, for the forward and backward directions as follows:

$$f(t + \Delta t) = f(t) + f'(t)\Delta t + \frac{f''(t)}{2}\Delta t^2 \tag{2.58}$$

$$f(t-\Delta t) = f(t) - f'(t)\Delta t + \frac{f''(t)}{2}\Delta t^2 \tag{2.59}$$

The central difference approximation for the first derivative can be obtained by subtracting Equation (2.59) from Equation (2.58):

$$f'(t) = \frac{f(t+\Delta t) - f(t-\Delta t)}{2\Delta t} \tag{2.60}$$

The second derivative can also be obtained by utilising the Taylor polynomial of degree three for both forward and backward time directions, yielding the subsequent expression:

$$f(t+\Delta t) = f(t) + f'(t)\Delta t + \frac{f''(t)}{2}\Delta t^2 + \frac{f^{(3)}(t)}{6}\Delta t^3 \tag{2.61}$$

$$f(t-\Delta t) = f(t) - (t)\Delta t + \frac{f''(t)}{2}\Delta t^2 - \frac{f^{(3)}(t)}{6}\Delta t^3 \tag{2.62}$$

The central difference approximation for the second derivative can be obtained by summing up Equations (2.61) and (2.62):

$$f''(t) = \frac{f(t+\Delta t) - 2f(t) - f(t-\Delta t)}{\Delta t^2} \tag{2.63}$$

The position Verlet method employs Equation (2.63) to compute the position:

$$\boldsymbol{x}(t+\Delta t) = 2\boldsymbol{x}(t) - \boldsymbol{x}(t-\Delta t) + \ddot{\boldsymbol{x}}(t)\Delta t^2 \tag{2.64}$$

The velocity can be derived based on Equation (2.60):

$$\boldsymbol{v}(t) = \frac{\boldsymbol{x}(t+\Delta t) - \boldsymbol{x}(t-\Delta t)}{2\Delta t} \tag{2.65}$$

The position Verlet method does not provide a velocity prediction for the next time step. To improve the position Verlet method, the velocity Verlet scheme is proposed,

which is a commonly utilised modification of the position Verlet method.

The velocity Verlet scheme [207] is employed in this study to numerically solve the equations of motion that governing the particles. According to Equation (2.58), the positions and velocities in the next time step can be determined as follows:

$$\boldsymbol{x}(t+\Delta t) = \boldsymbol{x}(t) + \boldsymbol{v}(t)\Delta t + \frac{1}{2}\dot{\boldsymbol{v}}(t)\Delta t^2 \tag{2.66}$$

$$\boldsymbol{v}(t+\Delta t) = \boldsymbol{v}(t) + \dot{\boldsymbol{v}}(t)\Delta t + \frac{1}{2}\ddot{\boldsymbol{v}}(t)\Delta t^2 \tag{2.67}$$

The position vector $\boldsymbol{x}(t)$ and the translational velocity $\boldsymbol{v}(t)$ are defined. The second derivative of the translational velocity, denoted as $\ddot{\boldsymbol{v}}(t)$, which is given by:

$$\ddot{\boldsymbol{v}}(t) = \frac{\dot{\boldsymbol{v}}(t+\Delta t) - \dot{\boldsymbol{v}}(t)}{\Delta t} \tag{2.68}$$

Substituting Equation (2.68) into Equation (2.67), the translational velocity at the next time step is finally determined as follows:

$$\boldsymbol{v}(t+\Delta t) = \boldsymbol{v}(t) + \frac{1}{2}(\dot{\boldsymbol{v}}(t+\Delta t) + \dot{\boldsymbol{v}}(t))\Delta t \tag{2.69}$$

Subsequently, the function of force evaluation is used to calculate the new acceleration $\dot{\boldsymbol{v}}(t+\Delta t)$, which is then utilised by the corrector to adjust the translational velocity in accordance with Equation (2.69).

The angular velocity of a particle can be determined using the same methodology as that for translational velocity, i.e., Equation (2.69). It is given by:

$$\boldsymbol{\omega}(t+\Delta t) = \boldsymbol{\omega}(t) + \frac{1}{2}(\dot{\boldsymbol{\omega}}(t+\Delta t) + \dot{\boldsymbol{\omega}}(t))\Delta t \tag{2.70}$$

The memory storage requirement of the velocity Verlet scheme is comparable to the position Verlet scheme, while the computation of the new acceleration is based on the

predicted velocity value rather than the corrected value.

The basic steps in the velocity Verlet algorithm are presented as follows, where the concept of half-step velocity and how to obtain Equation (2.69) from the half-step velocity are explained:

1. **Initially evaluate the half-step velocity**: Calculate an intermediate velocity at half the time step $(t + \frac{1}{2}\Delta t)$, using the velocity and acceleration at t:

$$\boldsymbol{v}\left(t + \frac{1}{2}\Delta t\right) = \boldsymbol{v}(t) + \frac{1}{2}\dot{\boldsymbol{v}}(t)\Delta t \tag{2.71}$$

2. **Update full step position**: Update the position using the intermediate velocity $\boldsymbol{v}\left(t + \frac{1}{2}\Delta t\right)$:

$$\boldsymbol{x}(t + \Delta t) = \boldsymbol{x}(t) + \boldsymbol{v}\left(t + \frac{1}{2}\Delta t\right)\Delta t \tag{2.72}$$

3. **Update the acceleration**: Compute the acceleration $\dot{\boldsymbol{v}}(t + \Delta t)$ from the interaction potential using the new position $\boldsymbol{x}(t + \Delta t)$, for instance, Equation (2.1) can be rewritten as follows:

$$m_i\dot{\boldsymbol{v}}_i(t + \Delta t) = \sum_j \boldsymbol{F}_{Ii,j}(\boldsymbol{x}(t + \Delta t)) + m_i\boldsymbol{g} \tag{2.73}$$

4. **Finish the update of velocity**: Complete the velocity update using the new acceleration:

$$\boldsymbol{v}(t + \Delta t) = \boldsymbol{v}\left(t + \frac{1}{2}\Delta t\right) + \frac{1}{2}\dot{\boldsymbol{v}}(t + \Delta t)\Delta t \tag{2.74}$$

substituting Equation (2.71) into Equation (2.74) yields:

$$\boldsymbol{v}(t + \Delta t) = \boldsymbol{v}(t) + \frac{1}{2}\dot{\boldsymbol{v}}(t)\Delta t + \frac{1}{2}\dot{\boldsymbol{v}}(t + \Delta t)\Delta t \tag{2.75}$$

which coincides Equation (2.69).

2.6 Closure

This chapter presents an overview of the fundamental concepts of discrete element method (DEM) and the governing equations employed in the simulations, which encompass particle motion description, particle interaction modelling, as well as determination of simulation time step and integration scheme.

In DEM, the motion of individual particles is traced while the collisions between particles are described using different methods, namely the hard-sphere models and the soft-sphere models. The hard-sphere models usually process a group of binary collisions in a predetermined order, without calculating the inter-particle overlaps or evaluating forces. In contrast, the soft-sphere models can simultaneously handle multiple collisions but requires accurate evaluation of inter-particle forces and torques.

The soft-sphere model of DEM is employed in this study due to the presence of a high concentration of particles in the investigated particulate systems, requiring consideration of multiple simultaneous collisions. In the soft-sphere model, various models have been employed to describe inter-particle forces and torques, which are introduced in three sections: contact force, attraction force, and rolling resistance.

The models employed to evaluate inter-particle forces and torques in this study are introduced. For describing the contact force between particles, the Hertz contact model and the JKR contact model are employed in the present work and introduced in Section 2.3.1. The JKR contact model is considered an extension of the Hertz model for describing adhesive contacts, which predicts a contact area relatively larger than that predicted by the Hertz model. The liquid-bridge force model and JKR surface adhesion force model, which are examples of inter-particle attraction forces, are utilised in this study and introduced in Section 2.3.2. The Elastic-Plastic Spring-Dashpot model (EPSD model) and the Constant Directional Torque model (CDT model) are employed in this study to evaluate the torque resources from rolling resistance on particles, as introduced in Section 2.3.3.

Subsequently, the critical time step for DEM simulation is introduced, along with a discussion on how to decide a reasonable time step for DEM simulations. The time step in the soft-sphere model of DEM must be carefully selected to avoid employing excessively large time steps that may lead to inaccurate calculations. On the other hand, DEM simulation is computationally expensive, especially when the number of particles is large. Therefore, it is also undesirable to adopt an extremely small time step, which would make the simulation difficult to complete in a reasonable time scale. Rayleigh time step is employed in the present work. The time step should be chosen to be smaller than the Rayleigh time step multiplied by a safety factor, with the typical range for the safety factor being between 0.1 and 0.2.

Finally, Section 2.5 introduced the velocity Verlet scheme, which is the integration scheme used in the present work. The velocity Verlet scheme is a method for integrating Newton's equations of motion. The basic steps in the velocity Verlet algorithm are as follows:

1. Calculate an intermediate velocity at half the time step.
2. Update the position using the intermediate velocity.
3. Compute the acceleration using the new position.
4. Complete the velocity update using the new acceleration.

Chapter 3

Coarse grain models of DEM

3.1 Introduction

In this chapter, the coarse grain model of DEM is introduced. Several coarse grain models of DEM have been proposed in the literature, and the general concept as well as classifications of these models are introduced in Section 3.2. The coarse grain models of DEM can be classified into two types [173] based on the employed scaling criterion. The first type is parameter scaling, which is explained in Section 3.2.1. The second type, called direct force scaling, is employed in the present study and is explained in Section 3.2.2.

In Section 3.3, a novel coarse grain model is proposed, which is called the scaled-up particle (SUP) model. The scaling laws employed in the SUP model are proposed in such a way that the bulk momentum change can be equivalent, which follows the previous works of Chan & Washino [173, 176]. In the concept of the scaling laws proposed by Chan & Washino, the number of particles is sufficiently large within single CVs, and the fluctuations of particle velocities and inter-particle forces can be ignored, which implies the model ignored some heterogeneous variables of the particles in CV. The previous works on porous media [208, 209] suggest that if the observer does not distinguish the microscopic heterogeneities of a porous system, this heterogeneous system can be effectively considered as homogeneous at macroscopic scale. This concept can also be applied to describe discrete

solid systems. In the present study, for simplicity in description, the author uses the term "effectively homogeneous assumption" as a name for the basic assumption of scaling laws proposed by Chan & Washino.

The most novel aspect of the SUP model is the proposed geometric similarity method for determining the overlap and separation distances between original particles, which is essential for estimating inter-particle forces and torques. Based on the effectively homogeneous assumption of particles in CV, this study derived scaling laws for particles with particle size distributions (PSDs). To apply the scaling laws to particles with PSD, the effectively homogeneous assumption cannot be limited only to variables of particles, and it must be extended to PSDs as well. If the particles in the simulation can be considered effectively homogeneous, then theoretically, the SUP model can be applied to scale any type of forces and torques exerted on DEM particles [177, 178, 154].

3.2 Classifications of coarse grain models

The coarse grain model of DEM is a promising approach for reducing the computational cost of DEM simulations, wherein particle size is artificially increased to effectively decrease the total number of particles in a given system. Several coarse grain models of DEM have been proposed in the literature [165, 167, 210, 169, 173]. Chen and Washino [173] proposed a classification criterion that categorised coarse grain models into two types, namely parameter scaling and direct force scaling. Figure 3.1 illustrates the simulation process differences between direct force scaling and parameter scaling.

In parameter scaling, the properties of particles are adjusted to maintain kinematic consistency between the scaled-up particle system and the original particle system. However, finding a suitable scale criterion can be challenging, particularly when dealing with systems involving multiple types of forces.

The direct force scaling first evaluates the force acting on original particles, and directly scales the forces for the scaled-up particles. The implementation of direct force

scaling may require additional coding efforts, but it offers the advantage of establishing a generic criterion applicable to multiple types of forces.

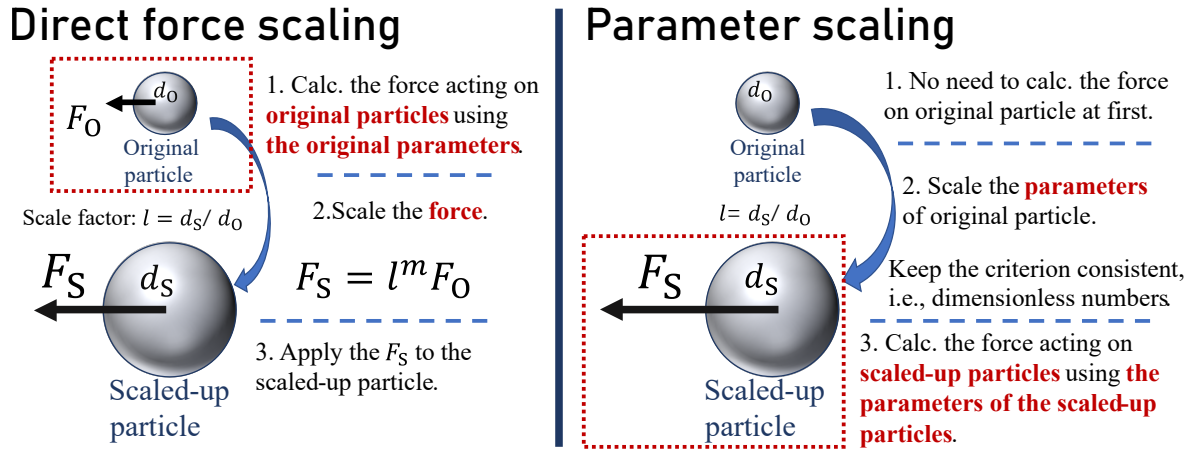

Figure 3.1: The difference in implementation processes between direct force scaling and parameter scaling is demonstrated, where d represents the diameter of the particle. Subscripts "$_S$" and "$_O$" indicate that the variables belong to scaled-up particles and original particles, respectively.

3.2.1 Parameter scaling

In order to achieve kinematic similarity between the coarse grained particle system and the original particle system, the parameter scaling [139, 168, 174, 175] adjusts the physical properties and other parameters of DEM particles.

Bierwisch et al. [139] proposed a coarse grain model to investigate the rapid granular flow from a moving container and the formation of repose angle, which is derived from the concept that the energy density and its evolution between the coarse grain particles and original particles should be consistent. The coarse grain model successfully reproduced the volume fractions and coordination numbers observed in particle beds composed of original particles.

Thakur et al. [168] investigated the compression behaviour of cohesionless and cohesive particle beds. In the parameter scaling of Thakur et al., both the loading and unloading stiffness in normal and tangential directions are scaled with particle size. This implies

that the inter-particle contact force should be proportional to the square of the particle radius. Following their coarse grain model [139, 168], the inter-particle forces can be scaled as follows:

$$|\boldsymbol{F}_{\mathrm{IS}}| \propto r_{\mathrm{AveS}}^2 \tag{3.1}$$

where $|\boldsymbol{F}_{\mathrm{IS}}|$ represents the magnitude of the inter-particle force exerted on the scaled-up particles, and r_{AveS} denotes the average radius of the scaled-up particles.

Jiang et al. [174] developed a coarse grain model in CFD-DEM simulation to investigate the multi-phase flow in vibrated fluidised bed. In terms of keeping the consistency between the original and the scaled-up DEM particles, their study employs a set of dimensionless numbers, such as the coefficient of restitution and the friction coefficient of DEM particles, ensuring that these dimensionless parameters are equal between the original and coarse-grained CFD-DEM systems. Kosaku et al. [175] proposed a coarse grain model with a systematic parameter scaling law for adhesion forces, especially liquid bridge forces, based on the assumption of energy conservation before and after employing the coarse grain model.

In summary, parameter scaling is simple in terms of implementation, because it does not require any additional coding. However, the scaling criterion of each parameter depends on the force models used and can be difficult or even impossible to determine for complex forms of forces. In parameter scaling, the scaling of force is occasionally referred [168], where the forces exerted on the particles are not considered as the primary parameter but rather emerge as a consequence of deriving the scaling law.

3.2.2 Direct force scaling

Another approach to conduct coarse-grained DEM simulation is the direct force scaling [165, 169, 173], where the forces acting on original particles are first estimated using the original particle properties and variables, and then directly scaled to apply to scaled-up

particles.

Figure 3.2 illustrates the procedure of conducting a simulation with the direct force scaling. Initially, as an initial step for simulating direct force scaling, the parameters of the scaled-up particle are already known. Consequently, the original particle variables must be evaluated based on the input variables of the scaled-up particles. Subsequently, the forces acting on the original particles can be computed using the original variables, following the procedure of the conventional DEM simulation. Finally, the forces exerted on the original particles are directly scaled, and the scaled forces are employed to solve the motion of scaled-up particles.

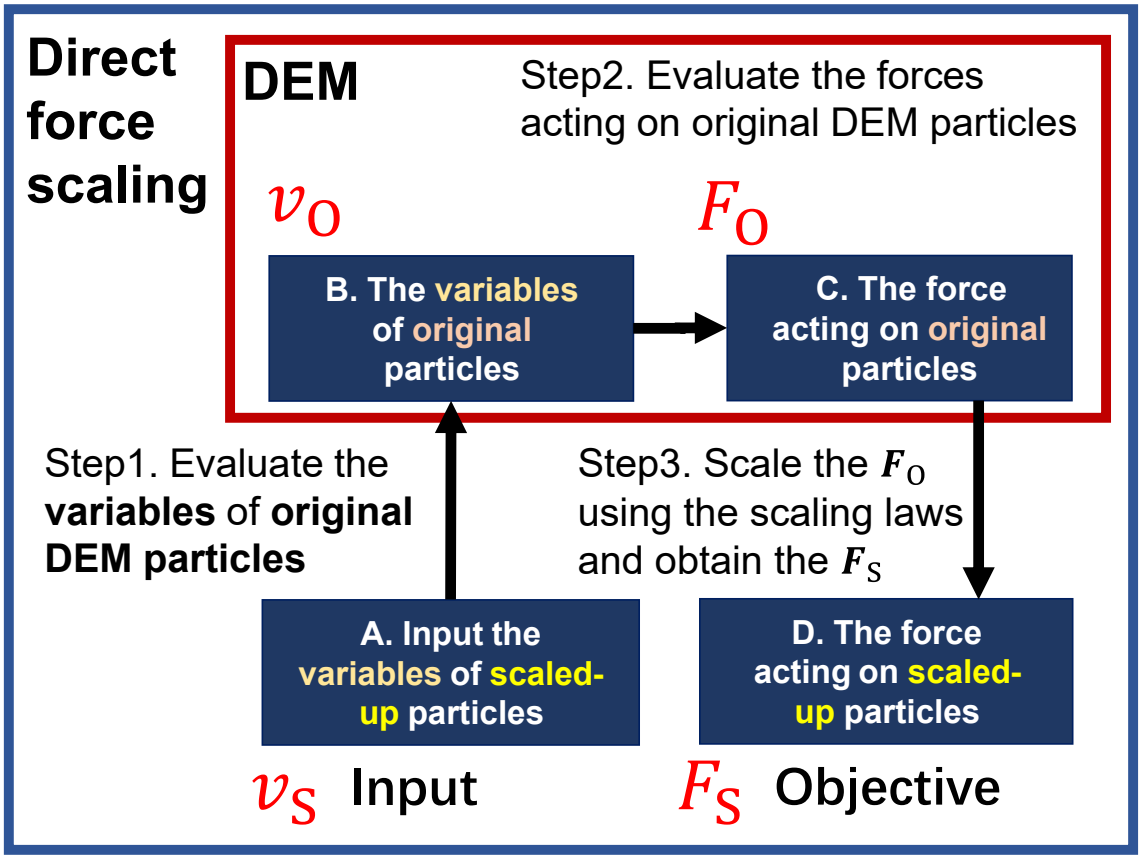

Figure 3.2: The process of evaluating forces on the scaled-up particle using direct force scaling.

The scale factor l is employed to represent the size ratio between the original particle

and the scaled-up particle. For the spherical particles the scale factor l can be given by:

$$l = \frac{d_{\mathrm{S}}}{d_{\mathrm{O}}} \tag{3.2}$$

where d_{S} is the diameter of the scaled-up particle, and d_{O} is the diameter of the original particle. For non-spherical particles, the scale factor l can be defined as:

$$l^3 = \frac{m_{\mathrm{AveS}}}{m_{\mathrm{AveO}}} \tag{3.3}$$

where m_{AveS} and m_{AveO} are the average mass of scaled-up particles and original particles, respectively.

In the direct force scaling approach, the force and torque applied on the scaled-up particle are l^m times larger than those of the original particle where m is called the scale power index. As shown in Figure 3.1, the scaling of force is essential in the direct force scaling, where the force acting on scaled-up particle $\boldsymbol{F}_{\mathrm{S}}$ is given by:

$$\boldsymbol{F}_{\mathrm{S}} = l^m \boldsymbol{F}_{\mathrm{O}} \tag{3.4}$$

where $\boldsymbol{F}_{\mathrm{O}}$ is the force exerted on the original particle, which is evaluated from the properties and parameters of the original particles. The scale power index m may vary for different types of forces, which is also crucial in distinguishing the various scaling laws of direct force scaling.

Several scale power indices have been proposed in the literature. Sakai and Koshizuka [165] proposed $m = 3$ for the contact, fluid and gravitational forces to keep the same equations of motion between the original and scaled-up systems in the particle level. In other words, the same scale power index is applied to both inter-particle and body forces:

$$\boldsymbol{F}_{\mathrm{IS}} = l^3 \boldsymbol{F}_{\mathrm{IO}} \tag{3.5}$$

$$\boldsymbol{F}_{\mathrm{BS}} = l^3 \boldsymbol{F}_{\mathrm{BO}} \tag{3.6}$$

$m = 4$ is assigned to the contact torque in their formulation as:

$$\boldsymbol{M}_{\mathrm{IS}} = r_{\mathrm{S}} \boldsymbol{n} \times \boldsymbol{F}_{\mathrm{IS}} = l r_{\mathrm{O}} \boldsymbol{n} \times l^3 \boldsymbol{F}_{\mathrm{IO}} = l^4 \boldsymbol{M}_{\mathrm{IO}} \tag{3.7}$$

Sakai et al. [166] inherited the same indices except that $m = 2$ is used for the van der Waals force to maintain the same potential energy. Their scale power indices are summarised in Table 3.1.

Table 3.1: Scale power indices of Sakai and Koshizuka and Sakai et al. [165, 166].

Scale power index	Force / torque type	Classification
4	Torque	Interparticle
3	Gravity	Body
3	Fluid force (CFD-DEM)	Body
3	Contact force	Interparticle
2	van der Waals force	Interparticle

Chu et al. [169] proposed a model that attempts to maintain the same total impulse, which also leads to l^3 scaling for fluid and gravitational forces. However, deriving a scaling law for contact force in their model poses challenges due to the requirement of a priori knowledge of the contact duration. Nevertheless, they suggested l^2 scaling based on the assumption that the contact duration is linearly proportional to the particle size. Their scale power indices are summarised in Table 3.2.

Table 3.2: Scale power indices of Chu et al. [169].

Scale power index	Force / torque type	Classification
3	Torque	Interparticle
3	Gravity	Body
3	Fluid force (CFD-DEM)	Body
2	Contact force	Interparticle

The present study developed and validated a coarse grain model called the scaled-up particle (SUP) model, which will be introduced in the subsequent section.

3.3 The scaled-up particle (SUP) model

The present section introduces the scaled-up particle (SUP) model, a novel coarse grain model of DEM that can be applied to various types of inter-particle forces and torques. The derivation of the SUP model is not specific to any specific type of force. The scaling laws are derived in such a way that the changes of momentum in control volumes are equivalent between original and scaled-up particles, which ensure similarity not at the particle level but within the control volume. The number of particles in CV should be large enough that the fluctuations of velocity at the particle level can be ignored. The concept of deriving scaling laws in the SUP model was first proposed by Chan et al. [173] and subsequently demonstrated to be applicable to arbitrary particle flow by Washino [176]. The present study extended the scaling laws to particles with PSDs, which is illustrated in Figure 3.3.

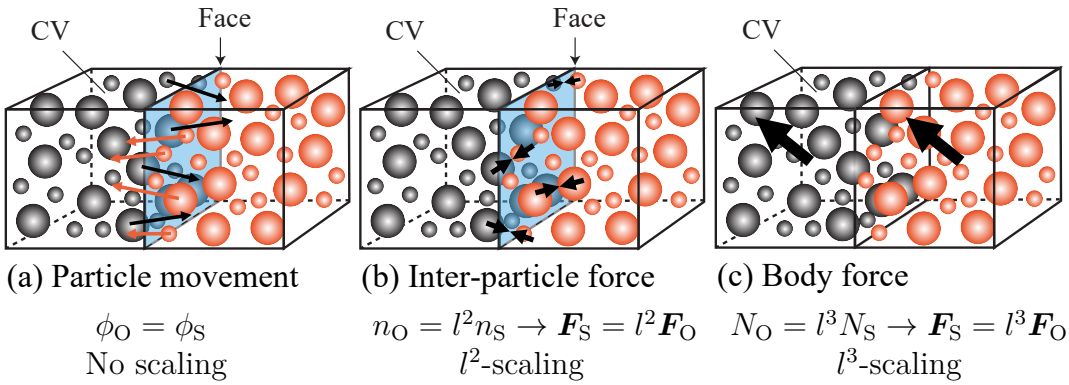

Figure 3.3: The momentum change mechanisms in a control volume include: (a) Momentum flux resulting from particle movement, (b) Stress due to inter-particle forces, and (c) Momentum source due to body forces. ϕ represents the mass flux across the Control Volume (CV) face, n denotes the number of particles interacting across CV face, and N signifies the number of particles within CV.

Figures 3.3(a), 3.3(b), and (c) illustrate three mechanisms that contribute to the momentum on a CV scale, which will be sequentially introduced. The movement of particles, as shown in Figure 3.3 (a), is related to the mass flux across the CV face, which should be consistent between the scaled-up particle system and the original system.

According to this scaling law, the translational velocity of the original particle should be equal to that of the scaled-up particle. Since the number of original particles inside the control volume, N, is l^3 times larger than that of the scaled-up particles, i.e. $N_{\mathrm{S}} = N_{\mathrm{O}}/l^3$, the derivation of the scaling laws by Chan & Washino does not explicitly mention particle size distributions, but it can actually be applied to particles with PSDs. The applicability of the scaling laws to particles with PSDs is conceptualised in this section.

Assuming that the particles have a discrete particle size distribution, the dimensionless diameter $\tilde{d}_i$ for each specific particle size that indexed by i is defined as the ratio of its diameter d_i to the maximum diameter $d_{N_{\max}}$ in the set:

$$\tilde{d}_i = \frac{d_i}{d_{N_{\max}}} = \frac{d_{\mathrm{O},i}}{d_{\mathrm{O},N_{\max}}} = \frac{d_{\mathrm{S},i}}{d_{\mathrm{S},N_{\max}}} \tag{3.8}$$

For a given set of discrete dimensionless particle sizes indexed by i, where $\tilde{d}_i$ is the diameter for each index i. The mass of each original particle m_{O} can be written as a function of its diameter d_{O}:

$$m_{\mathrm{O},i} = m_{\mathrm{O}}(\tilde{d}_i, d_{\mathrm{O},N_{\max}}) \tag{3.9}$$

The same form for the mass of scaled-up particles can be written as:

$$m_{\mathrm{S},i} = m_{\mathrm{S}}(\tilde{d}_i, d_{\mathrm{S},N_{\max}}) \tag{3.10}$$

The term $w_{\mathrm{O},i}$ represents the proportion of particles with a specific size in relation to the total number of particles. The sum of all $w_{\mathrm{O},i}$ from $i = 1$ to $i = N_{\max}$ equals 1.

$$\sum_{i=1}^{N_{\max}} w_{\mathrm{O},i} = 1 \tag{3.11}$$

For a given $w_{\mathrm{O},i}$ there is a equal $w_{\mathrm{S},i}$, i.e. $w_{\mathrm{S},i} = w_{\mathrm{O},i}$. The conservation of total particle

mass in a CV for original particles and scaled-up particles is given as follows:

$$\sum_{i=1}^{N_{\max}} N_{\mathrm{S}} w_{\mathrm{S},i} m_{\mathrm{S},i} = \sum_{i=1}^{N_{\max}} N_{\mathrm{O}} w_{\mathrm{O},i} m_{\mathrm{O},i} \tag{3.12}$$

The corresponding relationships of the parameters with different size particle can be find in Table 3.3.

Index i	Dimensionless particle size $\tilde{d}_i$	Particle mass m_i	The weight of particle number w_i
1	$\tilde{d}_1$	m_1	w_1
2	$\tilde{d}_2$	m_2	w_2
3	$\tilde{d}_3$	m_3	w_3
$\vdots$	$\vdots$	$\vdots$	$\vdots$
n	$\tilde{d}_n$	m_n	w_n
$\vdots$	$\vdots$	$\vdots$	$\vdots$
$N_{\max}$	$\tilde{d}_{N_{\max}}$	$m_{N_{\max}}$	$w_{N_{\max}}$

Table 3.3: Subscript i corresponding to Dimensionless particle sizes $\tilde{d}_i$, particle mass m_i and w_i the weight of particle number for the specific particle size $\tilde{d}_i$

The momentum flux due to the movement of particles can be written as a sum of different size particles in one CV:

$$\frac{1}{V_{\mathrm{CV}}} \sum_{i=1}^{N_{\max}} N_{\mathrm{S}} w_{\mathrm{S},i} m_{\mathrm{S},i} \boldsymbol{v}_{\mathrm{S},i} (\boldsymbol{v}_{\mathrm{S},i} \cdot \boldsymbol{n}_{\mathrm{face}}) = \frac{1}{V_{\mathrm{CV}}} \sum_{i=1}^{N_{\max}} N_{\mathrm{O}} w_{\mathrm{O},i} m_{\mathrm{O},i} \boldsymbol{v}_{\mathrm{O},i} (\boldsymbol{v}_{\mathrm{O},i} \cdot \boldsymbol{n}_{\mathrm{face}}) \tag{3.13}$$

Substitute Equation (3.12) into the right side of Equation (3.13), and derive the following expression:

$$\boldsymbol{v}_{\mathrm{S},i} (\boldsymbol{v}_{\mathrm{S},i} \cdot \boldsymbol{n}_{\mathrm{face}}) = \boldsymbol{v}_{\mathrm{O},i} (\boldsymbol{v}_{\mathrm{O},i} \cdot \boldsymbol{n}_{\mathrm{face}}) \tag{3.14}$$

In equations (3.13), V_{CV} represents the volume of the control volume, and $\boldsymbol{n}_{\mathrm{face}}$ indicates

the unit vector perpendicular to the face. Equations (3.12), (3.13), and (3.14) indicate that for the same CV, there is no need to scale the momentum flux due to the movement of particles, and the velocity of scaled-up particles does not need to be scaled either.

A significant advantage of the SUP model is that it provides a set of scaling laws that can be universally applied to scale different forces, namely l^2 scaling for all inter-particle forces and torques, as well as l^3 scaling for any body forces. In Figures 3.3 (b) and (c), the mechanisms of force scaling are depicted, which are explained in the subsequent Section 3.3.1. The scale power indices of the SUP model are summarised in Table 3.4, where the scaling law of inter-particle torques is explained in Section 3.3.3.

Table 3.4: Scale power indices of the SUP model [173, 176, 177, 178].

Scale power index	Force / torque type	Classification
2	Torque	Interparticle
3	Gravity	Body
3	Fluid drag force (CFD-DEM)	Body
2	Contact force	Interparticle
2	Attraction force	Interparticle

3.3.1 Scaling laws of forces

With respect to the inter-particle force, as illustrated in Figure 3.3 (b), the translational momentum flux across the control volume (CV) face should be consistent, regardless of whether scaled-up particles or original particles are employed. In the field of continuum mechanics, it is well recognised that stresses acting on a surface can be equivalently interpreted as momentum fluxes across that surface, as demonstrated in foundational texts [22]. The total momentum flux (ϕ) across a control volume (CV) face, resulting from both inter-particle forces and particle motion, can be described as follows:

$$\phi = \phi_{\text{I-P-Force}} + \phi_{\text{motion}} \tag{3.15}$$

where the term ϕ_{motion} represents the momentum flux resources from particle motion, which has been previously discussed. The $\phi_{\text{I-P-Force}}$ represents the momentum flux resources from inter-particle force and will be discussed below.

The scaling laws derivation considers particles with different PSDs as an extension of the inter-particle forces scaling laws proposed by Chan & Washino [173, 176]. The momentum exchange of inter-particle force occurs at a given interface between two given CVs, and the projection area of the particles at the interface should be equal between the scaled-up particles and the original particles. Especially for compactly arranged particles, a given interface area cannot accommodate proportionally enlarged particles without reducing the number of particles. According to this rule, the relationship of particles number on the face can be given by:

$$\sum_{i=1}^{N_{\max}} n_{\text{S}} w_{\text{S},i} A_{\text{S},i} = \sum_{i=1}^{N_{\max}} n_{\text{O}} w_{\text{O},i} A_{\text{O},i} \tag{3.16}$$

where n_{O} and n_{S} represent the number of particles on the interface of the original and scaled-up particles, respectively. $A_{\text{O},i}$ and $A_{\text{S},i}$ represent the projection area for an individual original particle and a scaled-up particle, respectively, in a specific dimensionless diameter $\tilde{d}_i$. The implicit assumption here is that the particle size distribution is similar for particles at the interface as it is within the entire CV, which is an extension requirement of applying the effectively homogeneous assumption to particles with PSDs. The projection area of spherical particles can be written as:

$$A_{\text{O},i} = \frac{\pi}{4} d_{\text{O},i}^2 \tag{3.17}$$

$$A_{\text{S},i} = \frac{\pi}{4} d_{\text{S},i}^2 \tag{3.18}$$

To calculate the scaling ratio of the projected areas, divide the scaled area by the original

area:

$$\frac{A_{\mathrm{S},i}}{A_{\mathrm{O},i}} = \frac{d_{\mathrm{S},i}^2}{d_{\mathrm{O},i}^2} = l^2 \tag{3.19}$$

Rearrange Equation (3.19), and the relationship between $A_{\mathrm{S},i}$ and $A_{\mathrm{O},i}$ can be obtained:

$$A_{\mathrm{S},i} = l^2 A_{\mathrm{O},i} \tag{3.20}$$

Substitute Equation (3.20) into Equation (3.16), the relationship of particle numbers on the across face between two given CVs can be obtained:

$$n_{\mathrm{O}} = l^2 n_{\mathrm{S}} \tag{3.21}$$

Considering the particle size distributions, the average stress σ on an interface between two CVs of original and scaled-up particles is respectively given by:

$$\sigma_{\mathrm{O}} = \frac{1}{A_{\mathrm{face}}} \sum_{i=1}^{N_{\max}} n_{\mathrm{O}} w_{\mathrm{O},i} \boldsymbol{F}_{\mathrm{IO},i} \cdot \boldsymbol{n}_{\mathrm{face}} \tag{3.22}$$

$$\sigma_{\mathrm{S}} = \frac{1}{A_{\mathrm{face}}} \sum_{i=1}^{N_{\max}} n_{\mathrm{S}} w_{\mathrm{S},i} \boldsymbol{F}_{\mathrm{IS},i} \cdot \boldsymbol{n}_{\mathrm{face}} \tag{3.23}$$

To ensure a consistent stress on the CV face, i.e. $\sigma_{\mathrm{O}} = \sigma_{\mathrm{S}}$, the relationship between inter-particle forces in the scaled-up particle system and the original system can be described as:

$$\frac{n_{\mathrm{O}}}{A_{\mathrm{face}}} \sum_{i=1}^{N_{\max}} w_{\mathrm{O},i} \boldsymbol{F}_{\mathrm{IO},i} \cdot \boldsymbol{n}_{\mathrm{face}} = \frac{n_{\mathrm{S}}}{A_{\mathrm{face}}} \sum_{i=1}^{N_{\max}} w_{\mathrm{S},i} \boldsymbol{F}_{\mathrm{IS},i} \cdot \boldsymbol{n}_{\mathrm{face}} \tag{3.24}$$

where A_{face} represents the area of the CV face. The following equation can be derived by substituting Equation (3.21) into Equation (3.24):

$$\frac{n_{\mathrm{S}} \sum_{i=1}^{N_{\max}} w_{\mathrm{S},i} \boldsymbol{F}_{\mathrm{IS},i} \cdot \boldsymbol{n}_{\mathrm{face}}}{A_{\mathrm{face}}} = \frac{(l^2 n_{\mathrm{S}}) \sum_{i=1}^{N_{\max}} w_{\mathrm{O},i} \boldsymbol{F}_{\mathrm{IO},i} \cdot \boldsymbol{n}_{\mathrm{face}}}{A_{\mathrm{face}}} \tag{3.25}$$

Rearrangement of this equation yields:

$$\sum_{i=1}^{N_{\max}} w_{\mathrm{S},i}\boldsymbol{F}_{\mathrm{IS},i}\cdot\boldsymbol{n}_{\mathrm{face}} = l^2\sum_{i=1}^{N_{\max}} w_{\mathrm{O},i}\boldsymbol{F}_{\mathrm{IO},i}\cdot\boldsymbol{n}_{\mathrm{face}} \tag{3.26}$$

Because the weight of particle number is equal between scaled-up and original particles ($w_{\mathrm{S},i} = w_{\mathrm{O},i}$), it can be assumed that the force should be uniformly scaled-up for any single particle size. Following this assumption, the relationship of inter-particle forces can be simplified to:

$$\boldsymbol{F}_{\mathrm{IS},i} = l^2\boldsymbol{F}_{\mathrm{IO},i} \tag{3.27}$$

Equation (3.27) suggests that the inter-particle forces should be scaled by l^2, i.e. the l^2-scaling. Since the derivation does not involve any specific type of force, it implies that the l^2-scaling can be universally applicable to any inter-particle force.

Regarding the scaling law of body force, as depicted in Figure 3.3 (c), regardless of whether scaled-up or original particles are employed, the body force exerted on CV should be consistent, which can be written as:

$$\frac{N_{\mathrm{O}}}{V_{\mathrm{CV}}}\sum_{i=1}^{N_{\max}} w_{\mathrm{O},i}\boldsymbol{F}_{\mathrm{BO},i} = \frac{N_{\mathrm{S}}}{V_{\mathrm{CV}}}\sum_{i=1}^{N_{\max}} w_{\mathrm{S},i}\boldsymbol{F}_{\mathrm{BS},i} \tag{3.28}$$

On the other hand, employing scaled-up particles should not change the total mass of particles within the CV, which can be written as:

$$N_{\mathrm{O}} = l^3 N_{\mathrm{S}} \tag{3.29}$$

By substituting Equation (3.29) into Equation (3.28), the following equation is obtained:

$$\boldsymbol{F}_{\mathrm{BO},i}(l^3 N_{\mathrm{S}}) = \boldsymbol{F}_{\mathrm{BS},i}N_{\mathrm{S}} \tag{3.30}$$

Rearrangement of this equation yields:

$$\boldsymbol{F}_{\mathrm{BS},i} = l^3 \boldsymbol{F}_{\mathrm{BO},i} \tag{3.31}$$

Equation (3.31) suggests that the body force should be scaled by l^3, i.e. the l^3-scaling, and the derived scaling law is applicable for the particles with size distributions. Since the derivation does not involve any specific type of force, it implies that the l^3-scaling is universally applicable to any body force.

The scaling laws proposed by Chan and Washino [161, 176] are derived in such a way that the bulk momentum change can be regarded as equivalent between original and scaled-up particles in a given control volume. When the number of particles (both original and scaled-up) in a given CV is sufficiently large, at the CV scale, the fluctuations of velocity and forces at the single particle scale can be ignored. Furthermore, in this study, it is assumed that the particle size distributions are spatially averaged within the control volume (CV). As a result, scaling laws for particles with size distributions are derived, which have the same form as the scaling laws derived from mono-disperse particles.

Firstly, with regard to particle movement, e.g., the translational velocity of particles, no scaling is applied. For any inter-particle force, such as inter-particle contact force and attraction force, l^2-scaling is employed. In the present work, the liquid-bridge force and JKR surface adhesion force are employed to investigate the scaling of inter-particle attraction force.

l^3-scaling is employed to scale the body force acting on the CV, in the present work, the only employed body force is gravity. The derivations of these scaling laws are not limited to any specific force, indicating they may be theoretically applicable to any type of force. These three scaling laws should be applied as long as the particles follow the effectively homogeneous assumption.

3.3.2 Evaluation of original particle variables

In scaled-up particle simulation, original particles are not explicitly used but represented by scaled-up particles. Therefore, it is crucial to accurately evaluate the original particle variables from those of the scaled-up particles to estimate the forces acting on the original particles. These variables include the particle translational velocity, angular velocity, particle overlap and separation distance. Sakai and Koshizuka [165] suggested that the translational velocity of the original particle should be the same as that of the scaled-up particle from the translational kinetic energy point of view:

$$\boldsymbol{v}_{\mathrm{O}} = \boldsymbol{v}_{\mathrm{S}} \tag{3.32}$$

It is also proven that the same translational velocity maintains the convective momentum flux across the faces of control volumes by Washino et al. [176]. The angular velocity is scaled by l to keep the same rotational kinetic energy between the original and scaled-up systems:

$$\boldsymbol{\omega}_{\mathrm{O}} = l\boldsymbol{\omega}_{\mathrm{S}} \tag{3.33}$$

These relationships for velocities have a solid theoretical basis and seem to be reasonable. In contrast, the evaluation methods of particle overlap and separation distance are not well-grounded. Sakai and Koshizuka [165] assumed that the overlap of the original particle is the same as that of the scaled-up particle, and Chan and Washino [173] employed the same idea for separation distance, that is:

$$\delta_{\mathrm{O}} = \delta_{\mathrm{S}} \tag{3.34}$$

$$S_{\mathrm{O}} = S_{\mathrm{S}} \tag{3.35}$$

Based on geometric similarity concept, a new method is proposed in the present work

to evaluate the variables of original particles in direct force scaling. Particularly, it focuses on the evaluation of original particle variables and it is suggested that to use geometric similarity for both particle overlap and separation distance. In other words, they are scaled by the scale factor l to ensure the same amount of mass to be accommodated in a fixed space. By employing the concept of geometric similarity, the overlap and separation distances should be evaluated as follows:

$$\delta_{\mathrm{O}} = \delta_{\mathrm{S}}/l \tag{3.36}$$

$$S_{\mathrm{O}} = S_{\mathrm{S}}/l \tag{3.37}$$

The key to the proposed coarse grain model is to keep the same flows in the control volume level between the original and scaled-up systems. The present work assumes that a sufficient number of discrete particles are effectively homogeneous within the control volume. As shown in Figure 3.4, the relationships given by Equations (3.36) and (3.36) are required to accommodate the same mass in the control volume, i.e. $m_{\mathrm{O}}n^3 = m_{\mathrm{S}}n^3/l^3$, where n is the number of particles aligned in one dimension. The relationships of the variables between the original and scaled-up particles are summarised in Table 3.5. As a supplementary explanation, in the direct force scaling, the force acting on the original particle is first evaluated using the original particle parameters and variables, which include the liquid bridge volume, minimum separation distance and rupture distance.

Table 3.5: Relationships of the original and scaled-up variables.

Variable	Previous work [165, 166, 173, 176]	Present work [177]
Translational velocity	$\boldsymbol{v}_{\mathrm{O}} = \boldsymbol{v}_{\mathrm{S}}$	$\boldsymbol{v}_{\mathrm{O}} = \boldsymbol{v}_{\mathrm{S}}$
Rotational velocity	$\boldsymbol{\omega}_{\mathrm{O}} = l\boldsymbol{\omega}_{\mathrm{S}}$	$\boldsymbol{\omega}_{\mathrm{O}} = l\boldsymbol{\omega}_{\mathrm{S}}$
Particle overlap	$\delta_{\mathrm{O}} = \delta_{\mathrm{S}}$	$\delta_{\mathrm{O}} = \delta_{\mathrm{S}}/l$
Separation distance	$S_{\mathrm{O}} = S_{\mathrm{S}}$	$S_{\mathrm{O}} = S_{\mathrm{S}}/l$

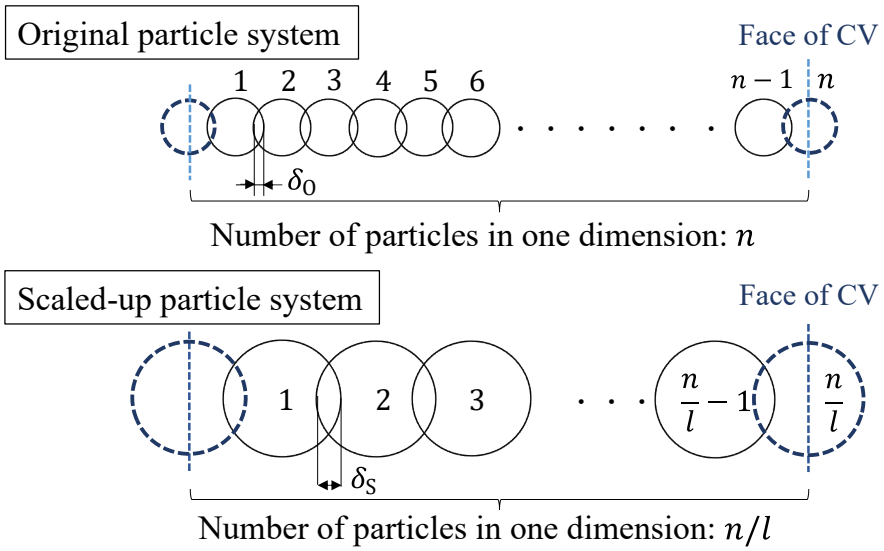

(a) Particle overlap

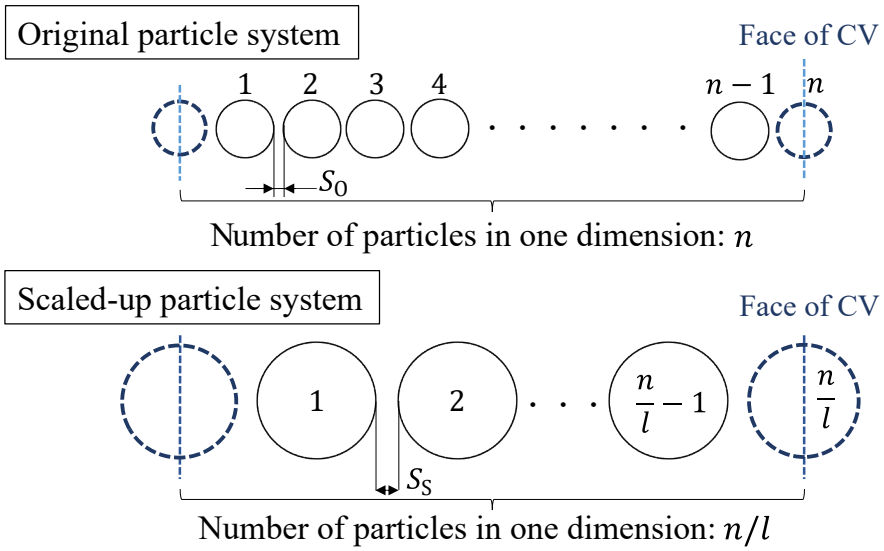

(b) Separation distance

Figure 3.4: Geometric similarity in control volume (1-dimension).

3.3.3 Scaling law of torques

The comparison of torque scaling concept between the SUP model and conventional coarse grain model is shown in Figure 3.5. In several previous works of coarse grain models, including those proposed by Sakai and Koshizuka [165] as well as Chu et al. [169], the torques are computed using the conventional procedure for discrete element method (DEM) particles. In other words, the torques are given by using the particle radius and forces which are both already "scaled-up". For example, in the previous work of Chu et al. [169] the scaling laws of inter-particle forces and torques are given by:

$$\boldsymbol{F}_{\mathrm{IS}} = l^2 \boldsymbol{F}_{\mathrm{IO}} \tag{3.38}$$

$$r_{\mathrm{S}} = l r_{\mathrm{O}} \tag{3.39}$$

where r_{S} and r_{O} are the radii of scaled-up particle and original particle respectively.

$$|\boldsymbol{M}_{\mathrm{IO}}| \propto |\boldsymbol{F}_{\mathrm{IO}}| r_{\mathrm{O}} \tag{3.40}$$

$$|\boldsymbol{M}_{\mathrm{IS}}| \propto |\boldsymbol{F}_{\mathrm{IS}}| r_{\mathrm{S}} \tag{3.41}$$

where $|\boldsymbol{M}_{\mathrm{IS}}|$ and $|\boldsymbol{M}_{\mathrm{IO}}|$ are the magnitude of inter-particle torques of scaled-up particle and original particle, respectively. Then, substitute Equations (3.38) and (3.39) into Equation (3.41) results in:

$$|\boldsymbol{M}_{\mathrm{IS}}| \propto l^3 |\boldsymbol{F}_{\mathrm{IO}}| r_{\mathrm{O}} \tag{3.42}$$

Substitute Equation (3.40) into Equation (3.42) results in:

$$|\boldsymbol{M}_{\mathrm{IS}}| \propto l^3 |\boldsymbol{M}_{\mathrm{IO}}| \tag{3.43}$$

Equation (3.43) implies the l^3-scaling is employed to scale the inter-particle torques.

In the SUP model, the torques on the original particles are first evaluated and then scaled so that the total change of angular momentum in control volumes is the same between scaled-up and original particles. This concept is totally different from that of conventional models. In this way, the scaling law of inter-particle torques coincides with that of inter-particle forces:

$$\boldsymbol{F}_{\mathrm{IS}} = l^2 \boldsymbol{F}_{\mathrm{IO}} \tag{3.44}$$

$$\boldsymbol{M}_{\mathrm{IS}} = l^2 \boldsymbol{M}_{\mathrm{IO}} \tag{3.45}$$

Equation (3.45) is derived in a similar manner to the scaling laws for inter-particle forces discussed in Section 3.3.1. The exchange of angular momentum between CVs must occur through particle contact, with particles in contact being located at the interface.

3.3.4 Scaling of time step

In this section, a head-on collision of two particles is considered to discuss the scaling of the stable time step. When two original particles are in contact, the equation of motion can be written using the Hertzian contact theory as:

$$m^*_{\mathrm{O}} \frac{dv_{r\mathrm{O}}}{dt} = -\frac{4}{3} E^* r^{*1/2}_{\mathrm{O}} \delta^{3/2}_{\mathrm{O}} \tag{3.46}$$

where the v_r is the relative velocity and δ is the normal overlap. Since the time step in DEM is usually determined based on the contact force alone in the literature [94, 129], any cohesion force is ignored here for simplicity. Employing the geometric similarity and l^2 scaling law, the equation of motion for two colliding scaled-up particles is given as:

$$m^*_{\mathrm{S}} \frac{dv_{r\mathrm{S}}}{dt} = -\frac{4}{3} E^* r^{*1/2}_{\mathrm{O}} \left(\frac{\delta_{\mathrm{S}}}{l} \right)^{3/2} l^2 \tag{3.47}$$

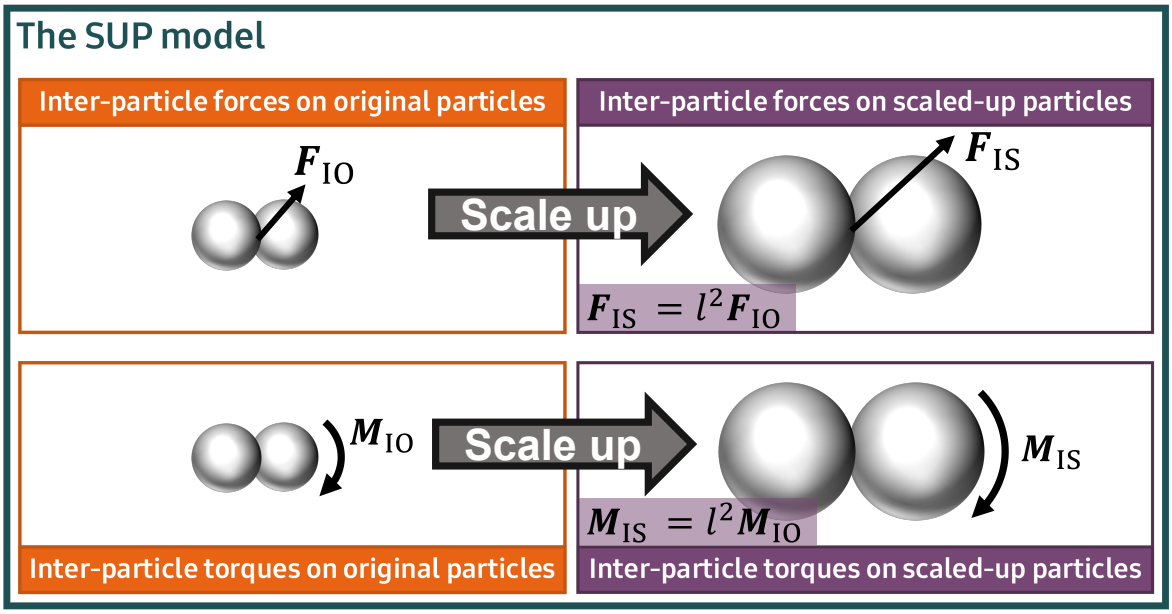

(a) The SUP model

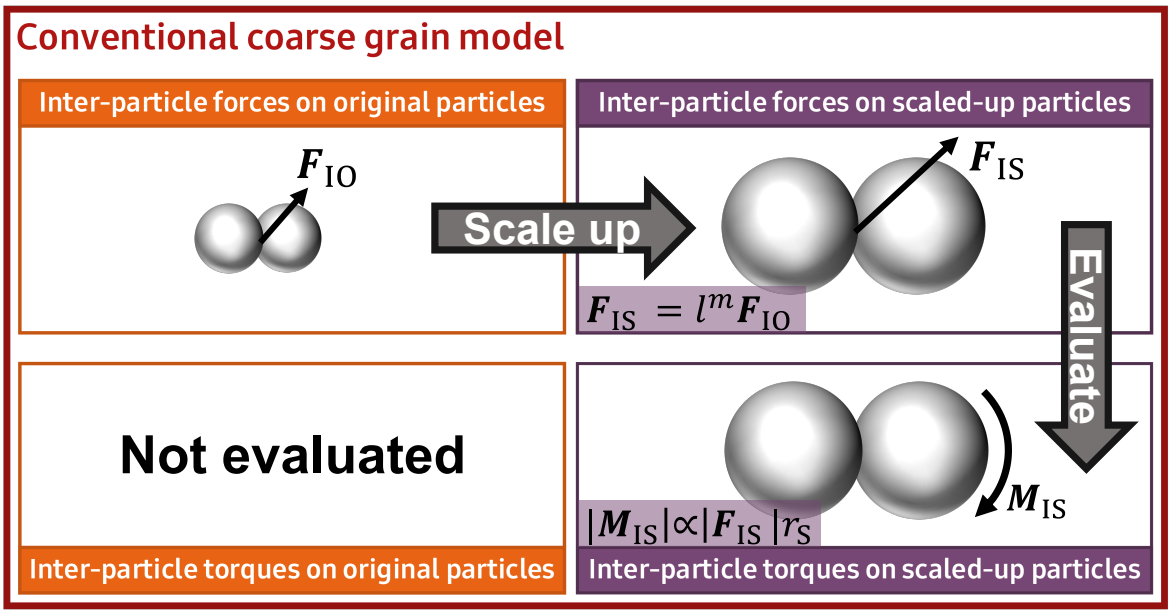

(b) Conventional coarse grain model

Figure 3.5: The different concepts of torques scaling between The SUP model and Conventional coarse grain model of DEM.

Rearranging Equation (3.47) gives:

$$m_{\mathrm{S}}^{*}\frac{dv_{r\mathrm{S}}}{dt} = -\frac{4}{3}E^{*}r_{\mathrm{S}}^{*1/2}\delta_{\mathrm{S}}^{3/2} \tag{3.48}$$

Equations (3.46) and (3.47) are written in the same form with different particle size. Typically, with the Hertzian theory, the time step is using the Rayleigh time as [129], that is proportional to the particle size:

$$\Delta t \sim \frac{\pi r}{0.8766 + 0.163\nu}\sqrt{\frac{2\rho(1+\nu)}{E}} \tag{3.49}$$

The relationship of original particle radius and scaled-up particle radius can be given by:

$$r_{\mathrm{S}} = l r_{\mathrm{O}} \tag{3.50}$$

Equations (3.49) and (3.50) suggest that the time step for the scaled-up particle can be l times larger than that of the original particle.

3.4 Closure

The present chapter offers a comprehensive introduction to the coarse grain model of DEM. The coarse grain model is one of the most promising approaches to reduce computational costs in DEM simulations. This is achieved by artificially increasing particle size, which effectively decreases the total number of particles within a given system. Coarse grain models can be classified into two types: parameter scaling and direct force scaling. These two methods are introduced in Sections 3.2.1 and 3.2.2, respectively.

To achieve kinematic similarity between the systems of original and of coarse grain particles, parameter scaling adjusts the physical properties and other parameters of DEM particles. Parameter scaling is simple in terms of implementation, because it does not require any additional coding. However, the scaling criterion for each parameter is de-

pendent on the force models employed. For complex forms of forces, determining this criterion can be challenging or even impossible.

The other approach to conduct coarse-grained DEM simulation is the direct force scaling, where the forces acting on original particles are first estimated using the original particle properties and variables, and then directly scaled to apply to scaled-up particles. This work focuses on direct force scaling because this approach holds more promise in establishing generic scaling laws that are applicable to different interactions.

The scaled-up particle (SUP) model is a novel model of direct force scaling, which is derived from the equivalence of bulk momentum change in arbitrary particle flow, which is introduced in Section 3.3.

In Section 3.3.1, three scaling laws of forces in the SUP model are derived based on the effectively homogeneous assumption of particles in control volume. Firstly, with regard to particle movement, e.g., the translational velocity of particles, no scaling is applied. For any inter-particle force, such as inter-particle contact force and attraction force, l^2-scaling is employed. In the present work, the liquid-bridge force and JKR surface adhesion force are employed to investigate the scaling of inter-particle attraction force. l^3-scaling is employed to scale the body force acting on the CV, in the present work, the only employed body force is gravity. The derivation of scaling laws of the SUP model is not depending on the specific type of force, which implies its applicability not limited in any specific type of force.

Section 3.3.2 introduced the evaluation of the original variables for direct force scaling. In scaled-up particle simulations employing direct force scaling, original particles are not explicitly utilised. Instead, they are represented by scaled-up particles. Therefore, it is crucial to accurately evaluate the original particle variables from those of the scaled-up particle to estimate the forces acting on the original particles. These variables encompass the particle translational velocity, angular velocity, particle overlap, and separation distance.

Section 3.3.3 compared the difference in torque scaling concepts between the SUP model and conventional coarse grain models of direct force scaling. In the SUP model, the torques on the original particles are first evaluated and then scaled so that the total changes of angular momentum in control volumes are the same, which is different from that of conventional models.

Section 3.3.4 introduced the scaling of the stable time step in coarse grained DEM simulation, which implies that the time step for the scaled-up particle can be l times larger than that of the original particle.

The present work validated the SUP model introduced in this section, and compared it to conventional coarse grain models of DEM. The evaluation of original variables, the scaling laws of inter-particle forces and the scaling of the stable time step are validated in Chapter 4. The evaluation of inter-particle torques is validated in Chapter 5. The applicability of the SUP model to particles with particle size distributions (PSDs) is validated in Chapter 6.

Chapter 4

Forces scaling for scaled-up particles

4.1 Introduction

In this chapter, several simulations were conducted to discuss the validity of the scale power index and the evaluation method of original particle variables explained in Section 3.3.1 and 3.3.2. For each system presented in this section, three different methods for scaled-up particles are tested, as summarised in Table 4.1.

Following Chan and Washino [173], different scale power indices are used for inter-particle and body forces. Method 1 employs $m = 2$ for both inter-particle forces and torques in conjunction with the geometric similarity to evaluate the particle overlap and separation distance, while $m = 3$ is used for body forces. This is the method suggested in the present work. Method 2 employs the same scale power indices as Method 1 but the original particle overlap and separation distance are assumed to be the same as those of the scaled-up particle (i.e. the conventional method). Method 3 employs $m = 3$ for both inter-particle and body forces (similar to Sakai and Koshizuka's model) as well as the corresponding torques with geometric similarity for the evaluation of the original variables.

Firstly, uniaxial compression simulations of packed particle beds were performed to investigate the particle system dominated by inter-particle contact forces. The detailed conditions and results discussion of uniaxial compression simulations can be found in

Table 4.1: Methods used in scaled-up particle simulations.

Method 1	Method 2	Method 3
$\boldsymbol{F}_{\mathrm{IS}} = l^2 \boldsymbol{F}_{\mathrm{IO}}$	$\boldsymbol{F}_{\mathrm{IS}} = l^2 \boldsymbol{F}_{\mathrm{IO}}$	$\boldsymbol{F}_{\mathrm{IS}} = l^3 \boldsymbol{F}_{\mathrm{IO}}$
$\boldsymbol{M}_{\mathrm{IS}} = l^2 \boldsymbol{M}_{\mathrm{IO}}$	$\boldsymbol{M}_{\mathrm{IS}} = l^2 \boldsymbol{M}_{\mathrm{IO}}$	$\boldsymbol{M}_{\mathrm{IS}} = l^3 \boldsymbol{M}_{\mathrm{IO}}$
$\boldsymbol{F}_{\mathrm{BS}} = l^3 \boldsymbol{F}_{\mathrm{BO}}$	$\boldsymbol{F}_{\mathrm{BS}} = l^3 \boldsymbol{F}_{\mathrm{BO}}$	$\boldsymbol{F}_{\mathrm{BS}} = l^3 \boldsymbol{F}_{\mathrm{BO}}$
$\delta_{\mathrm{O}} = \delta_{\mathrm{S}}/l$	$\delta_{\mathrm{O}} = \delta_{\mathrm{S}}$	$\delta_{\mathrm{O}} = \delta_{\mathrm{S}}/l$
$S_{\mathrm{O}} = S_{\mathrm{S}}/l$	$S_{\mathrm{O}} = S_{\mathrm{S}}$	$S_{\mathrm{O}} = S_{\mathrm{S}}/l$

Section 4.2.

Subsequently, simulations of particle flow in a vertical mixer were performed to investigate the particle system dominated by inter-particle attraction forces. The liquid bridge force and the JKR surface adhesion force are employed as instances of inter-particle attraction forces, which have been introduced in Section 2.3.2. The detailed conditions and results discussions of simulations can be found in Section 4.3.

In addition, the simulations of particles in a periodic box are conducted to investigate the scaling law of the time step. The scaling law of critical time step has been introduced in Section 2.4. The detailed conditions and results discussions of simulations can be found in Section 4.4.

4.2 Uniaxial compression of packed particle bed

The first validation test is uniaxial compression of packed particles as shown in Figure 4.1. The original particle properties used in the simulation are listed in Table 4.2. The original particle diameter is 0.5 mm and density is 2500 kg/m^3. Particles with diameters of 1 and 2 mm are employed as scaled-up particles, i.e. the scale factors of 2 and 4, respectively.

The initial particle beds are prepared using the following steps. Particles with small sliding friction ($\mu_s = 0.01$) are randomly generated and allowed to fall into the simulation domain with dimensions of $14 \times 14 \times 200$ mm^3 by gravity. A plane wall is placed at the bottom and periodic boundaries are used in the lateral directions. The low friction

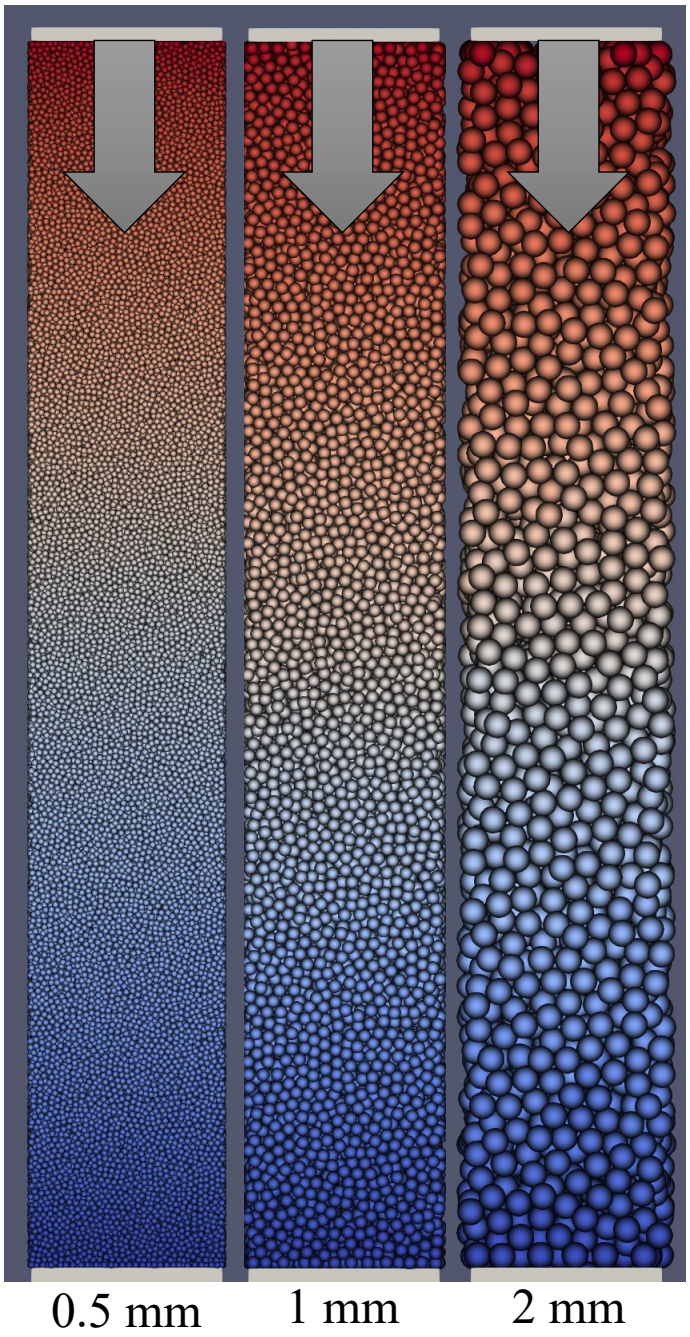

Figure 4.1: Uniaxial compression of packed particle bed using the proposed method. Periodic boundaries are used in the lateral directions. Colour indicates the particle velocity magnitude between 0 mm/s (blue) and 5 mm/s (red).

Table 4.2: Original particle properties for uniaxial compression of packed particle bed.

Property	Value
Particle diameter [mm]	0.5
Particle density [kg/m^3]	2500
Initial bed height [mm]	100
Young's modulus [MPa]	5
Poisson's ratio [-]	0.3
Restitution coefficient [-]	0.9
Sliding friction coefficient [-]	0.3

particles are used to make the initial particle beds compact. Then the particles above 100 mm from the bottom are removed and an upper wall is placed at the bed surface.

During the compression process, the sliding friction coefficient is reset to 0.3. The upper wall is moved downwards with a constant speed of 5 mm/s while the bottom wall is fixed in space. The bed is compressed until the upper wall moves 10 mm, i.e. strain of 0.1. The stress on the upper wall is monitored during the compression. No attraction force is considered and the contact force is calculated using the Hertzian theory. Although gravitational force is exerted on the particles, it only has a negligible impact on the stress obtained.

Figure 4.2 shows the stress-strain relationship obtained from the simulations. It can be seen in Figure 4.2(a) that the results of the original and scaled-up particles with Method 1 almost fall into the same curve. On the other hand, in Figure 4.2(b) and (c), the scaled-up particles significantly overestimate the compression stress, and this tendency is more pronounced as the scale factor increases. It is concluded from these simulations that the l^2 scaling with the geometric similarity for particle overlap is the most appropriate method for a contact force dominant system.

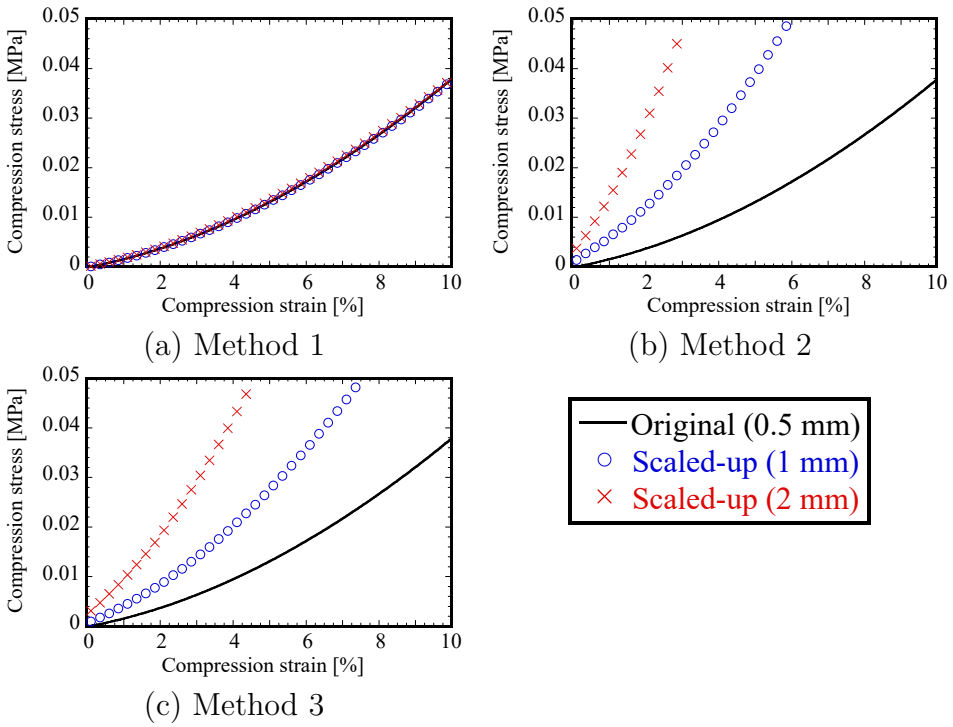

Figure 4.2: Stress-strain relationship during uniaxial compression of packed particle bed.

4.3 Particle flow in a vertical mixer

The second validation test is a dynamic system of particle flow in a vertical mixer where attraction forces are exerted on the particles. The mixer used is a scaled-down version of the 10L Roto Junior high shear granulator (Zanchetta Lucca). The inner diameter of the mixer is 84 mm and a 3-bladed impeller shown in Figure 4.3 is mounted at the bottom. The common properties of the original particles used in all cases are listed in Table 4.3. The original particle diameter is 0.5 mm, density is 1000 kg/m^3, and the total mass is 0.0458 kg as used by Chan and Washino [173]. The impeller rotates with 300 rpm until the flow reaches steady state. Particles with diameters of 1 and 2 mm are employed as scaled-up particles, i.e. scale factors of 2 and 4, respectively. Although it is possible to further increase the particle size, the mixer to particle diameter ratio, D/d, should not be too small in order to minimise boundary effects [211, 212]. The range of D/d in this study is from 42 to 168 which is in accordance with the recommendation of $D/d \geq 40$ in the literature [211, 212]. Simulations have been conducted to validate the limitation of D/d in the present work, which provides the same conclusion as the literature [211, 212]. The detailed results and discussions refer to Appendix.

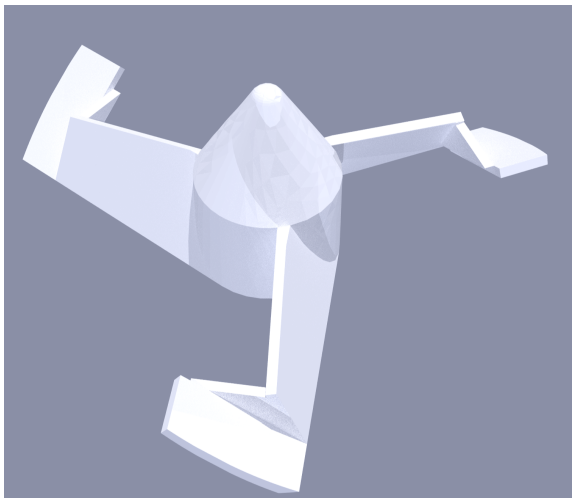

Figure 4.3: Snapshot of the impeller of vertical mixer.

Two sets of simulations are carried out and presented in Sections 4.3.1 and 4.3.2,

Table 4.3: Common properties of original particles for vertical mixer.

Property	Value
Particle diameter [mm]	0.5
Particle density [kg/m^3]	1000
Total mass [kg]	0.0458
Young's modulus [MPa]	100
Poisson's ratio [-]	0.3
Restitution coefficient [-]	0.1
Sliding friction coefficient [-]	0.3

respectively, with different combinations of contact and attraction force models. The first is the Hertzian contact with the capillary force model explained in Section 2.3.2.1, and the second is the JKR adhesive contact model explained in Section 2.3.2.2. The attraction forces between the particles and mixer walls are deactivated so that the particles do not adhere to the casing wall and impeller, which may reduce the amount of bulk moving particles available for velocity analyses.

4.3.1 Wet particles with capillary force

The particles are assumed to be uniformly wet with liquid. The liquid to solid volume ratio is 0.05 and does not change with time, which is denoted by a_1. 8.3% of the liquid on the particle surface is used for the formation of the bridge between each particle pair so that the entire liquid is used in the case of maximum packing, which is denoted as b_1. Based on previous work [173], the liquid bridge volume for the original particle is evaluated as:

$$\lambda_{\mathrm{LO}} = \lambda_{\mathrm{LS}}/l^3 \tag{4.1}$$

where the liquid bridge volume is calculated as:

$$\lambda_{\mathrm{LS}} = a_1 b_1 (V_{\mathrm{pSi}} + V_{\mathrm{pSj}}) \tag{4.2}$$

where V_p is the particle volume. The rupture distance for the original particle, S_rupO, is calculated using λ_LO, and if the separation distance, $S_\mathrm{O} = S_\mathrm{S}/l$, is larger than S_rupO, the liquid bridge force is not calculated. Four different values of surface tension coefficient are tested, i.e. 0.05, 0.1, 0.2 and 0.4 N/m. The contact angle is set to 0 deg and viscous force is not taken into account. The minimum separation distance for the original particle is set to 1 μm. If S_O is smaller than 1 μm, the minimum separation distance is used to calculate the liquid bridge force.

Figure 4.4 shows snapshots of the original particle flow with different values of surface tension. It is a typical flow of cohesive particles that particles are bonded together and form lumps. The size of the lumps increases as the surface tension increases. Especially with $\gamma_\mathrm{L} = 0.4$ N/m, the entire particles are lumped together. The overall particle velocity increases as the surface tension increases. This is because the relative velocity of the large lumps to the impeller is smaller than that of the small lumps.

Figures 4.5 and 4.6 show snapshots of the scaled-up particle flow using Method 1 with scale factors of 2 and 4, respectively. Although the boundaries of the lumps become less clear as the scale factor increases (especially with $\gamma_\mathrm{L} = 0.1$ and 0.2 N/m), the overall flow structure and velocity field of the original particles are well captured. Figures 4.7 and 4.8 show snapshots of the scaled-up particles using Method 2 with scale factors of 2 and 4, respectively. The overall flow structure is similar to that of the original particles to a certain extent. However, the boundaries of the lumps are even less clear compared to Method 1. In addition, comparing with Figure 4.4, the powder velocity in Figures 4.7 and 4.8 is smaller. It indicates that Method 2 cannot provide sufficiently large capillary force. Figures 4.9 and 4.10 show particle snapshots using Method 3 with scale factors of 2 and 4, respectively. It can be clearly seen that the particles become more cohesive than the original particles, which indicates that Method 3 largely overestimates the capillary force.

Figures 4.11, 4.12 and 4.13 show the probability density distribution of the particle

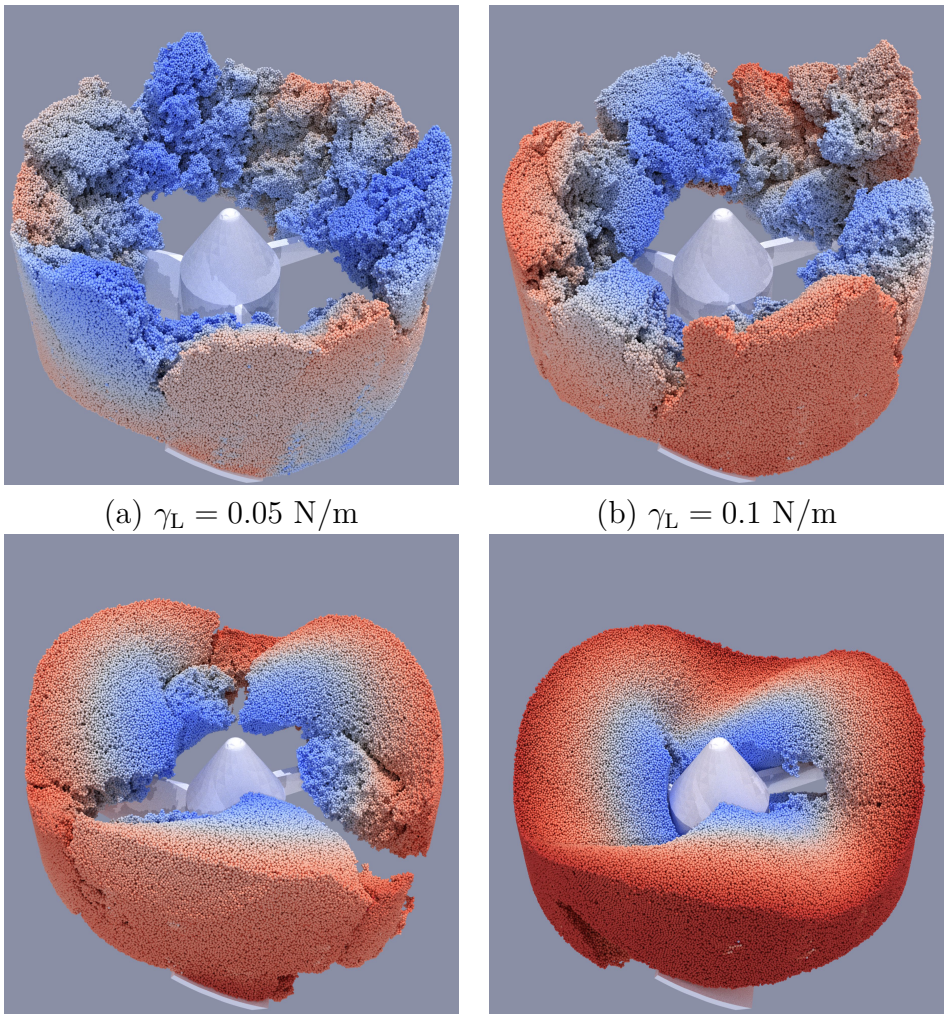

(a) $\gamma_L = 0.05$ N/m (b) $\gamma_L = 0.1$ N/m

(c) $\gamma_L = 0.2$ N/m (d) $\gamma_L = 0.4$ N/m

Figure 4.4: Snapshots of the original particles in vertical mixer with capillary force. Colour indicates the particle velocity magnitude between 0 m/s (blue) and 1.4 m/s (red).

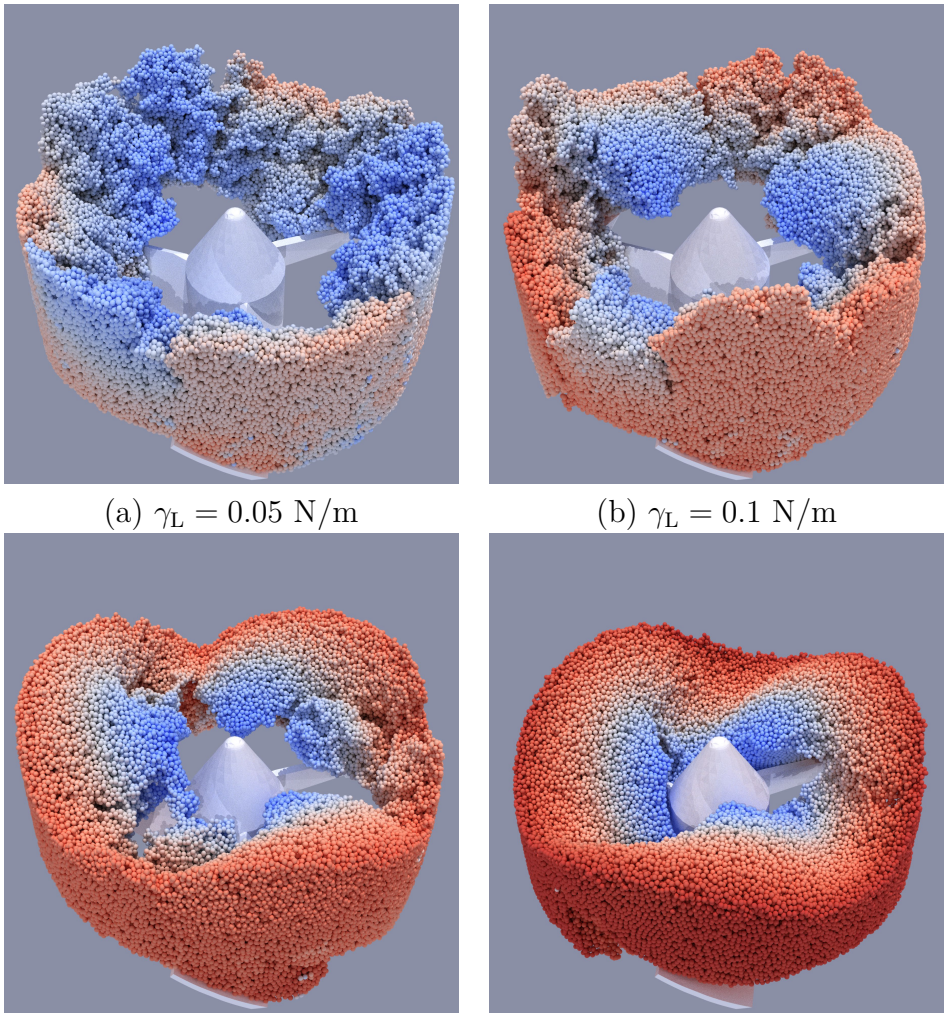

(a) $\gamma_L = 0.05$ N/m (b) $\gamma_L = 0.1$ N/m

(c) $\gamma_L = 0.2$ N/m (d) $\gamma_L = 0.4$ N/m

Figure 4.5: Snapshots of the scaled-up particles in vertical mixer with capillary force (scale factor = 2, Method 1). Colour indicates the particle velocity magnitude between 0 m/s (blue) and 1.4 m/s (red).

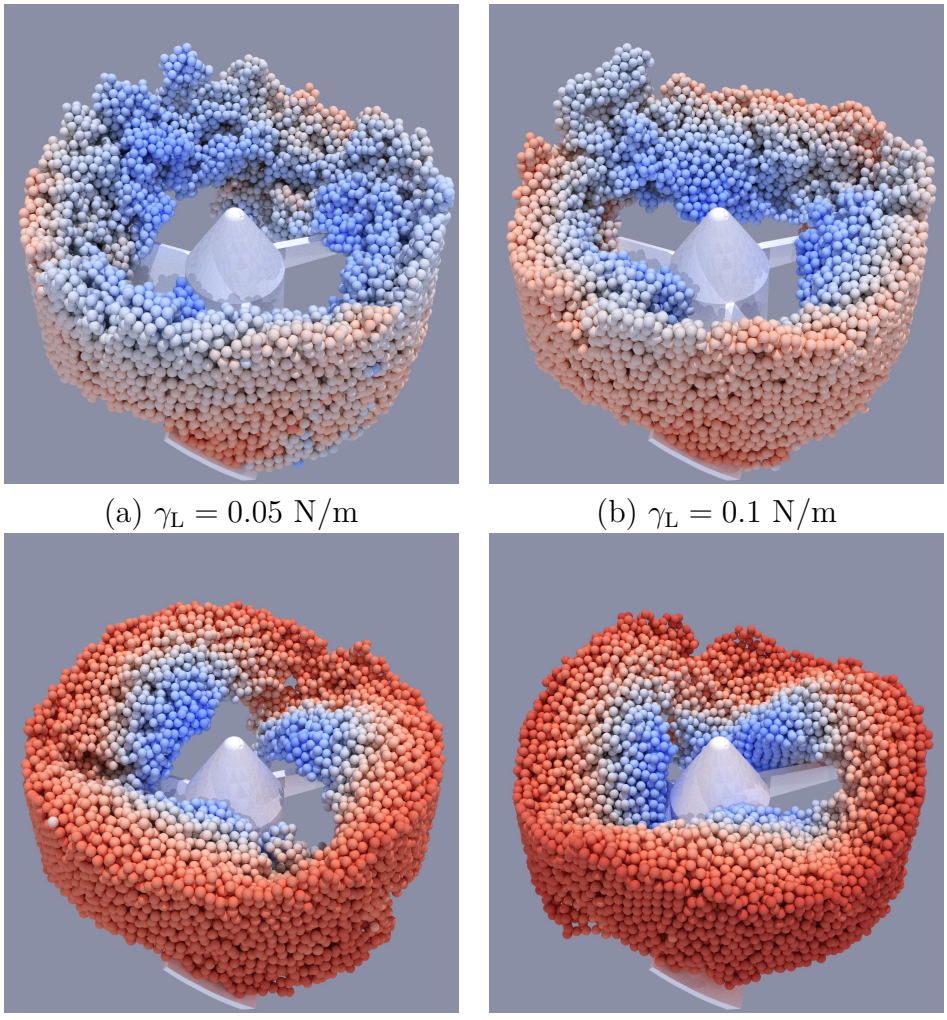

(a) $\gamma_L = 0.05$ N/m (b) $\gamma_L = 0.1$ N/m

(c) $\gamma_L = 0.2$ N/m (d) $\gamma_L = 0.4$ N/m

Figure 4.6: Snapshots of the scaled-up particles in vertical mixer with capillary force (scale factor = 4, Method 1). Colour indicates the particle velocity magnitude between 0 m/s (blue) and 1.4 m/s (red).

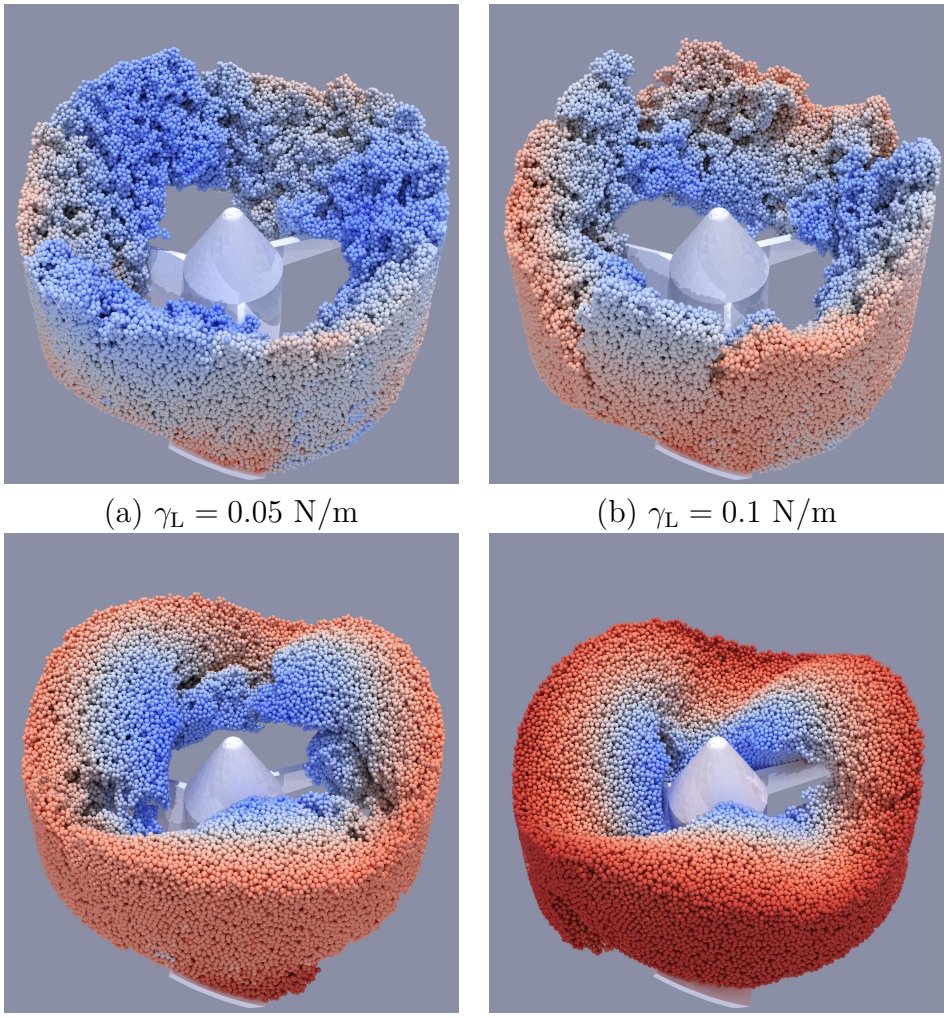

(a) $\gamma_L = 0.05$ N/m (b) $\gamma_L = 0.1$ N/m

(c) $\gamma_L = 0.2$ N/m (d) $\gamma_L = 0.4$ N/m

Figure 4.7: Snapshots of the scaled-up particles in vertical mixer with capillary force (scale factor = 2, Method 2). Colour indicates the particle velocity magnitude between 0 m/s (blue) and 1.4 m/s (red).

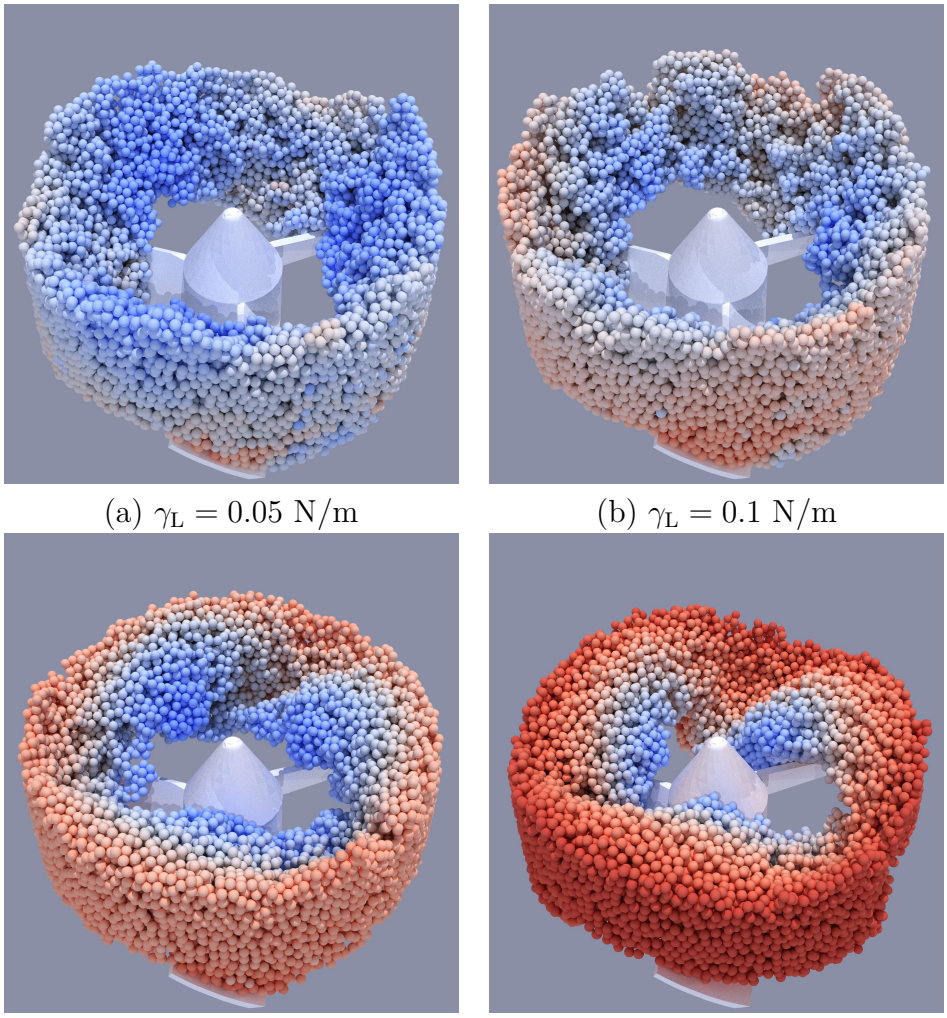

(a) $\gamma_L = 0.05$ N/m (b) $\gamma_L = 0.1$ N/m

(c) $\gamma_L = 0.2$ N/m (d) $\gamma_L = 0.4$ N/m

Figure 4.8: Snapshots of the scaled-up particles in vertical mixer with capillary force (scale factor = 4, Method 2). Colour indicates the particle velocity magnitude between 0 m/s (blue) and 1.4 m/s (red).

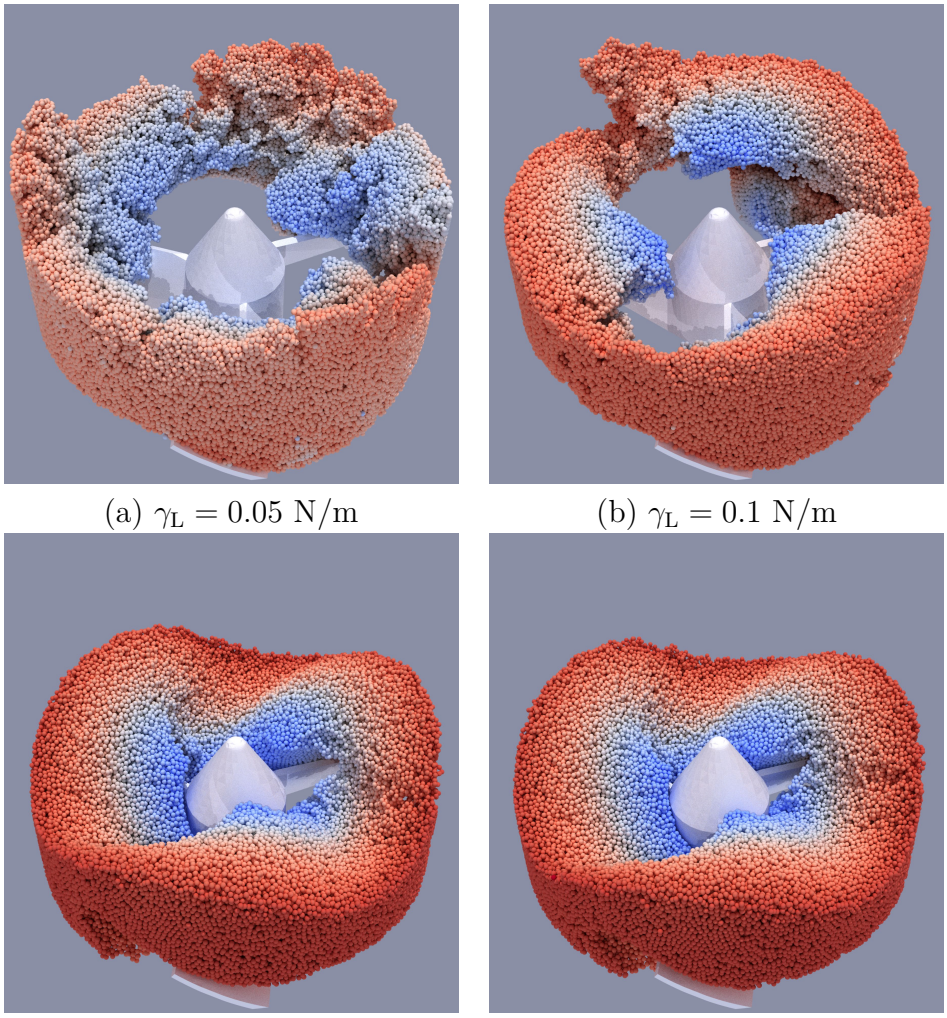

(a) $\gamma_L = 0.05$ N/m (b) $\gamma_L = 0.1$ N/m

(c) $\gamma_L = 0.2$ N/m (d) $\gamma_L = 0.4$ N/m

Figure 4.9: Snapshots of the scaled-up particles in vertical mixer with capillary force (scale factor = 2, Method 3). Colour indicates the particle velocity magnitude between 0 m/s (blue) and 1.4 m/s (red).

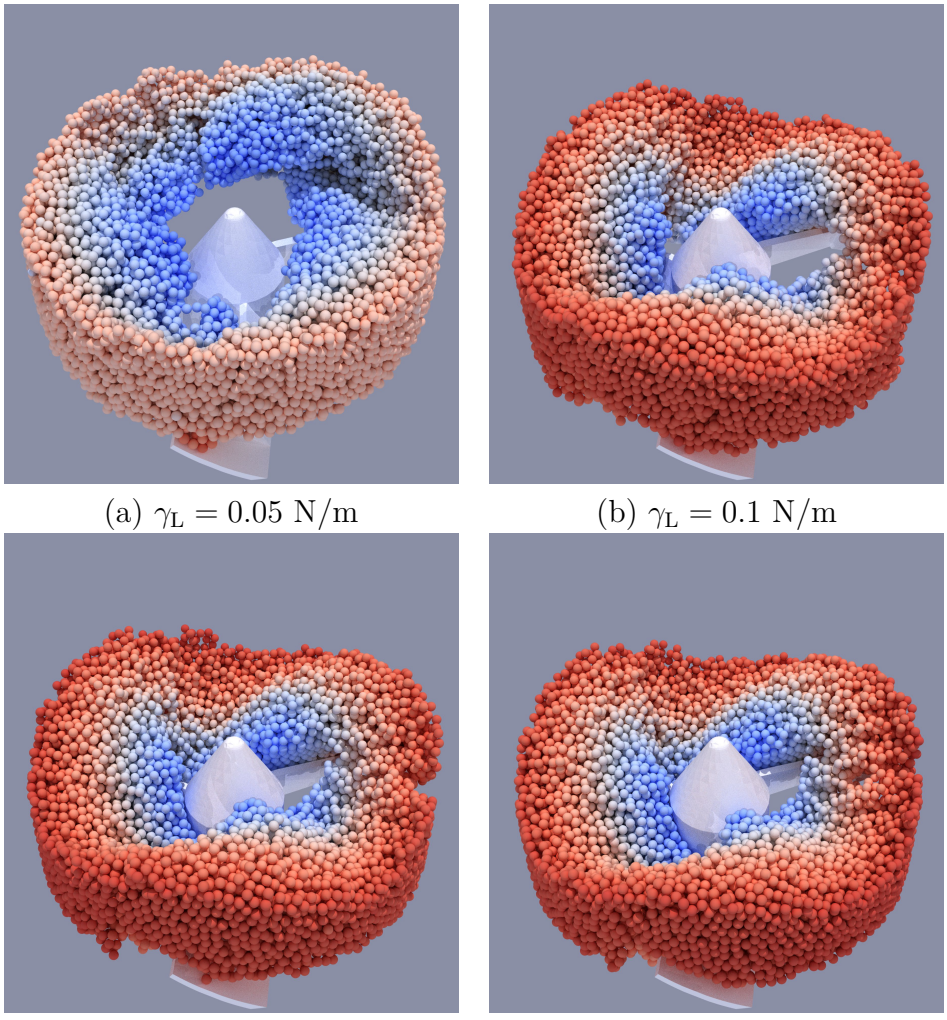

(a) $\gamma_L = 0.05$ N/m (b) $\gamma_L = 0.1$ N/m

(c) $\gamma_L = 0.2$ N/m (d) $\gamma_L = 0.4$ N/m

Figure 4.10: Snapshots of the scaled-up particles in vertical mixer with capillary force (scale factor = 4, Method 3). Colour indicates the particle velocity magnitude between 0 m/s (blue) and 1.4 m/s (red).

velocity magnitude at steady state with Methods 1, 2 and 3, respectively. The distribution without attraction force (i.e. $\gamma_L = 0$ N/m) is also included to indicate that the capillary force has a large impact on the particle velocity even with the smallest surface tension coefficient tested. First, the discussion focuses on how different surface tension values influence the results of the original particles. When $\gamma_L = 0.05$ N/m, the distribution of the original particle velocity is narrow with a large peak value at around 0.75 m/s. The distribution becomes broader as the surface tension coefficient increases while the peak velocity is shifted rightward. When $\gamma_L = 0.4$ N/m, the probability increases linearly with the particle velocity, which indicates that almost the entire particles move together with the impeller since a large lump is formed as can be seen in Figure 4.4(d).

The focus now shifts to the comparison of simulation results between the original and scaled-up particles. In Figure 4.11, it can be seen that the scaled-up particles can reasonably reproduce the original particle velocity distribution. However, a slight discrepancy is observed when $\gamma_L = 0.1$ and 0.2 N/m due to the formation of the medium size lumps of the original particles, which cannot be "resolved" with the large scaled-up particles. In Figure 4.12, the peak velocities of the scaled-up particles are shifted leftwards from those of the original particles. This is because the capillary force is underestimated with the conventional evaluation of the separation distance. Finally, in Figure 4.13, the results obtained from the scaled-up particles are significantly different from the original particle results and the peak velocities are shifted rightwards. This is because the capillary force is largely overestimated with the l^3 scaling. In Figure 4.13(d), one may find the velocity distributions similar between the original and scaled-up systems. However, this is simply because all the particles form a single lump due to the strong capillary force above which the velocity distribution does not change any more. Note that the results of the scaled-up particles in Figure 4.13(c) and (d) are almost the same. It is concluded from these simulations that the l^2 scaling with geometric similarity is the most appropriate method to replicate the original particle behaviour in a capillary force dominant system.

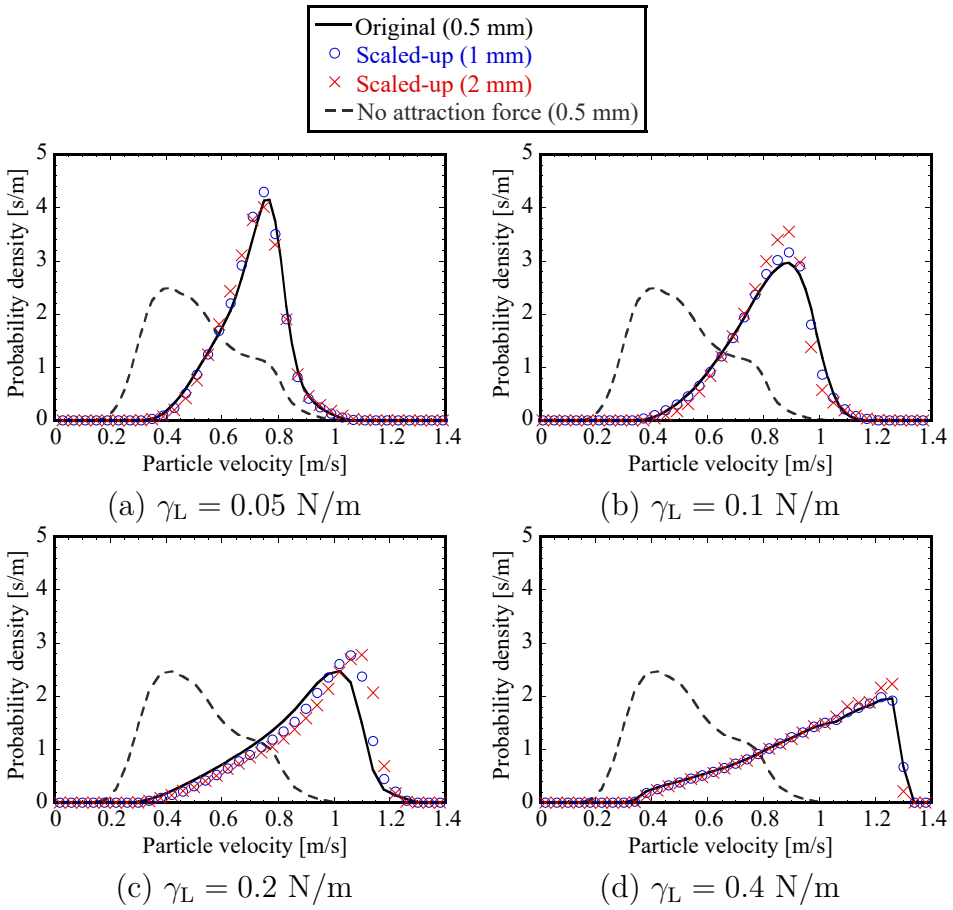

Figure 4.11: Probability density distribution of particle velocity magnitude in vertical mixer with capillary force (Method 1).

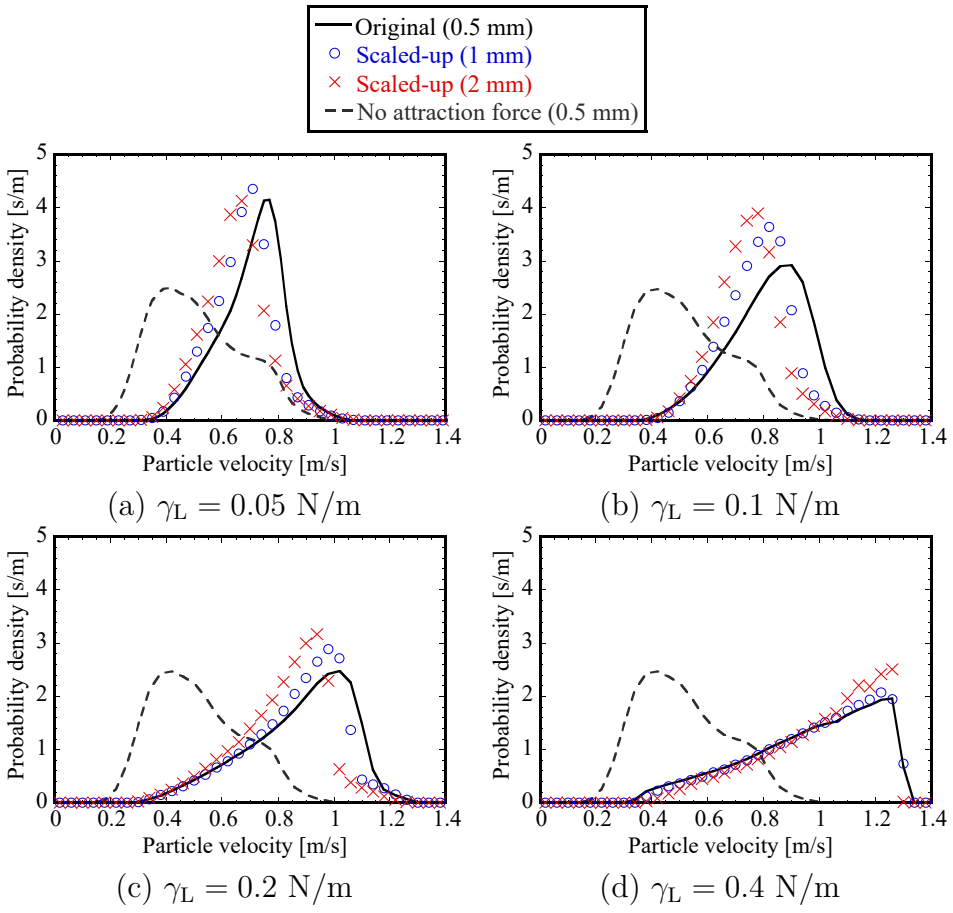

Figure 4.12: Probability density distribution of particle velocity magnitude in vertical mixer with capillary force (Method 2).

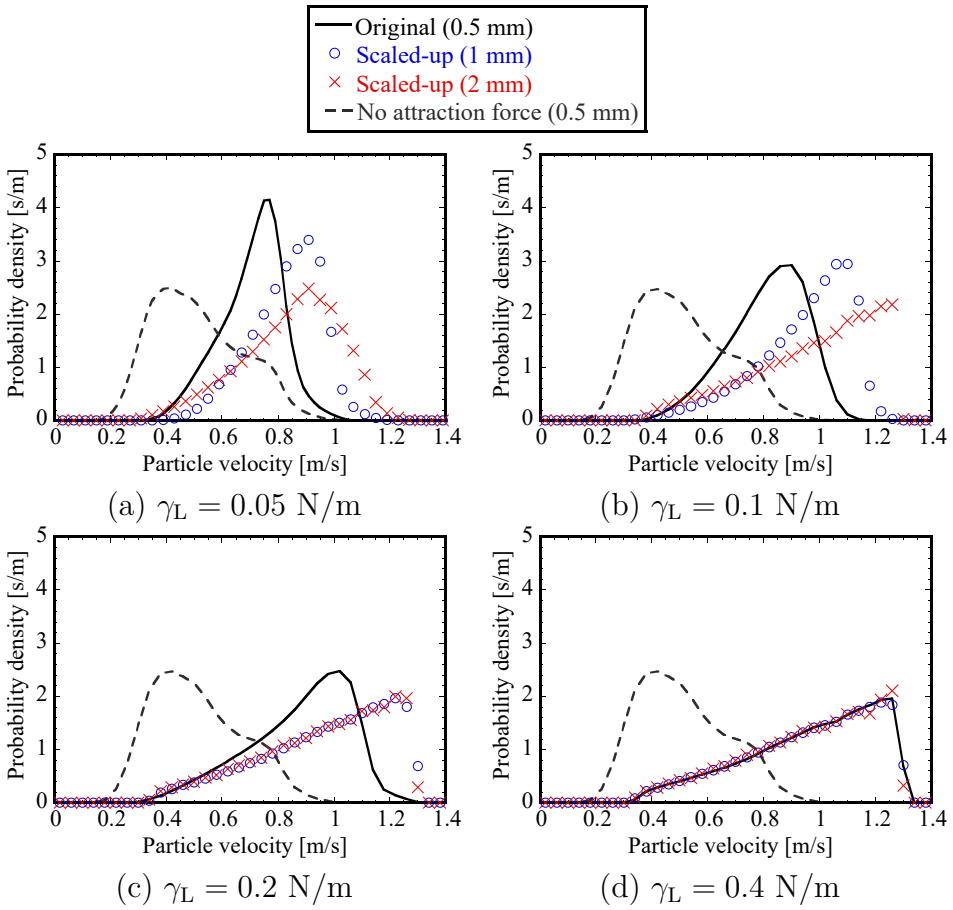

(a) $\gamma_L = 0.05$ N/m (b) $\gamma_L = 0.1$ N/m

(c) $\gamma_L = 0.2$ N/m (d) $\gamma_L = 0.4$ N/m

Figure 4.13: Probability density distribution of particle velocity magnitude in vertical mixer with capillary force (Method 3).

In the present work, the liquid volume on a particle is defined by the volume ratio of liquid to solid, so solid volume is exactly the particle volume, and the volume ratio directly controls the liquid volume on the particle. Consequently, the liquid volume of particles directly influences the liquid volume of liquid bridge λ_{L}, which controls the liquid bridge force.

Equation (2.43) reveals that the magnitude of the liquid bridge force is governed by λ_{L}. The magnitude of the liquid bridge force decreases as the volume of the liquid decreases. Equation (2.44) indicates that λ_{L} controls the rupture distance of liquid bridge. As the liquid volume decreases, the rupture distance of the liquid bridge also reduces, thereby increasing the likelihood of its rupture.

For validating the influence of liquid volume variation, simulations were conducted using the proposed model with $\gamma_{\mathrm{L}} = 0.05$ N/m and liquid to solid volume ratio being 0.005, which is 1/10 of the chosen value (0.05) of other wet particle flow simulations. Other conditions are exactly the same as other wet particle simulations. Figure 4.14 shows the results of original particles and scaled-up particles with $l = 4$. It is clear that the probability distribution is sensitive to the liquid volume variation, and the distribution shifted leftward with decreasing liquid volume, i.e., the average velocity of particles are decreased since the decrease of λ_{L}. The proposed model can capture this deviation and provide good agreements between original and scaled-up results with different volumes of liquid.

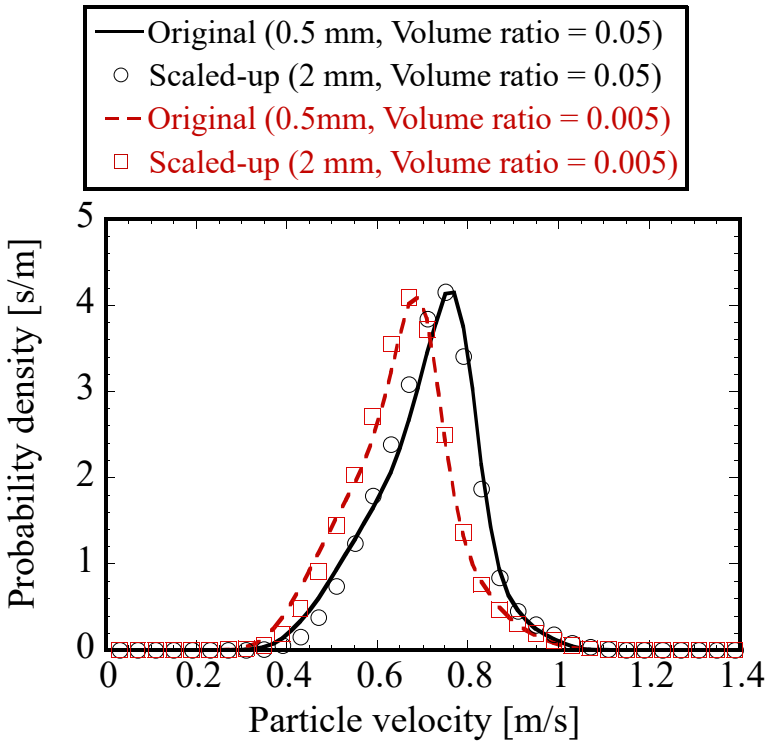

Figure 4.14: Probability density distribution of particle velocity magnitude in vertical mixer with capillary force using different volume ratios of liquid to solid. (Method 1, $\gamma_{\mathrm{L}} = 0.05$ N/m).

4.3.2 Particles with JKR surface adhesion force

It is considered that the surface adhesion force calculated from the simplified JKR model is exerted on the particles. Four different values of surface energy are tested, i.e. 0.1, 0.2, 0.4 and 0.8 J/m^2. Since the original particle size is relatively large (0.5 mm), artificially large surface energy values are used so that noticeable impacts on the particle velocity can be seen. Note that the purpose of these tests is to discuss the validity of the SUP model.

Figures 4.15, 4.16 and 4.17 show the probability density distribution of the particle velocity magnitude at steady state with Methods 1, 2 and 3, respectively. Similar to the capillary force cases discussed in the discussions of wet particle simulations, it can be seen that Method 1 provides the best prediction of the original particle velocity whilst Methods 2 and 3 give much larger differences. This proves that the l^2 scaling with the geometric similarity for particle overlap is valid for a system where surface adhesion force is dominant. The results presented in Sections 4.2 and 4.3 implies that the proposed method is versatile and universally applicable for any type of inter-particle force.

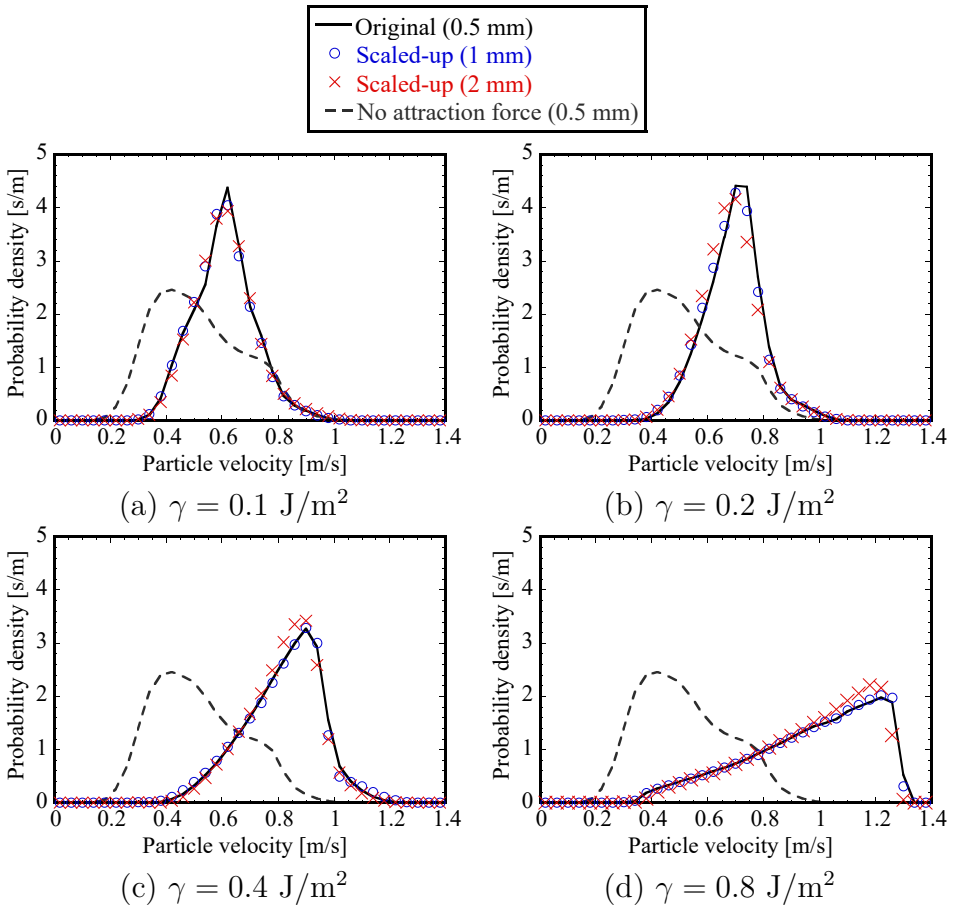

Figure 4.15: Probability density distribution of particle velocity magnitude in vertical mixer with JKR surface adhesion force (Method 1).

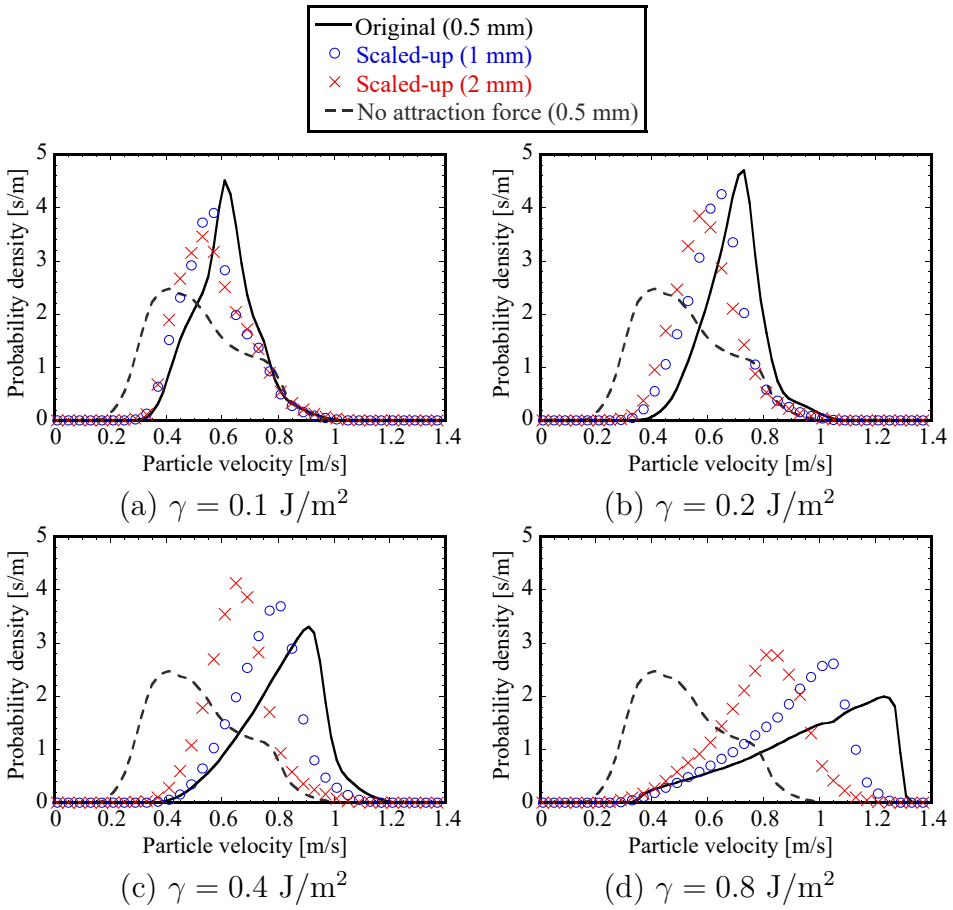

Figure 4.16: Probability density distribution of particle velocity magnitude in vertical mixer with JKR surface adhesion force (Method 2).

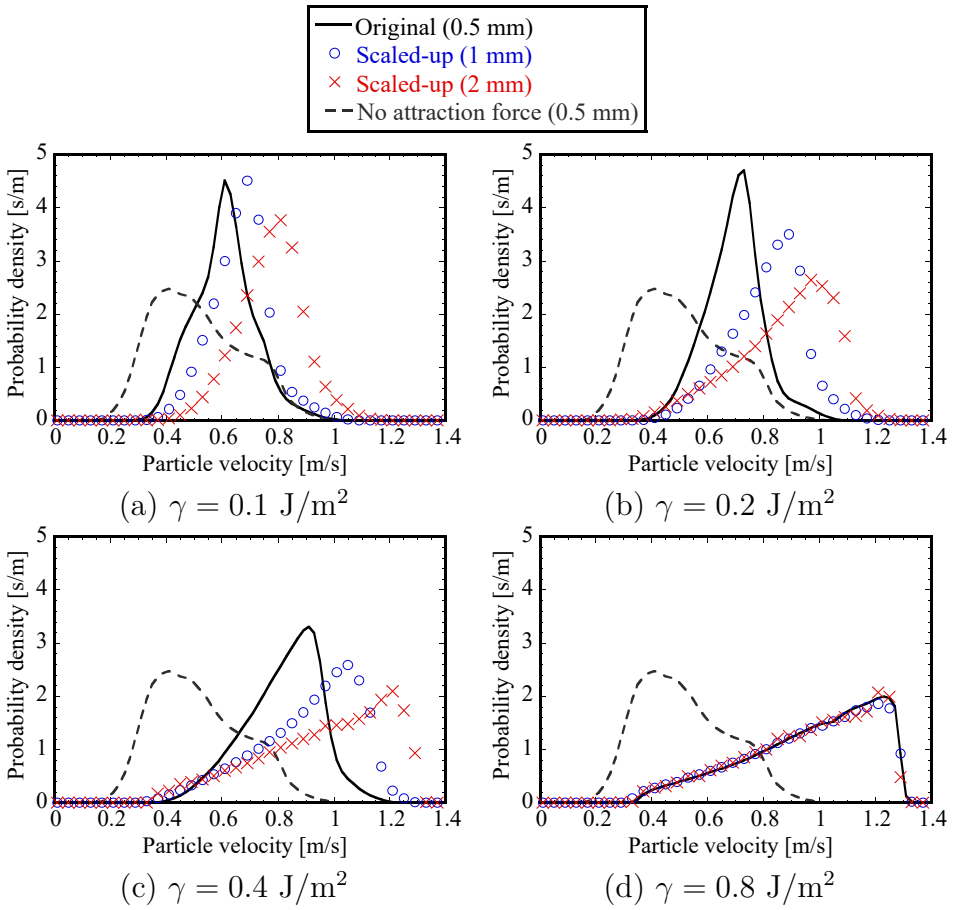

Figure 4.17: Probability density distribution of particle velocity magnitude in vertical mixer with JKR surface adhesion force (Method 3).

4.4 Periodic boundary box with no energy dissipation

Periodic boundary box simulations were conducted to verify the scaling of time step, which is presented in Section 3.3.4. The properties of original particles are shown in Table 4.4, where particles are set with no dissipation of energy when they collide with each other. In original simulations, the particle diameter is 0.5mm, and the box size is $20 \times 20 \times 20$ mm^3. The particles of 1 and 2 mm diameter are employed as scaled-up particles, while the box size is scaled-up as well. Between original and scaled-up systems, the total amounts of particles, the initial particle velocities and relative positions are artificially set at the same. When Δt is small enough and simulations run stable, it is expected that the total energy of particles fluctuates around a fixed value. Gradually increasing the Δt and it over a critical value, the collisions will not be resolved properly, and total energy will increase unphysically. Figure 4.18 shows the total kinetic energy change of original particle simulation with Δt equals to 0.2, 0.5, 0.8 and 1 μs. When Δt is 0.2 or 0.5 μs, simulations run stably. The total kinetic energy increased unphysically when $\Delta t = 0.8$ or 1 μs, which indicates 0.8 μs is larger than critical Δt. To find out the critical Δt for particles with different scale factors, a series of Δt are employed for original particles, from 0.2 μs to 1.8 μs with an interval of 0.1 μs. Figure 4.19 is obtained by the slope of plots in Figure 4.18, which shows the plots of energy increase rate with scale factors equal 1, 2 and 4. When the energy increase rate fluctuates around zero, the simulation is stable. For $l = 1$, 2 and 4, the critical Δt is approximately 0.6 μs, 1.2 μs and 2.4 μs respectively. These three Δt are proportional to the scale factor, which supports the proposed scaling rule of time step.

Table 4.4: Original particle properties of periodic boundary box simulation.

Property	Value
Particle diameter [mm]	0.5
Particle density [kg/m^3]	1000
Particles amounts [-]	36644
Young's modulus [MPa]	100
Poisson's ratio [-]	0.3
Restitution coefficient [-]	1
Sliding friction coefficient [-]	0

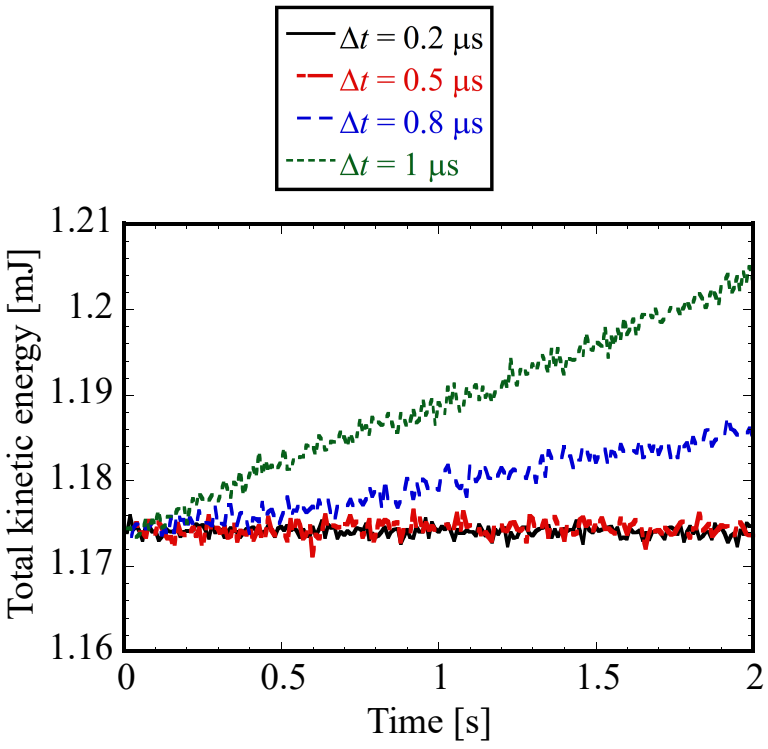

Figure 4.18: The total kinetic energy of periodic boundary box simulation (original particles).

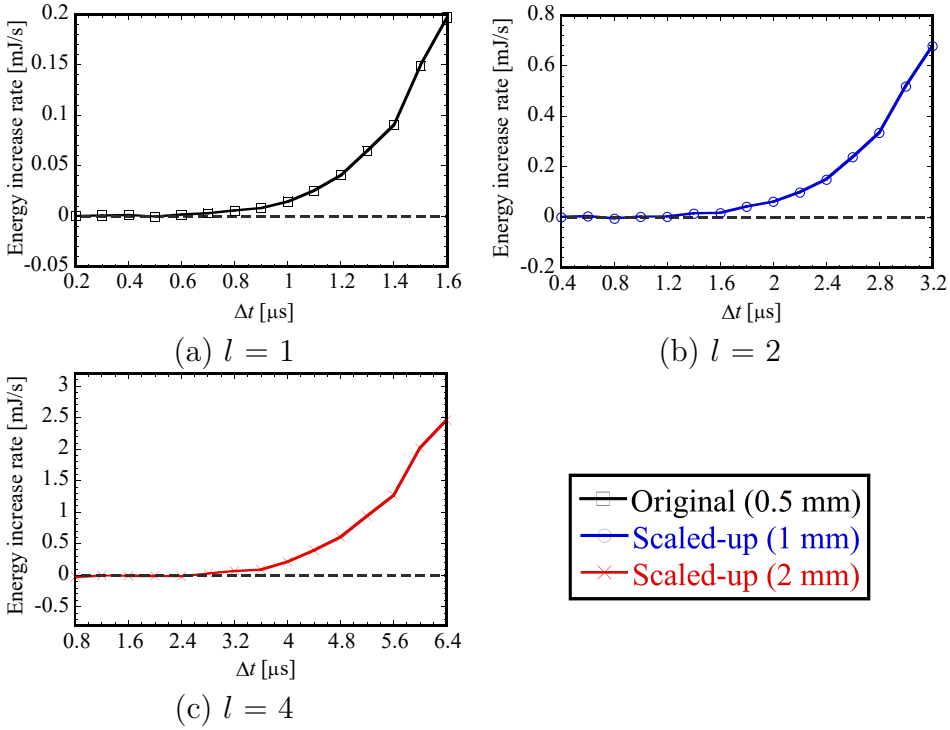

Figure 4.19: The total kinetic energy increase rate of periodic boundary box simulations.

4.5 Closure

In this chapter, several factors are compared and discussed that are related to the evaluation of inter-particle forces in coarse-grained DEM simulation. The SUP model is validated for inter-particle force scaling, and the scaling law of time step is also validated. The accurate evaluation of inter-particle forces for the scaled-up particles requires two essential factors:

- It is crucial to establish appropriate scaling laws for inter-particle forces, which have been introduced in Section 3.3.1 of Chapter 3, and validated in this chapter.
- In order to properly evaluate inter-particle forces, the direct force scaling method requires accurate estimation of the original particle variables, particularly the overlap and separation distance between original particles, which have been introduced in Section 3.3.2, and validated in this chapter.

The evaluation of inter-particle contact forces is validated in Section 4.2 through the simulations of particle bed compression, where inter-particle attraction forces are excluded. Three methods are employed and compared, the results are summarised as follows:

- Method 1: By employing the l^2-scaling, i.e. $\boldsymbol{F}_{\mathrm{IS}} = l^2 \boldsymbol{F}_{\mathrm{IO}}$, approach for inter-particle forces and employing the concept of geometric similarity, i.e. $\delta_{\mathrm{O}} = \delta_{\mathrm{S}}/l$, to evaluate original particle variables, the simulation results demonstrate a good agreement between scaled-up particles and their corresponding original particle simulation results. The scaled-up particle simulation can provide an almost identical stress-strain curve with that of the original system.
- Method 2: The compression stress is overestimated when employing the l^2-scaling for inter-particle forces, but applying the conventional method, i.e. $\delta_{\mathrm{O}} = \delta_{\mathrm{S}}$, to evaluate original particle variables.

- Method 3: The compression stress is overestimated when employing the l^3-scaling for inter-particle forces and the geometric similarity concept to evaluate original particle variables.

The evaluation of inter-particle attraction forces is validated in Section 4.3 through the simulations of particle flow in vertical mixer, where liquid bridge force and the JKR surface adhesion force are employed as the instances of attraction forces. Three methods are employed and compared, the results are summarised as follows:

- Method 1: By employing the l^2-scaling approach for inter-particle forces and employing the concept of geometric similarity (i.e. $S_{\mathrm{O}} = S_{\mathrm{S}}/l$) to evaluate original particle variables, the scaled-up particle simulation can reasonably reproduce the overall flow structure and velocity distributions of the original particles in a dynamic system. Slight discrepancies are observed when the attraction forces are relatively large, which may be because of the formation of medium size lumps which cannot be resolved with large scaled-up particles.

- Method 2: The particle average velocity is underestimated when employing the l^2-scaling for inter-particle forces, but applying the conventional method, i.e. $S_{\mathrm{O}} = S_{\mathrm{S}}$, to evaluate original particle variables.

- Method 3: The particle average velocity is overestimated when employing the l^3-scaling for inter-particle forces and the geometric similarity concept to evaluate original particle variables.

The scaling law of the critical time step for the SUP model introduced in Section 2.4 is further validated through the simulation of particles in a periodic boundary box with no energy dissipation, as discussed in Section 4.4. The results suggest that the time step for the scaled-up particle can be l times larger than that of the original particle.

The results indicate that both the concept of geometric similarity in evaluating original particle variables and the l^2-scaling for inter-particle forces are necessary to evaluate inter-

particle forces on the scaled-up particles. The SUP model, i.e. Method 1, theoretically can be applied to any type of inter-particle force, which is partially validated by the simulation results in this chapter.

Chapter 5

Torques scaling for scaled-up particles

5.1 Introduction

In this chapter, a series of simulations were conducted to investigate the validity of scaling laws for inter-particle torques as explained in Section 3.3.3. The torques arising from rolling resistance have been incorporated into the simulations presented in this chapter, which were not considered in Chapter 4. In the SUP model, the rolling resistance torque follows the same scaling law as the inter-particle contact torque, which is validated in the present chapter as well. Three different combinations of scaling laws, as presented in Table 5.1, are employed.

Table 5.1: Methods used in validation simulations.

Method 1	Method 2	Method 3
$\boldsymbol{F}_{\mathrm{IS}} = l^2 \boldsymbol{F}_{\mathrm{IO}}$	$\boldsymbol{F}_{\mathrm{IS}} = l^2 \boldsymbol{F}_{\mathrm{IO}}$	$\boldsymbol{F}_{\mathrm{IS}} = l^3 \boldsymbol{F}_{\mathrm{IO}}$
$\boldsymbol{M}_{\mathrm{IS}} = l^2 \boldsymbol{M}_{\mathrm{IO}}$	$\boldsymbol{M}_{\mathrm{IS}} = l^3 \boldsymbol{M}_{\mathrm{IO}}$	$\boldsymbol{M}_{\mathrm{IS}} = l^3 \boldsymbol{M}_{\mathrm{IO}}$
$\boldsymbol{F}_{\mathrm{BS}} = l^3 \boldsymbol{F}_{\mathrm{BO}}$	$\boldsymbol{F}_{\mathrm{BS}} = l^3 \boldsymbol{F}_{\mathrm{BO}}$	$\boldsymbol{F}_{\mathrm{BS}} = l^3 \boldsymbol{F}_{\mathrm{BO}}$

In all three employed methods, l^3-scaling is used for the body force, i.e. gravitational force, since it has been derived in Chapter 3 for the SUP model (Method 1). Furthermore, different scaling laws of the body force will significantly influence the bulk density of particle beds, shifting the focus of comparison to the body force scaling. Considering

that almost all coarse grain models of DEM in literature utilise l^3-scaling for body force [165, 166, 169, 173, 176], it would not be meaningful to employ a hypothetical body force scaling law for validation purposes. Method 1 uses l^2 for both inter-particle forces and torques. These are the scaling laws derived from the SUP model. In Method 2, l^2 is used for inter-particle forces but l^3 for inter-particle torques, which coincides with the work by Chu et al. [169]. As mentioned in Section 3.3.3, Methods 1 and 2 are derived from the two different concepts illustrated in Figure 3.1 (bottom and top, respectively). Method 3 uses l^3 for both inter-particle forces and torques for reference.

Two types of particle systems are employed to compare the scaling laws of inter-particle torques:

- Bulk density is an important macroscopic property of powders and often measured to assess flowability and compactability. In Section 5.2, the bulk density of cohesive particles beds is evaluated to investigate the influence of different scaling methods on the bulk density of scaled-up particle beds.

- Angle of repose is another major macroscopic property commonly used to evaluate powder flowability. In Section 5.3, heap formation of cohesive particles is simulated to investigate the applicability of the coarse grain model to measure the angle of repose.

5.2 Bulk density evaluation of particle bed

The first simulation is a static particle bed of cohesive mono-dispersed particles. The original particle is 0.5 mm in diameter with a density of 1000 kg/m^3, and other particle properties used are listed in Table 5.2. The coefficient of rolling resistance, μ_{r}, is varied from 0 to 0.8 for the EPSD model and from 0 to 0.16 for the CDT model. Particles with diameters of 1 and 2 mm are employed as scaled-up particles, i.e. the scale factors are 2 and 4, respectively.

Table 5.2: Particle properties for bulk density evaluation.

Property	Value
Particle density [kg/m^3]	1000
Young's modulus [MPa]	10
Poisson's ratio [-]	0.3
Restitution coefficient [-]	0.1
Sliding friction coefficient [-]	0.3
Surface energy [J/m^2]	0.2

Particles are randomly generated in an insertion region with dimensions of $20 \times 20 \times 90$ mm^3 whose centre is located at 285 mm from the bottom. The size of the simulation domain in the horizontal directions is 21×21 mm^2, where the periodic boundary condition is applied. A plane wall is positioned at the bottom. The particles are inserted with a mass flow rate of 1.68 g/s and initial velocity of $(0, 0, -0.2)$ m/s for 10 seconds. The particles are settled under the influence of gravity, and the bulk density is measured after relaxation. The particles below 20 mm and above 60 mm from the bottom are excluded in the bulk density measurement to eliminate the effect of the bottom wall and bed surface.

The results obtained from the simulation using the EPSD model are first discussed. Snapshots of the original particle beds with different coefficients of rolling resistance are shown in Figure 5.1. It can be observed that the height of the particle bed increases and the coordination number decreases as μ_{r} increases. This indicates that the rolling resistance impedes the formation of packed structures.

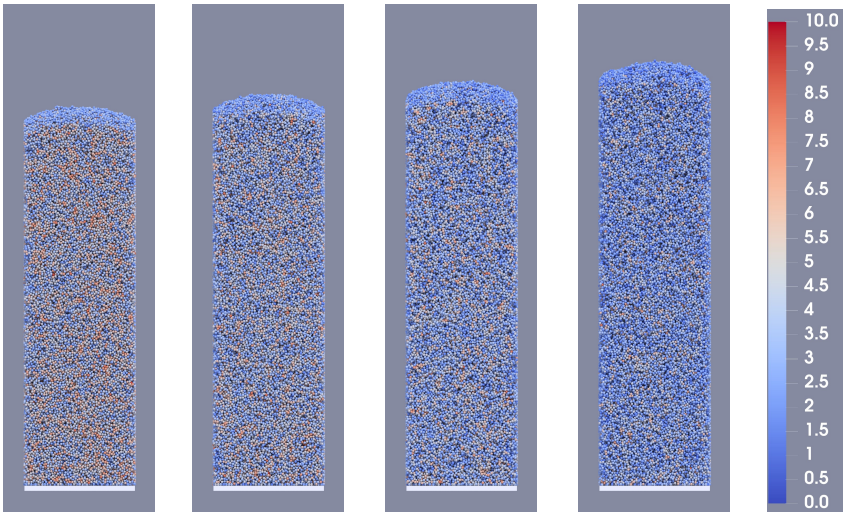

(a) $\mu_r = 0$ (b) $\mu_r = 0.2$ (c) $\mu_r = 0.4$ (d) $\mu_r = 0.8$

Figure 5.1: Static beds of original mono-dispersed particles with different coefficients of rolling resistance using the EPSD model. The colour indicates the coordination number.

Figure 5.2 shows snapshots of the particle beds with different scaling methods when $l = 4$ and $\mu_r = 0$. The bed height obtained from Method 3 is significantly higher than that of the original particles. This is mainly because of the overestimation of the cohesion force as discussed in the previous work [177] and Chapter 4. The bed heights obtained from the original particles, Method 1 and Method 2 are by and large similar. However, a subtle difference can be seen between Figure 5.2b and 5.2c: the bed height is slightly lower in Method 2. Since μ_r is 0, the only difference between them is the scaling law of the contact torque, which in Method 2 is evaluated by using Equation (3.43). Method 2 gives a larger torque during contact and hence more particle rotation than Method 1, as evidenced by the higher rotational energy observed in Figure 5.3, which can enhance the rearrangement of the particles to make a more compact bed.

Snapshots of the particle beds with different scale factors are shown in Figure 5.4 where Method 1 is used for the scaling laws. It can be said that Method 1 can qualitatively capture the effect of rolling resistance regardless of the scale factors tested.

The bulk density of the particle beds as a function of μ_r is plotted in Figure 5.5. It can be seen that the bulk density of the original particles gradually decreases with

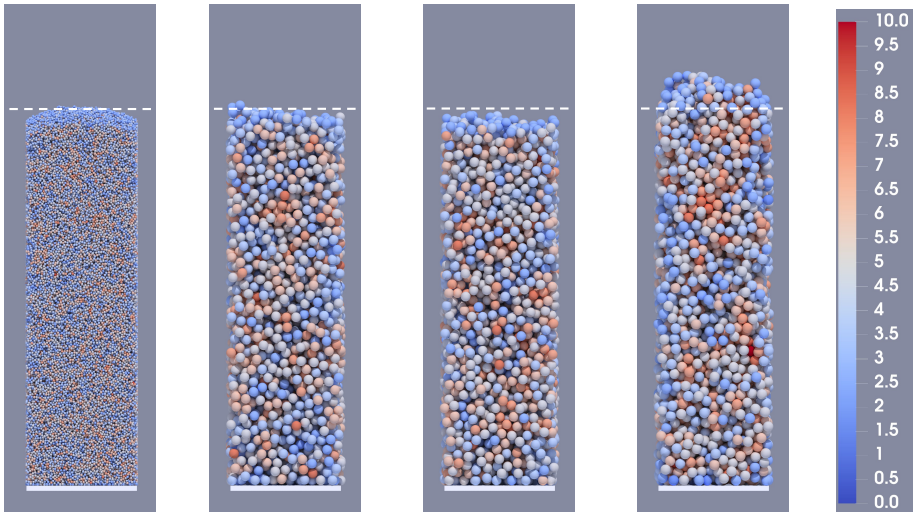

(a) Original (b) Method 1 (c) Method 2 (d) Method 3

Figure 5.2: Static particle beds with different scaling laws when $l = 4$ and $\mu_r = 0$ using the EPSD model for rolling resistance. The colour indicates the coordination number. The dashed line indicates the height of the original bed.

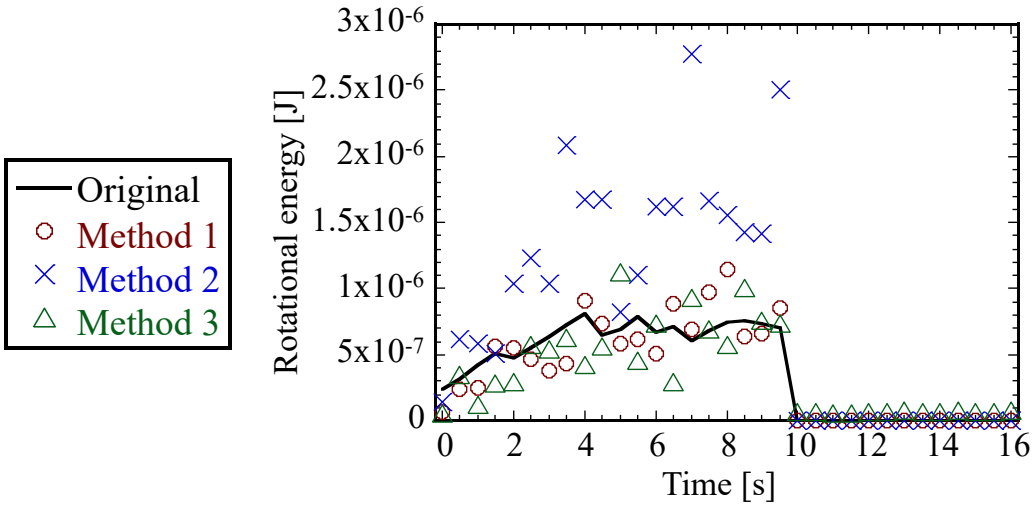

Figure 5.3: Total rotational energy of mono-dispersed particles with different scaling laws when $l = 4$ and $\mu_r = 0$ using the EPSD model for rolling resistance.

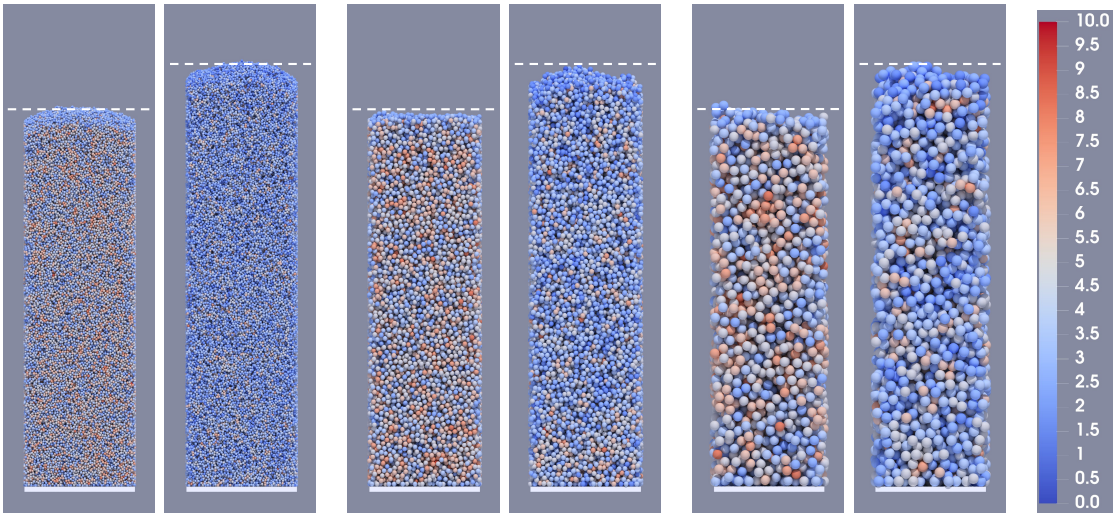

(a) Original (b) $l = 2$ (c) $l = 4$

Figure 5.4: Static beds of mono-dispersed particles with different scale factors; (left) $\mu_r = 0$ and (right) $\mu_r = 0.8$. The EPSD model is used for the rolling resistance and Method 1 is used for the scaling laws. The colour indicates the coordination number. The dashed line indicates the height of the original bed.

increasing μ_r. The bulk density is approximately 541 kg/m^3 when $\mu_r = 0$ and 484 kg/m^3 when $\mu_r = 0.8$, i.e., more than 10% difference between them. In Method 1, the bulk density of the original system is well replicated, and the results of $l = 2$ and 4 are almost identical, which is preferable as a coarse grain model. The results obtained from Method 2 are also close to the original results. However, the deviation from the original results is comparatively larger than that of Method 1, and it is more pronounced as the scale factor increases. This implies that l^3 scaling could not represent the inter-particle torques and the resultant rotation of the original particles. In Method 3, the inter-particle forces are largely overestimated as discussed above, and the bed becomes significantly more porous.

The deviation from the original bulk density is plotted in Figure 5.6. It can be seen that the deviation of Method 1 is in general small and below 0.6%. The deviation of Method 2 from the original results is slightly and yet noticeably larger than that of Method 1. On the other hand, as discussed above, the deviation of Method 3 is the largest amongst the methods tested. Therefore, it is concluded that Method 1, i.e., the SUP model, reproduces the particle behaviour of the original particles most accurately in these simulations.

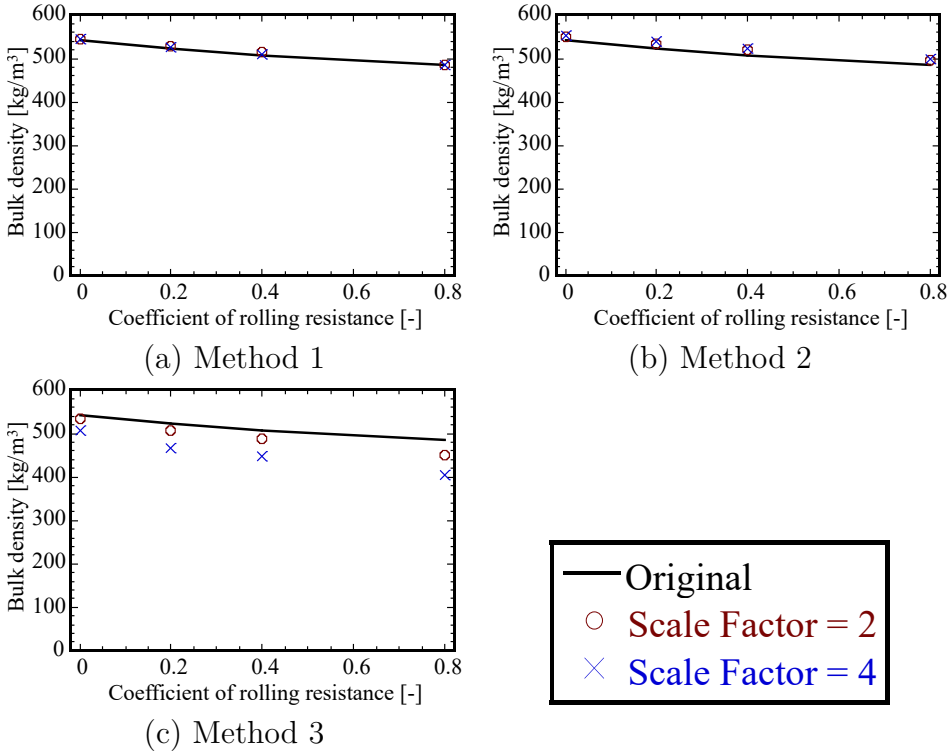

Figure 5.5: Bulk density of mono-dispersed particle beds as a function of μ_r using the EPSD model.

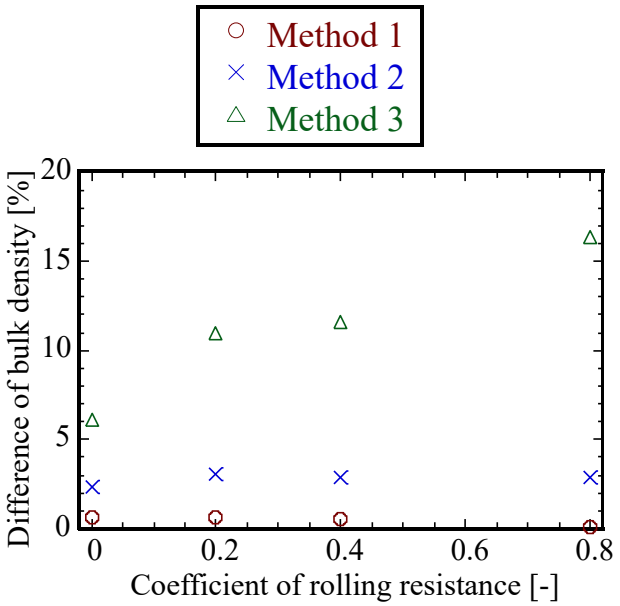

Figure 5.6: Deviation from original bulk density of mono-dispersed particles. The EPSD model is used for rolling resistance and the scale factor used is 4.

The subsequent discussion will focus on the results obtained from the simulations that utilised the CDT model. Figure 5.7 shows the bulk density of the particle beds as a function of μ_r.

The employed range of the rolling resistance coefficient is $0 \leq \mu_r \leq 0.16$ as the difference between Methods 1 and 2 is most notable for small μ_r in Figures 5.5 and 5.6. The bulk density of the original particles gradually decreases as μ_r increases as previously. It is approximately 502 kg/m^3 when $\mu_r = 0.16$, which is slightly more than 7% decrease from the case with no rolling resistance, i.e. $\mu_r = 0$. The changes in the original bulk density are well captured by Method 1 in general, while Method 2 tends to slightly overestimate the bulk density. Method 3 underestimates the bulk density significantly.

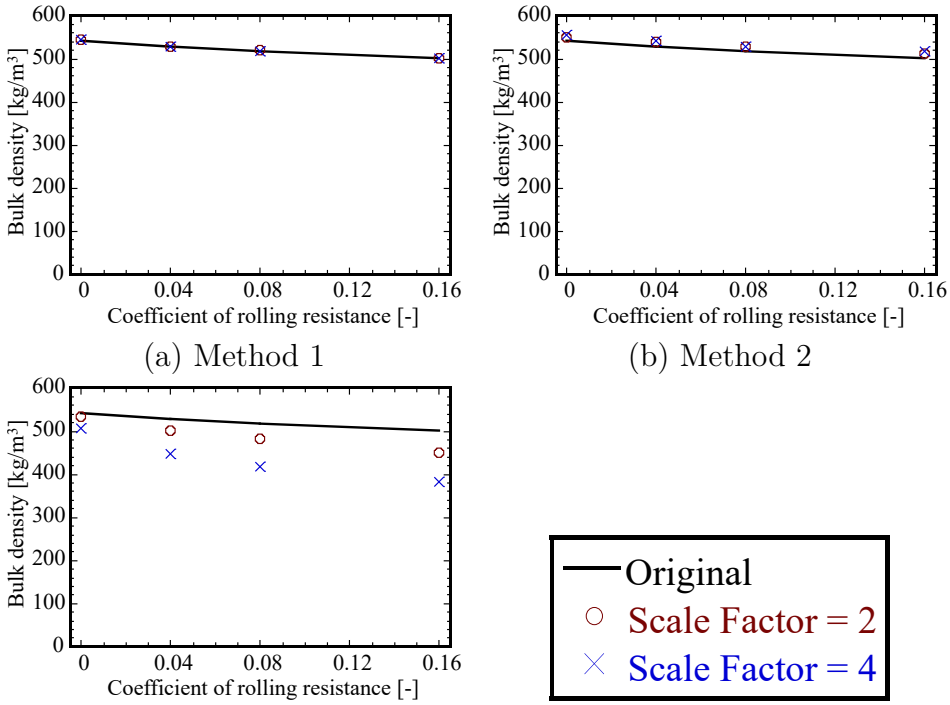

(a) Method 1

(b) Method 2

(c) Method 3

Figure 5.7: Bulk density of mono-dispersed particle beds as a function of μ_r using the CDT model.

The deviation from the original bulk density is plotted in Figure 5.8. The deviation of Method 1 is very small and less than 0.6% within the coefficient of rolling resistance tested. The deviation of Method 2 ranges between 1.9 and 2.6%, which is larger than

that of Method 1.

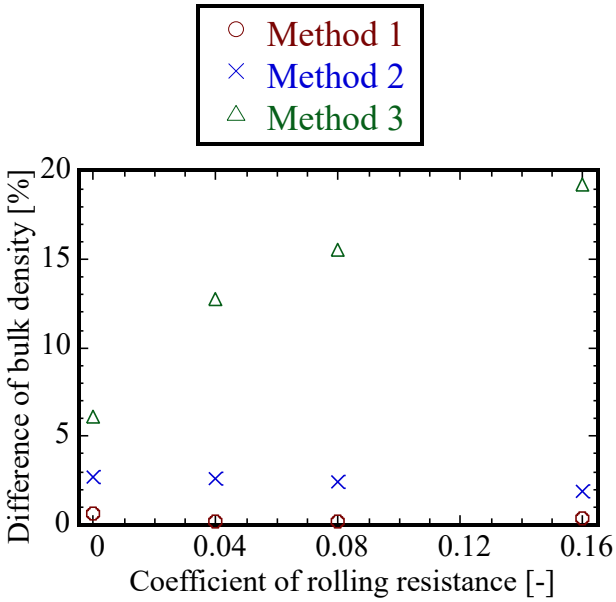

Figure 5.8: Deviation from original bulk density of mono-dispersed particles. The CDT model is used for rolling resistance and the scale factor used is 4.

In conclusion, for both the EPSD and CDT models, Method 1 demonstrates the best agreement with the bulk density of the original particles among the three scaling methods. These results support the fact that the scaling laws derived in the SUP model are generic and can be used for any forces and torques.

5.3 Angle of repose evaluation

In this section, heap formation of cohesive particles is simulated to investigate the applicability of the coarse grain model to measure the angle of repose. The original particle diameter is 1 mm and other particle properties are listed in Table 5.3. The EPSD model is used for rolling resistance and μ_{r} is varied from 0 to 0.8. Particles with diameter of 2 mm are used as scaled-up particles, i.e. a scale factor of 2.

Table 5.3: Particle properties for angle of repose evaluation.

Property	Value
Particle density [kg/m^3]	1000
Young's modulus [MPa]	10
Poisson's ratio [-]	0.3
Restitution coefficient [-]	0.1
Sliding friction coefficient [-]	0.3
Surface energy [J/m^2]	0.05

Particles are randomly generated in an insertion region with a mass flow rate of 3.35 g/s and an initial downward velocity of 0.2 m/s for 10 seconds. The dimension of the insertion region is $14 \times 14 \times 260$ mm^3 which is located at 230 mm from the bottom. A square plate with a side length of 56 mm is located at the bottom as illustrated in Figure 5.9, and particles falling out of the plate are removed. The particles are settled by gravity and the projected images of the resultant heap in the x and y directions are analysed after relaxation. The angle of repose, θ_{rep}, is defined as the angle of area-equivalent triangle (Figure 5.10) as:

$$\theta_{\mathrm{rep}} = \tan^{-1}(2h/l_{\mathrm{b}}) \tag{5.1}$$

$$h = 2A_{\mathrm{p}}/l_{\mathrm{b}} \tag{5.2}$$

where l_{b} is the base length of the heap, which is defined as the side length of the plate plus the diameter of particles used in the simulation, and A_{p} denotes the projected area of the heap.

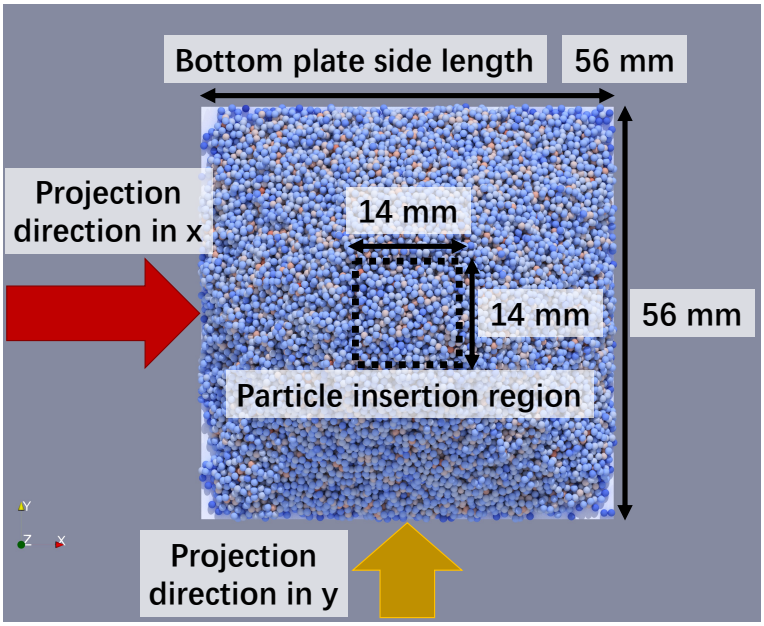

Figure 5.9: Simulation of heap formation (top view) and the direction of projection image.

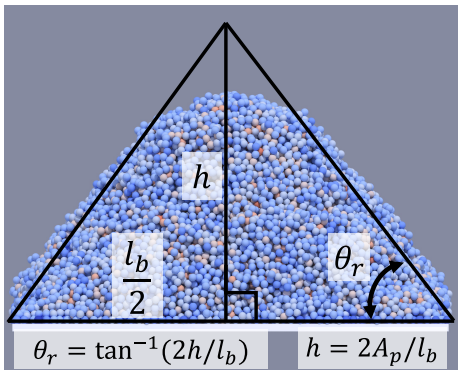

Figure 5.10: Definition of angle of repose.

Figure 5.11 shows snapshots of the particle heaps with the original particles, Method 1, Method 2 and Method 3 when $\mu_r = 0.2$. A tall heap is formed and the angle of repose of the original particles is above 50°, which is classified as "cohesive" in the Carr classification of flowability [213] as shown in Table 5.4. Typically, dry particles in the order of millimetres in size are free-flowing and one may find these simulation results counter-intuitive. This is because the Young's modulus used in the simulation is 10 MPa, which is very low as compared to typical solid materials (in the order of GPa). Consequently, the particles become cohesive due to the excessive energy dissipation during contact, which is extensively discussed in the authors' previous work [160, 161]. Nevertheless, the use of low Young's modulus is not a problem for the assessment of coarse grain models as long as the same value is used between the original and scaled-up particles. The height of the heap obtained from Method 1 is in good agreement with that of the original system. On the other hand, the heap is shorter in Method 2 due to the enhanced particle rotation caused by l^3 scaling. The shape of the heap is completely different in Method 3.

The angle of repose as a function of μ_r is plotted in Figure 5.12. In the original system, the angle of repose increases with μ_r and varies from "fair to passable flow" to "very cohesive (non-flowing)" in Table 5.4. Both Methods 1 and 2 can qualitatively capture the transition of the original flowability albeit the slight but persistent underestimation in Method 2. The angle of repose obtained from Method 3 is largely overestimated.

Table 5.4: Carr classification of powder flowability based on angle of repose.

Description	Angle of repose
Very free flowing	$< 30°$
Free flowing	30-38°
Fair to passable flow	38-45°
Cohesive	45-55°
Very cohesive (non-flowing)	$> 55°$

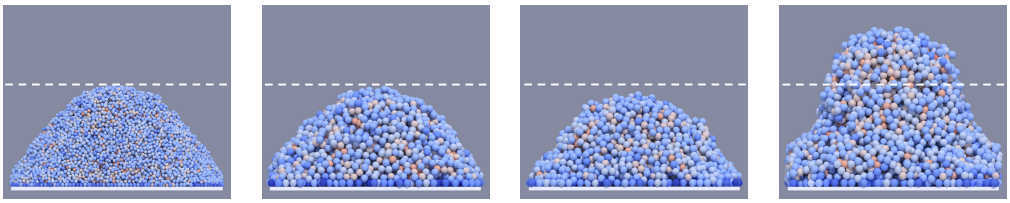

(a) Original (b) Method 1 (c) Method 2 (d) Method 3

Figure 5.11: Heap formation for angle of repose measurement with different scaling laws when $\mu_r = 0.2$. The dashed line indicates the height of the original heap.

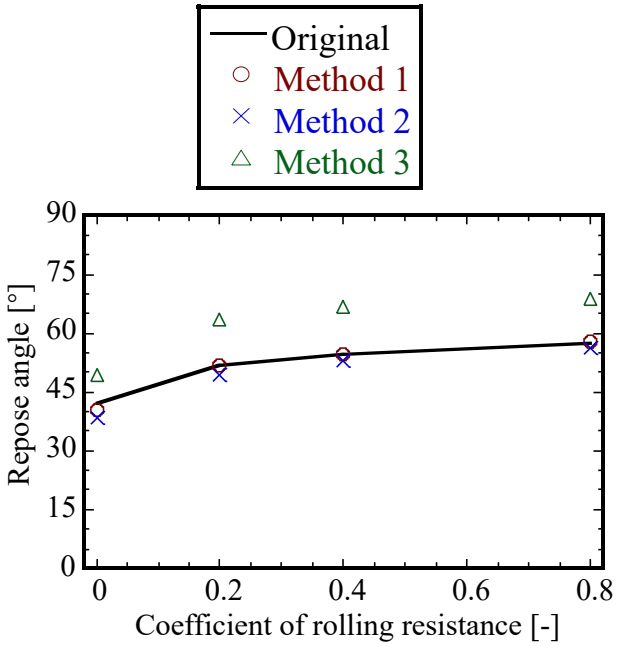

Figure 5.12: Angle of repose as a function of μ_r.

Finally, the deviation from the original angle of repose is plotted in Figure 5.13. In both Methods 1 and 2, the deviation is most notable when $\mu_r = 0$. This may be because the particles can easily fall out of the plate especially at the beginning of the simulations if the rolling resistance is not activated. This changes the time taken to form a stable first layer on the plate between the original and scaled-up particles. Note that the same parameters are used for particle-particle and particle-wall contacts in these simulations. When $\mu_r \geq 0.2$, the deviation of Method 1 is less than 1% whilst Method 2 underestimates the angle of repose by 2-5%. It can be said that Method 1 can predict the original angle of repose most accurately among the methods tested.

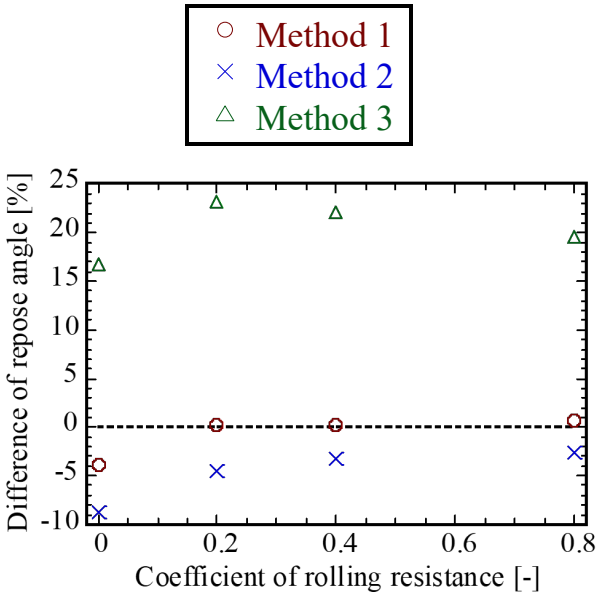

Figure 5.13: Deviation from original angle of repose.

5.4 Closure

In this chapter, the validity of the scaling law of inter-particle torques in the SUP model [173, 176, 177, 178] is investigated, which has not been properly discussed in previous work.

Three groups of scaling laws are employed in coarse grained DEM simulations, which are presented in Table 5.1. As introduced in Section 3.3.3, in the SUP model, the original inter-particle torques are first computed and then scaled-up. On the other hand, in conventional coarse grain models, the inter-particle torques are computed in the standard procedure for DEM particles using the scaled-up particle radius and forces [165, 169]. The former and latter are tested as Method 1 and Method 2, respectively, in this work. Method 3 uses l^3 for both inter-particle forces and torques for reference. A variety of simulations of particle beds and heaps were performed to measure the bulk density and angle of repose.

Bulk density is an important macroscopic property of powders and is often measured to assess their flowability and compactability. The bulk density of cohesive particle beds was evaluated in Section 5.2 to investigate the impact of different scaling methods on the bulk density of scaled-up particle beds. Both the EPSD model and CDT model of rolling resistance, which are explained in Section 2.3.3, are employed. The bulk density and bed height of particle beds are sensitive to the coefficient of rolling resistance, whereby an increase in the rolling resistance coefficient leads to a decrease in bulk density and an increase in bed height. Increased rolling resistance indicates a restriction in the flow of particles. The simulation results obtained from three different scaling methods are presented below:

- Method 1: By employing the SUP model, i.e. l^2-scaling to inter-particle forces and torques, the scaled-up particle simulation can accurately capture variations in bulk density as the rolling resistance coefficient changes.

- Method 2: Employing l^2-scaling to inter-particle forces and l^3-scaling to inter-

particle torques, the scaled-up particle simulation can generally capture variations in bulk density as the rolling resistance coefficient changes. However, the deviation from the original results is comparatively larger than that of Method 1, and it is more pronounced as the scale factor increases.

- Method 3: Employing l^3-scaling to inter-particle forces and torques, which results in significant overestimation of the inter-particle forces as discussed above, and making the scaled-up particle bed much more porous than the original particle bed.

Angle of repose is another important macroscopic property commonly used for evaluating powder flowability. The repose angle of cohesive particle heaps was evaluated in Section 5.3 to investigate the impact of different scaling methods on the repose angle of scaled-up particle heaps. The EPSD model of rolling resistance is employed. The repose angle of particle heaps is sensitive to the coefficient of rolling resistance, whereby an increase in the rolling resistance coefficient leads to a higher value of repose angle. Increased rolling resistance indicates a restriction in the flow of particles. The simulation results obtained from three different scaling methods are presented below:

- Method 1: By employing the SUP model, which involves scaling inter-particle forces and torques using l^2-scaling, the scaled-up particle simulation can generally capture variations in the repose angle as the rolling resistance coefficient changes. When considering rolling resistance, the deviation from original repose angles to those of scaled-up particles is found to be less than 1%.

- Method 2: Employing l^2-scaling to inter-particle forces and l^3-scaling to inter-particle torques, the scaled-up particle simulations underestimated the repose angle by 2-5%.

- Method 3: Employing l^3-scaling to inter-particle forces and torques, which results in significant overestimation of the repose angle.

The conclusions of this chapter are outlined below:

- The SUP model, i.e. Method 1, can successfully replicate the original bulk density using both the EPSD and CDT models for rolling resistance, which supports the fact that the scaling laws derived in the SUP model are generic and applicable to any forces and torques. On the other hand, as the scale factor increases, there is an increasing deviation observed in the conventional method, namely Method 2.
- The original angle of repose can be accurately captured using the SUP model from "fair to passable" to "very cohesive" particles in the Carr classification.

Chapter 6

The SUP model with PSDs

6.1 Introduction

This chapter includes various DEM simulations, which were conducted to validate the SUP model for DEM particles with particle size distributions (PSDs).

- Bulk density is sensitive to the change of PSDs, the bulk density of particle bed with bi-dispersed particles and particles with log-normal PSDs is evaluated, and compared the bulk density of particle beds obtained from coarse grained DEM simulation to those of the original.

- In Section 6.2, to validate the SUP model in terms of scaling inter-particle torques for particles with PSDs, three scaling laws are employed in the simulations of bi-dispersed particles, which are the same as the scaling laws employed in Chapter 5 and shown in Table 6.1.

- In Section 6.3, log-normal PSDs are employed to validate the SUP model with particles with the continuous variation of PSD from the relatively narrow PSD to the wider PSD. The impact of changes in PSDs on the bulk density of the particle bed is discussed.

Table 6.1: Methods used in the bi-dispersed particles simulations.

Method 1	Method 2	Method 3
$\boldsymbol{F}_{\mathrm{IS}} = l^2 \boldsymbol{F}_{\mathrm{IO}}$	$\boldsymbol{F}_{\mathrm{IS}} = l^2 \boldsymbol{F}_{\mathrm{IO}}$	$\boldsymbol{F}_{\mathrm{IS}} = l^3 \boldsymbol{F}_{\mathrm{IO}}$
$\boldsymbol{M}_{\mathrm{IS}} = l^2 \boldsymbol{M}_{\mathrm{IO}}$	$\boldsymbol{M}_{\mathrm{IS}} = l^3 \boldsymbol{M}_{\mathrm{IO}}$	$\boldsymbol{M}_{\mathrm{IS}} = l^3 \boldsymbol{M}_{\mathrm{IO}}$
$\boldsymbol{F}_{\mathrm{BS}} = l^3 \boldsymbol{F}_{\mathrm{BO}}$	$\boldsymbol{F}_{\mathrm{BS}} = l^3 \boldsymbol{F}_{\mathrm{BO}}$	$\boldsymbol{F}_{\mathrm{BS}} = l^3 \boldsymbol{F}_{\mathrm{BO}}$

6.2 Particle beds formation of bi-dispersed particles

As mentioned in Section 6.1, the theories used in the SUP model are generic and may be applicable to poly-dispersed systems with a particle size distribution. In this section, simulations of bi-dispersed particle beds are conducted to evaluate the bulk density. The simulation procedure is largely the same as that explained in Section 5.2. The original particle diameters are 0.5 mm and 1 mm for small and large particles, respectively. The particle density is 1000 kg/m^3, and other simulation parameters are listed in Table 5.2. The rolling resistance is given by the EPSD model, and scale factors of 2 and 4 are employed for the coarse grained simulations.

Particles are randomly generated in an insertion region with dimensions of $26 \times 26 \times 280$ mm^3 whose centre is located at 380 mm from the bottom. The size of the simulation domain in the horizontal directions is 28×28 mm^2, where the periodic boundary condition is applied. A plane wall is positioned at the bottom. The particles are inserted with a mass flow rate of 5.96 g/s and initial velocity of $(0, 0, -0.2)$ m/s for 10 seconds. The small and large particles are uniformly distributed when inserted with a mass ratio of 1:1. The particles are settled under the influence of gravity, and the bulk density is measured after relaxation. The particles below 50 mm and above 100 mm from the bottom are excluded from the bulk density measurement.

Snapshots of the particle beds obtained from the original particles, Method 1 and Method 2 when $l = 4$ and $\mu_{\mathrm{r}} = 0$ are presented in Figure 6.1. No noticeable segregation occurs and the small and large particles are uniformly distributed in the final beds. The bed height of Method 2 is slightly lower than those of the original and Method 1, as

previously observed in Figure 5.2 for mono-dispersed particles. This implies that the scaled-up particles using Method 2 can rotate more, which results in a reduced volume of the particle beds.

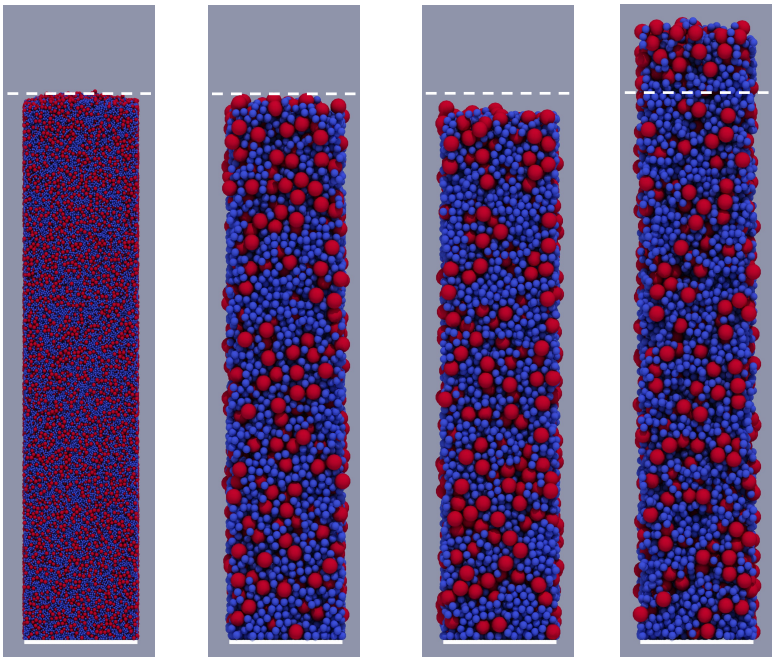

(a) Original (b) Method 1 (c) Method 2 Method 3

Figure 6.1: Static particle beds of bi-dispersed particles with different scaling laws when $l = 4$ and $\mu_r = 0$. The colour indicates the particle size; (blue) small and (red) large. The dashed line indicates the height of the original bed.

Figure 6.2 shows snapshots of particle beds with different scale factors using Method 1. Qualitatively, the bed heights obtained from the scaled-up particles are in good agreement with those of the original bed regardless of the scale factors tested.

The bulk density of the particle beds as a function of μ_r is plotted in Figure 6.3. The bulk density of the original particles is approximately 568 kg/m^3 when μ_r is 0. The bulk density is slightly higher than that of the mono-dispersed particles in Figure 5.5 (541 kg/m^3) because of (i) the large particles that are comparatively less cohesive than the small particles and (ii) small particles can fill the space between large particles. When μ_r is increased to 0.8, the original bulk density is reduced to approximately 511 kg/m^3, i.e., more than 10% drop. In general, both Methods 1 and 2 can qualitatively replicate

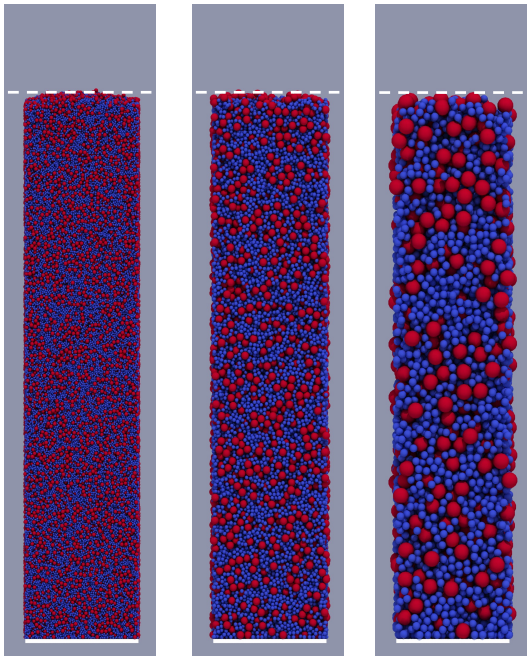

(a) Original (b) $l = 2$ (c) $l = 4$

Figure 6.2: Static beds of bi-dispersed particles with different scale factors when $\mu_r = 0$. Method 1 is used for the scaling laws. The colour indicates the particle size; (blue) small and (red) large. The dashed line indicates the height of the original bed.

the original bulk density. However, with a closer look, one may notice that the deviation increases progressively as the scale factor increases in Method 2. The results are less sensitive to the scale factor in Method 1, and the deviation is in general small.

Figure 6.4 shows the deviation from the original bulk density when $l = 4$. The deviation of Method 1 is less than 2%, whilst that of Method 2 consistently exceeds 3% and reaches up to 4.2% when $\mu_r = 0.8$. From these results, it is inferred that the SUP model can be used for predicting the bulk density of a particle mixture with different sizes.

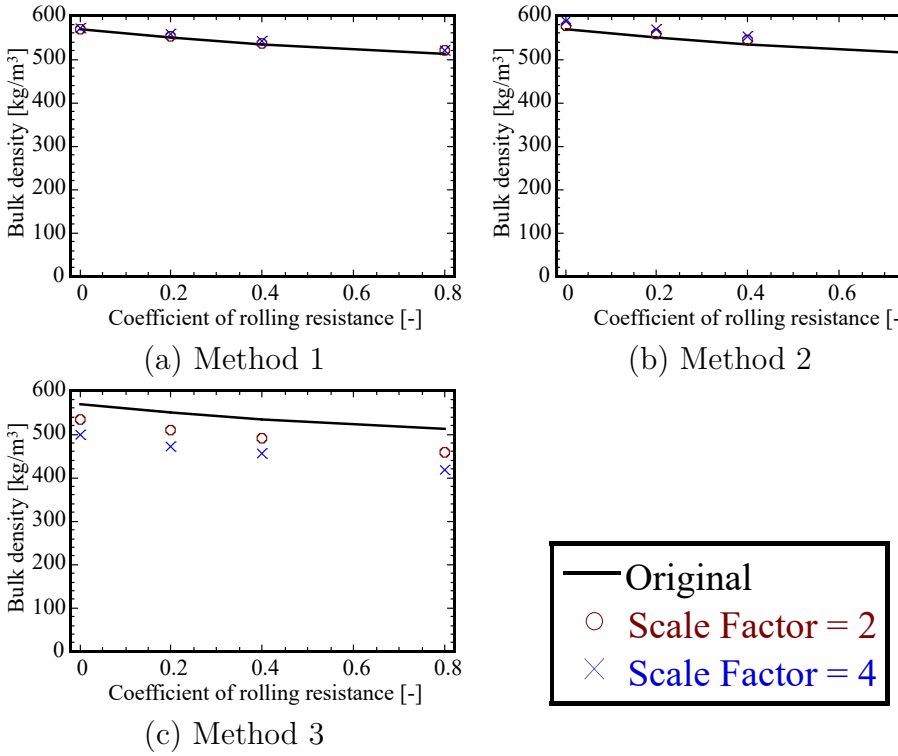

Figure 6.3: Bulk density of bi-dispersed particle beds as a function of μ_r.

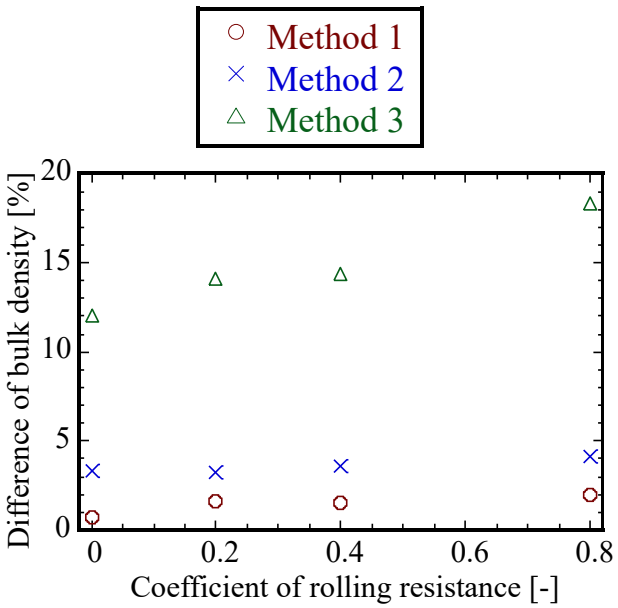

Figure 6.4: Deviation from original bulk density of bi-dispersed particles. The scale factor used is 4.

6.3 Particle beds formation with Log-normal PSDs

The bulk density, as a macroscopic property of granular materials, is closely associated with particle size distributions (PSDs). Simulations of particle beds with log-normal PSDs are conducted in this section to discuss the applicability of the SUP model in various PSDs.

The log-normal distribution is a continuous probability distribution of a random variable, where the natural logarithm of the variable follows a normal distribution. In other words, if the random variable X is log-normally distributed, then Y = ln(X) has a normal distribution. The focus of a log-normal distribution lies in the behaviour of the natural logarithm ln(X) of the random variable X within a normal distribution. This means that while X itself does not follow a normal distribution, ln(X) follows a normal distribution with a mean of μ and a standard deviation of σ_{d}. The log-normal PSDs of particle diameters are given by:

$$f(x_{\mathrm{d}}|\mu,\sigma_{\mathrm{d}}) = \frac{1}{x_{\mathrm{d}}\sigma_{\mathrm{d}}\sqrt{2\pi}} \exp\left(-\frac{(\ln x_{\mathrm{d}} - \mu)^2}{2\sigma_{\mathrm{d}}^2}\right) \tag{6.1}$$

where x_{d} represents the actual value of the diameter. In a log-normal distribution, x must be a positive number ($x > 0$), as the domain of the logarithm function is positive real numbers. μ is the mean of the underlying normal distribution. σ_{d} is the standard deviation of the underlying normal distribution. The parameters μ and σ_{d} can be given by:

$$\mu = \ln\left(\frac{m_{\mathrm{d}}^2}{\sqrt{s_{\mathrm{d}}^2 + m_{\mathrm{d}}^2}}\right) \tag{6.2}$$

$$\sigma_{\mathrm{d}} = \sqrt{\ln\left(\frac{s_{\mathrm{d}}^2}{m_{\mathrm{d}}^2} + 1\right)} \tag{6.3}$$

where m_{d} and s_{d} are the mean value and the standard deviation of particle diameters. In the present work, the mean value of original particle diameter m_{dO} is set to 1 mm with a density of 1000 kg/m^3, and other particle properties used are listed in Table 6.2.

Table 6.2: Particle properties for bulk density evaluation with log-normal PSDs.

Property	Value
Particle density [kg/m^3]	1000
Young's modulus [MPa]	10
Poisson's ratio [-]	0.3
Restitution coefficient [-]	0.1
Sliding friction coefficient [-]	0.3
Surface energy [J/m^2]	0.2 and 0.02

The ratio of standard deviation to the mean value of particle diameter $s_{\mathrm{dO}}/m_{\mathrm{dO}}$ is employed to control the PSDs. The employed log-normal PSDs with different $s_{\mathrm{dO}}/m_{\mathrm{dO}}$ are presented in Figure 6.5, which are used for the simulations in this section. $s_{\mathrm{d}}/m_{\mathrm{d}}$ is varied from 0 to 80%, where $s_{\mathrm{d}}/m_{\mathrm{d}}$ being 0 indicates mono-dispersed particles, while a higher value indicates wider PSDs.

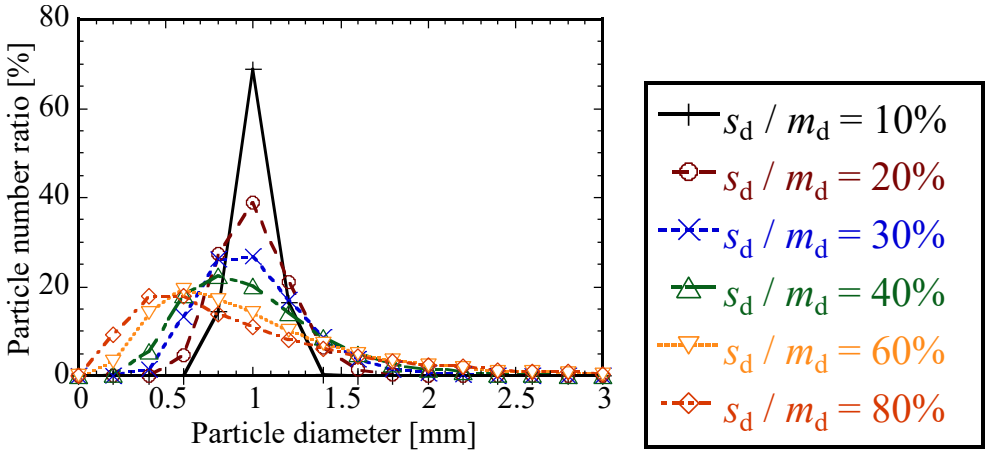

Figure 6.5: The log-normal PSDs employed in the original particle simulations.

Original particles are randomly generated in an insertion region with dimensions of $52 \times 52 \times 990$ mm^3, centred at a distance of 520 mm from the bottom. The size of the original simulation domain in the horizontal directions is 56×56 mm^2, where the periodic boundary condition is applied. A plane wall is positioned at the bottom. In the coarse grained simulations, the scale factors $l = 2$ and $l = 4$ are employed. The simulation domain and insertion region are extended in the horizontal directions, i.e., the insertion region with dimensions of $52l \times 52l \times 990$ mm^3 and the simulation domain with dimensions

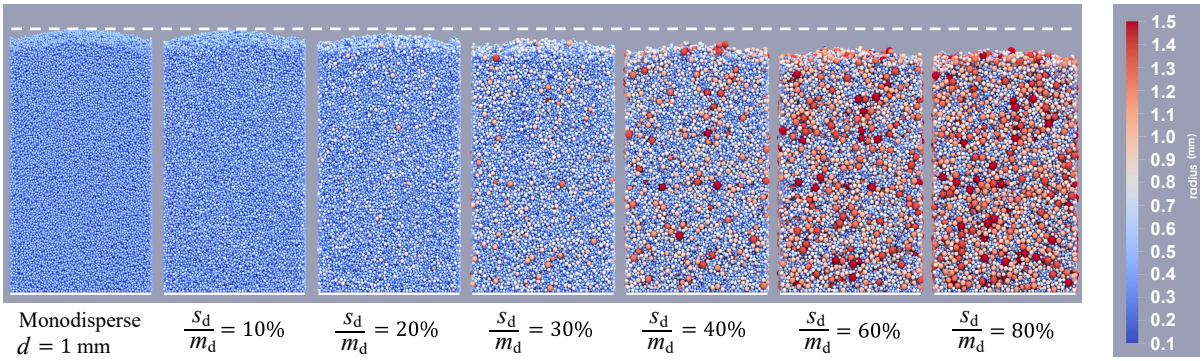

Figure 6.6: Static beds of original particles with different PSDs. The colour indicates the radius of particle (surface energy = 0.2).

of $56l \times 56l$ mm^2 are employed.

The particles are inserted at the start of the simulation with a velocity of $(0, 0, -0.2)$ m/s. The total mass of the inserted particles is 0.18g for simulations of original particles, while it amounts to 0.72g and 2.88g for the scaled-up particle simulations with scale factors of 2 and 4 respectively. The particles are settled under the influence of gravity, and the bulk density is measured after relaxation. The particles below 20 mm and above 60 mm from the bottom are excluded from the bulk density measurement to eliminate the effect of the bottom wall and bed surface.

In particle beds with PSDs, there are regions of particles that do not exert any strong force, and the non-affine movements of small particles are observed, which partially fill the void space between larger particles [84]. In this simulation, the compression strain of the particle bed under gravity is relatively small, such non-affine movement is mainly from the percolation of small particles. Namely, the movement of small particles in the void space between large particles is larger than the compression of the particle bed under gravity. As depicted in Figure 6.5, an increase in the ratio of s_d/m_d leads to the wider PSDs and the higher particle number ratio of small particles. The increase of amounts of small particles results in more percolation of small particles, which contributes to the formation of densely packed structures.

In the original particle simulations, it is evident that the bed height exhibits sensitivity

to the PSDs. Snapshots of the original particle beds with different PSDs are shown in Figure 6.6. It can be observed that the height of the particle bed decreases as s_d/m_d increases. It suggests that particles with PSDs are able to form more densely packed structures than mono-dispersed particles.

Figure 6.7 shows the bulk density of original particle beds with log-normal PSDs as a function of s_d/m_d. Surface energy $\gamma = 0.02$ and 0.2J/m^2 are employed to investigate the influence of cohesion force. Obviously, a higher surface energy corresponds to a lower bulk density because stronger adhesion prevents small particles from gravity-driven movement into the gaps between large particles.

Figure 6.8 shows the average coordination number of original particle beds with log-normal PSDs as a function of s_d/m_d. Surface energy $\gamma = 0.02$ and 0.2J/m^2 are employed to investigate the influence of cohesion force. Obviously, a higher surface energy corresponds to a lower average coordination number due to the stronger cohesion force resulting in more porous structures of particle beds and average coordination number decreases.

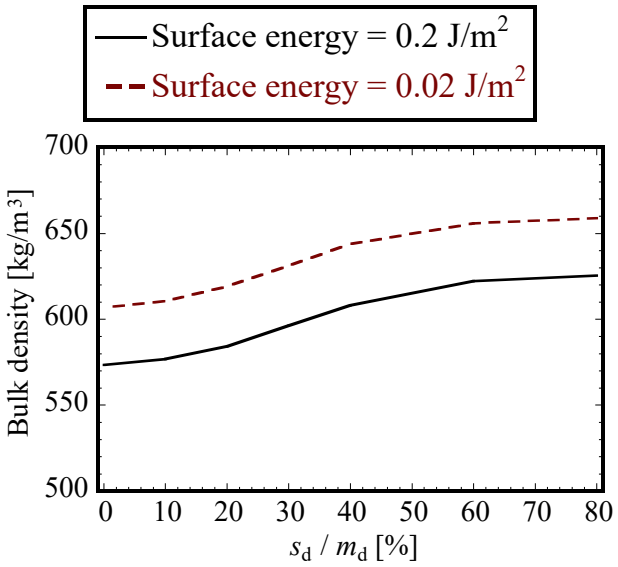

Figure 6.7: The bulk density of original particle beds with log-normal PSDs, as a function of s_d/m_d.

The bulk density of the particle beds as a function of s_d/m_d is plotted in Figure 6.9. It can be seen that the bulk density of the original particles gradually increases with

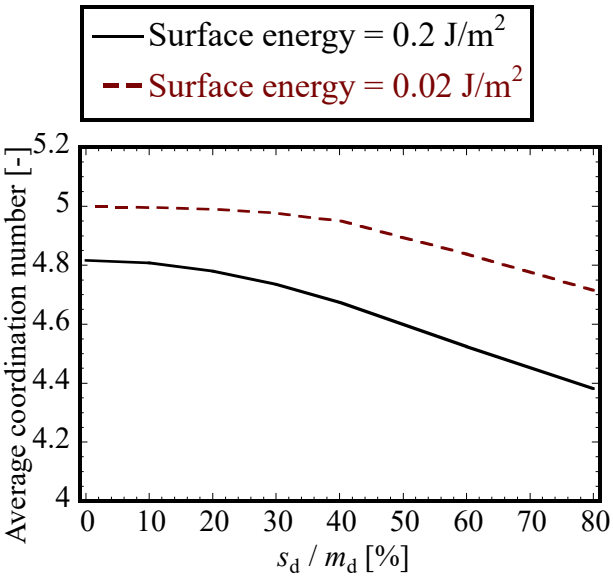

Figure 6.8: The average coordination number of original particle beds with log-normal PSDs, as a function of s_d/m_d.

increasing s_d/m_d. The bulk density is approximately 573 kg/m^3 when $s_d/m_d = 0$ and 625 kg/m^3 when $s_d/m_d = 80\%$, i.e., more than 9% difference between them. In Method 1, the bulk density of the original system is well replicated, and the results of $l = 2$ and 4 are almost identical.

The average coordination number of the particle beds as a function of s_d/m_d is plotted in Figure 6.10. It can be seen that the average coordination number of the original particles gradually decreases with increasing s_d/m_d. The average coordination number is approximately 4.82 when $s_d/m_d = 0$ and 4.38 when $s_d/m_d = 80\%$, i.e., more than 9% difference between them. The SUP model can well replicate the average coordination number of the original particles, and the results of $l = 2$ and 4 are almost identical.

It is concluded that, when $\gamma = 0.2$, the SUP model can reproduce the bulk density and average coordination number of the original particles precisely.

It is also important to discuss the impact of cohesion force magnitude on the bulk density of particle beds with PSDs. A series of simulations are conducted with the surface energy $\gamma = 0.02$ J/m^2. The bulk density of the particle beds as a function of s_d/m_d is

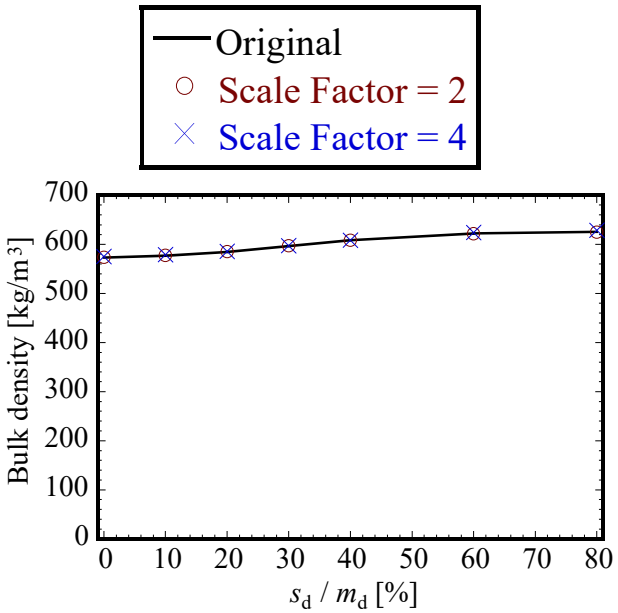

Figure 6.9: Bulk density of particle beds with log-normal PSDs as a function of s_d/m_d (γ = 0.2 J/m^2).

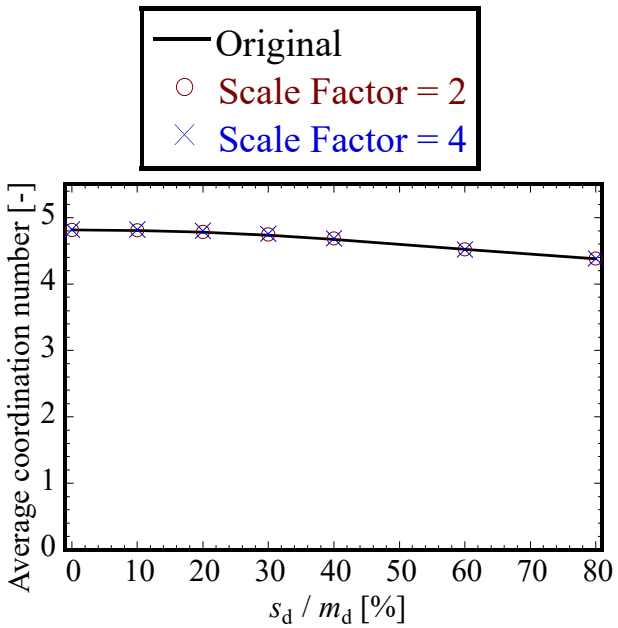

Figure 6.10: Average coordination number of particle beds with log-normal PSDs as a function of s_d/m_d (γ = 0.2 J/m^2).

plotted in Figure 6.11. The bulk density of the original particles shows a gradual increase with the increasing ratio of s_d/m_d. The bulk density increases from approximately 606 kg/m^3 at $s_d/m_d = 0$ to 658 kg/m^3 at $s_d/m_d = 80\%$, which provides a significant difference over 8%. When employing surface energy $\gamma = 0.02$ J/m^2, the bulk density of particle beds is higher than that of particle beds where the surface energy is 0.2 J/m^2. The overall deviation from the original bulk density to that of a scale factor of 4 is less than 0.5%, which implies that the SUP model can accurately replicate the bulk density of the original system, with nearly identical results for $l = 2$ and $l = 4$.

The average coordination number of the particle beds as a function of s_d/m_d is plotted in Figure 6.12. It can be seen that the average coordination number of the original particles gradually decreases with increasing s_d/m_d. The average coordination number is approximately 4.99 when $s_d/m_d = 0$ and 4.72 when $s_d/m_d = 80\%$, i.e., more than 5% difference between them, which is lower than the difference of average coordination number when adopt $\gamma = 0.2$ J/m^2. It is observed that there is a slight deviation from original average coordination number to that of scaled-up particles when $s_d/m_d = 80\%$. The deviation in coordination number from the original to scale factors 2 and 4 is approximately 0.04 and 0.12, respectively. The SUP model can generally replicate the average coordination number of the original particles when adopting a relatively lower surface energy, although it may not be exactly the same.

In conclusion, Method 1, i.e. the SUP model, accurately reproduces the bulk density of particle beds in these simulations. In general, reducing surface energy does not influence the accuracy of Method 1 to reproduce the bulk density. For average coordination number, the results from the SUP model are not exactly the same as those of original, but the deviation is still considerable small. The combination of the results from this section and those in Section 6.2 supports the idea that the scaling laws derived in the SUP model are applicable universally across various PSDs.

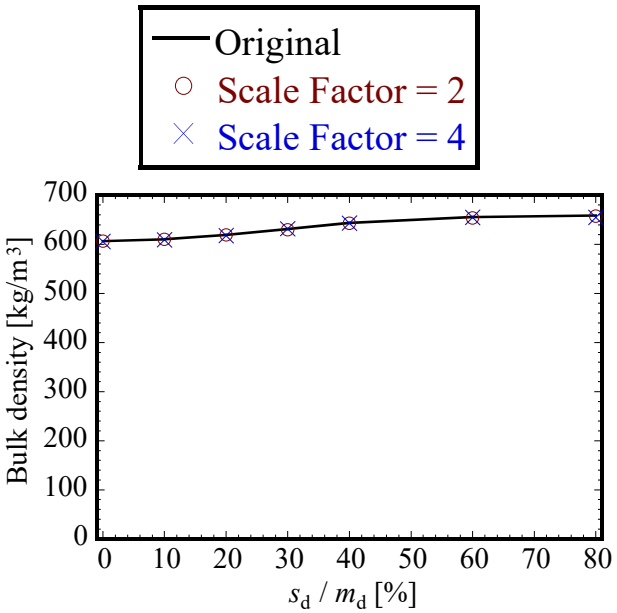

Figure 6.11: Bulk density of particle beds with log-normal PSDs as a function of $s_\mathrm{d}/m_\mathrm{d}$ ($\gamma = 0.02$ J/m^2).

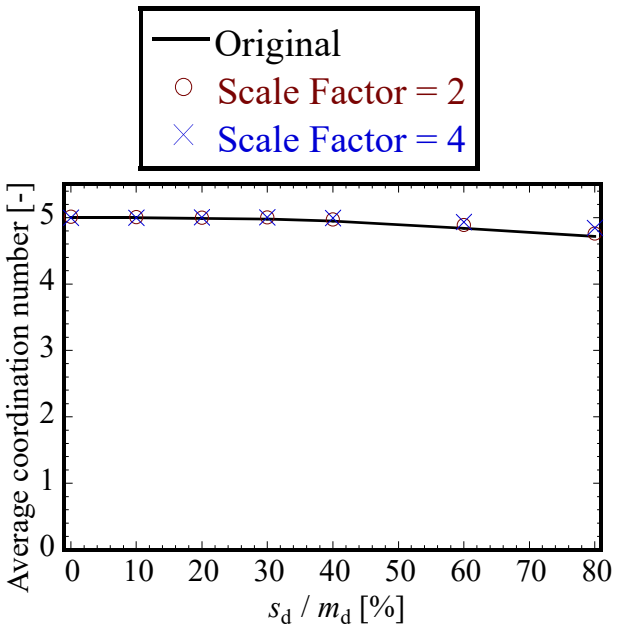

Figure 6.12: Average coordination number of particle beds with log-normal PSDs as a function of $s_\mathrm{d}/m_\mathrm{d}$ ($\gamma = 0.02$ J/m^2).

6.4 Closure

In this chapter, the applicability of the SUP model is validated in various particle size distributions (PSDs). Bulk density of particle beds is sensitive to the variation of PSDs, which is therefore employed to investigate the validity of the SUP model to various PSDs. The simulation employs the evaluation of cohesive particle beds using bi-dispersed particles to represent one type of discrete particle size distribution, while particles with log-normal PSDs are used to represent a continuous change in particle size distribution. In this chapter, three scaling laws are employed, and the SUP model, i.e. Method 1, has demonstrated its potential as a promising approach capable of reproducing the bulk density of original particles across various PSDs.

In Section 6.2, the simulations of bi-dispersed particles, as an extended validation of the torque scaling laws validated in Chapter 5, the focus is more on comparing torque scaling:

- Method 1: By employing the SUP model, i.e. l^2-scaling to inter-particle forces and torques, the scaled-up particle simulation can accurately capture variations in bulk density as the rolling resistance coefficient changes.

- Method 2: Employing l^2-scaling to inter-particle forces and l^3-scaling to inter-particle torques, the scaled-up particle simulation can generally capture variations in bulk density as the rolling resistance coefficient changes. However, the deviation from the original results is comparatively larger than that of Method 1, and it is more pronounced as the scale factor increases.

- Method 3: Employing l^3-scaling to inter-particle forces and torques results in significant overestimation of the inter-particle forces, as discussed above, which makes the scaled-up particle bed much more porous than the original particle bed.

In Section 6.3, the simulations of particles with log-normal PSDs are conducted as a

validation of various PSDs. The focus is to validate whether the SUP model can accurately capture the continuous variation of PSDs. By employing the SUP model, i.e. l^2-scaling to inter-particle forces and torques, the scaled-up particle simulation can accurately capture variations in bulk density as the PSDs change.

The SUP model, i.e. Method 1, successfully replicated the original bulk density of bi-dispersed particles and particles with log-normal PSDs, which indicates the SUP model can be used for predicting the bulk density of a particle mixture with different sizes and theoretically applicable to any type of PSDs.

Chapter 7

Closure

7.1 Summary

In previous works of coarse grain models of DEM, the scaling laws are usually derived for specific types of forces [165, 166, 169], which presents a challenge when applying coarse grain models of DEM to simulate granular materials with various types of forces and torques. The present study develops a novel coarse grain model of DEM that can be universally applied to scale various types of forces and torques. Furthermore, it is proven applicable to particles with various PSDs. The proposed model is called the scaled-up particle (SUP) model.

The SUP model can significantly reduce the computational cost of DEM simulation. One of the greatest advantages of the developed model is that it is derived in a way that is not relevant to any specific type of inter-particle forces and torques. Although the validation simulations do not cover all types of inter-particle forces and torques, the theory and basic assumptions of the SUP model do not limit its capability to scale any type of inter-particle forces and torques.

In the SUP model, the particle overlap and separation distance of original particles are evaluated based on geometric similarity using the corresponding scaled-up particle variables, which differs from the conventional method in the literature [165, 173]. The translational and rotational velocities are determined in such a way that the same kinetic

energies can be achieved between the original and scaled-up particles as suggested by Sakai and Koshizuka [165]. In chapters 4, 5, and 6, the SUP model is validated for its applicability to particle systems involving various inter-particle forces, torques, and particle size distributions respectively.

The comparisons of simulation results with different methods presented in sections 4.2 and 4.3 in Chapter 4 provide several insights for evaluating inter-particle forces in coarse-grained DEM simulation, as summarised below:

- The results demonstrate that the proposed method, the SUP model, can provide an almost identical stress-strain curve to that of the original system during the uniaxial compression of a packed particle bed, where particle contact forces are dominant.
- Furthermore, the same method can accurately reproduce the overall flow structure and velocity distributions of the original particles in a dynamic system, such as a vertical mixer, where capillary and Johnson-Kendall-Roberts (JKR) surface adhesion forces, i.e. inter-particle attraction forces, are dominant.
- Slight discrepancies are observed when the attraction forces are relatively large. This could potentially be attributed to the formation of medium-sized lumps that cannot be resolved with larger scaled-up particles.
- The comparisons in the simulations of particle bed compression and particle flow in a vertical mixer suggest that accurately evaluating inter-particle overlap and separation distance is crucial in coarse-grained DEM simulation.
- Among the three investigated methods, the SUP model, i.e. Method 1, demonstrated the best agreement with the results of original particles. In principle, it can be applied to any type of inter-particle force.

The concept of inter-particle torques scaling in the SUP model, as introduced in Section 3.3.3, differs from that of conventional coarse grain models. This difference in concept

provides different scaling laws of inter-particle torques. The comparisons of simulation results presented in sections 5.2 and 5.3 provide several insights for inter-particle torques evaluation in coarse-grained DEM simulation, as summarised below:

- By applying l^2-scaling to inter-particle torques and forces, the SUP model can successfully reproduce the original bulk density for both the EPSD and CDT models of rolling resistance. This supports the fact that the scaling laws derived in the SUP model are generic and can be used for any forces and torques.

- Method 2 employs l^2-scaling for inter-particle forces but l^3-scaling for torques. The deviation of the conventional coarse grain model in bulk density is generally higher than that of the SUP model, and it increases as the scale factor increases. The bulk density obtained by Method 2 is slightly higher than that of the original particles, which implies that Method 2 overestimated the inter-particle torques, resulting in excess particle rearrangement and leading to the formation of more densely compacted structures than those of the original particles.

- In the simulations for evaluating the angle of repose, the SUP model accurately captures the original angle of repose for particles classified as "fair to passable" to "very cohesive" according to Carr's classification. The overestimated torques of Method 2 yield the underestimation of repose angle.

- The comparisons in the simulations evaluating bulk density and repose angle of cohesive particles suggest that accurately estimating inter-particle torques is crucial in coarse-grained DEM simulation.

- Among the three investigated methods, the SUP model, i.e. Method 1, showed the best agreement with the results of original particles, and in principle, it can be applied to any type of inter-particle torque.

In the previous works of the SUP model, mono-dispersed particles are employed for

simplicity [173, 176, 177], which includes the simulations in chapters 4 and 5. However, the theories employed in the SUP model are generic and have potential applicability to more complex systems. The comparisons of simulation results presented in Sections 6.2 and 6.3 provide several insights of particle size distributions (PSDs) in coarse-grained DEM simulation, as summarised below:

- In Section 6.2, the bulk density of particle beds is evaluated and compared, the bi-dispersed particles are employed. The l^2-scaling of inter-particle torques, which was validated in Chapter 5 for mono-dispersed particles, is also applicable to bi-dispersed particles.

- In Section 6.3, the bulk density of particle beds are evaluated and compared, the particles with log-normal PSDs are employed. The l^2-scaling of inter-particle torques is validated, that it is also applicable to particles with various PSDs.

- In the aforementioned simulations, the SUP model successfully replicated the original bulk density of bi-dispersed particles and particles with log-normal PSDs. This indicates that the SUP model can be utilised to predict the bulk density of a particle mixture with various particle size distributions. In principle, the SUP model can be applied to particle systems with any type of particle size distribution.

In addition, the scaling law of the critical time step for the SUP model that was introduced in Section 2.4 is further validated through the simulation of particles in a periodic boundary box with no energy dissipation, as discussed in Section 4.4. The results suggest that the time step for the scaled-up particle can be l times larger than that of the original particle.

7.2 Future directions

The suggestions for future work are listed as follows:

- Slight discrepancies between the velocity distribution of scaled-up particles and original particles are observed in Section 4.3 of Chapter 4, particularly when the attraction forces are relatively large. This may be attributed to the formation of medium-sized lumps that cannot be resolved with larger scaled-up particles. Therefore, gaining a deeper understanding of the causes for the observed deviations and, if feasible, expanding the applicable scope of the SUP model would be valuable.

- The SUP model has been validated for various types of PSDs in static particle beds, as discussed in Chapter 6. Given that particle beds with different PSDs have been simulated, it is easy to consider compressing particle beds with varying PSDs and validating whether the SUP model can replicate the stress-strain curve of the original particles with various PSDs. In addition, its applicability to dynamic particle systems with different PSDs has not yet been validated. Therefore, it would be valuable to deeply investigate the applicability of the SUP model in dynamic particle systems, such as particle flow in mixers and fluidised beds.

- Since this study focuses on discussing the validity of the proposed coarse grain model for various types of forces and torques, a maximum scale factor of 4 is employed. However, theoretically, as long as the particles follow the effectively homogeneous assumption, the SUP model does not impose any limitations on the scale factor. Namely, the limitation of scale factor is primarily determined by the specific particle system rather than the SUP model. It would be valuable to apply larger scale factors for validation simulations involving more particle systems.

- In the derivation of the SUP model, the mentioned three mechanisms leading to the change in momentum are assumed to be equivalent at control volume scale for the original and scaled-up particles. However, the model does not discuss the energy dissipation of particles in the control volume, which is different for particles of the same mass after the particle size enlargement. This is a promising direction to

improve the existing coarse grain model of DEM.

- The clear applicable size range of the effectively homogeneous assumption still requires further investigation. It would be valuable to explore the minimum and maximum particle sizes that can be captured by the SUP model.

Appendix A

Simulations of particle flow in a vertical mixer with $D/d \geq 40$

The proposed model has provided good agreements between original and scaled-up results while $D/d > 40$. As mentioned in Section 4.3, the D/d is recommended to be larger than 40, which limits the range of scale factor selection. This is a kind of limitation from geometry, as larger particles have the risk of enhancing the influence of boundary effects.

The mixer simulations of the larger scale factor have been conducted to test the influences of boundary effects. The simulation conditions were the same as those used for the mixer simulations of wet particles in Section 4.3.1 with $\lambda_{\mathrm{L}} = 0.05$ N/m. Employed the larger particles are 4 and 8 mm in diameters, while $l = 8$ and 16, $D/d = 21$ and 10.5 respectively. Figure A.1 shows the results of probability distribution of particles velocity. It is clear that the distribution peak is shifted leftward while gradually increasing the scale factor. The deviation from the original results is remarkable, especially for the cases where $D/d < 40$. These results provide a reference for the particle size limitation of model applications and support the opinion in the literature [211, 212] that D/d should be set larger than 40.

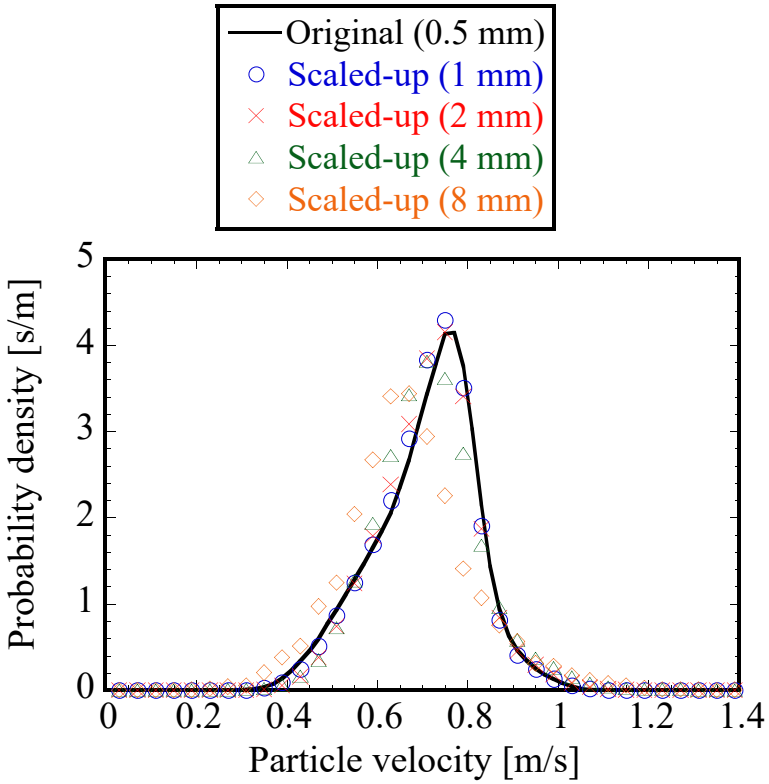

Figure 1: Probability density distribution of particle velocity magnitude in vertical mixer with capillary force including the larger scale factor results (Method 1, $\lambda_{\mathrm{L}} = 0.05$ N/m).

References

[1] P. Richard, M. Nicodemi, R. Delannay, P. Ribière, D. Bideau, Slow relaxation and compaction of granular systems, Nature Materials, Vol. 4, pp. 121–128 (2005).

[2] S. J. Antony, W. Hoyle, Y. Ding, Granular Materials: Fundamental and Applications, Royal Society of Chemistry, 2004.

[3] R. M. Nedderman, Statics and Kinematics of Granular Materials, Cambridge University Press, 1992.

[4] U. E. Shamy, M. Zeghal, Coupled Continuum-Discrete Model for Saturated Granular Soils, Journal of Engineering Mechanics, Vol. 131, pp. 413–426 (2005).

[5] Y. Guo, X. B. Yu, Comparison of the implementation of three common types of coupled CFD-DEM model for simulating soil surface erosion, International Journal of Multiphase Flow, Vol. 91, pp. 89–100 (2017).

[6] Y. Guo, C. Wang, M. Lu, X. B. Yu, Numerical investigations on evolution mechanism of contact erosion in layered soils considering particle-scale parameters, Transportation Geotechnics, Vol. 41, 101023 (2023).

[7] R. Sun, H. Xiao, H. Sun, Realistic representation of grain shapes in CFD–DEM simulations of sediment transport with a bonded-sphere approach, Advances in Water Resources, Vol. 107, pp. 421–438 (2017).

[8] H. Elghannay, D. Tafti, LES-DEM simulations of sediment transport, International Journal of Sediment Research, Vol. 33, pp. 137–148 (2018).

[9] E. Harada, H. Gotoh, H. Ikari, A. Khayyer, Numerical simulation for sediment transport using MPS-DEM coupling model, Advances in Water Resources, Vol. 129, pp. 354–364 (2019).

[10] W. C. Li, H. J. Li, F. C. Dai, L. M. Lee, Discrete element modeling of a rainfall-induced flowslide, Engineering Geology, Vol. 149-150, pp. 22–34 (2012).

[11] Z. M. Shi, H. C. Zheng, S. B. Yu, M. Peng, T. Jiang, Application of CFD-DEM to investigate seepage characteristics of landslide dam materials, Computers and Geotechnics, Vol. 101, pp. 23–33 (2018).

[12] Z. Liu, L. Su, C. Zhang, J. Iqbal, B. Hu, Z. Dong, Investigation of the dynamic process of the Xinmo landslide using the discrete element method, Computers and Geotechnics, Vol. 123, 103561 (2020).

[13] T. T. Vo, D. M. Tran, C. T. Nguyen, T. K. Nguyen, Discrete element investigation of the mobility of granular mass flows, Solid State Communications, Vol. 369, 115190 (2023).

[14] T. Shan, J. Zhao, A coupled CFD-DEM analysis of granular flow impacting on a water reservoir, Acta Mechanica, Vol. 225, pp. 2449–2470 (2014).

[15] G. G. Zhou, J. Du, D. Song, C. E. Choi, H. S. Hu, C. Jiang, Numerical study of granular debris flow run-up against slit dams by discrete element method, Landslides, Vol. 17, pp. 585–595 (2020).

[16] W. Mao, Y. Wang, P. Yang, Y. Huang, H. Zheng, Dynamics of granular debris flows against slit dams based on the CFD−DEM method: effect of grain size distribution and ambient environments, Acta Geotechnica, Vol. 18, pp. 5811–5838 (2023).

[17] F. J. Muzzio, T. Shinbrot, B. J. Glasser, Powder technology in the pharmaceutical industry: The need to catch up fast, Powder Technology, Vol. 124, pp. 1–7 (2002).

[18] D. Fichana, A. J. Marchut, P. H. Ohlsson, S. Y. Chang, O. Lyngberg, J. Dougherty, S. Kiang, H. Stamato, B. Chaudhuri, F. Muzzio, Experimental and model-based approaches to studying mixing in coating pans, Pharmaceutical Development and Technology, Vol. 14, pp. 173–184 (2009).

[19] D. Sunkara, M. Capece, Influence of Material Properties on the Effectiveness of Glidants Used to Improve the Flowability of Cohesive Pharmaceutical Powders, AAPS PharmSciTech, Vol. 19, pp. 1920–1930 (2018).

[20] K. Tahara, Pharmaceutical formulation and manufacturing using particle/powder technology for personalized medicines, Advanced Powder Technology, Vol. 31, pp. 387–392 (2020).

[21] J. H. Finke, A. Kwade, Powder processing in pharmaceutical applications—in-depth understanding and modelling, Pharmaceutics, Vol. 13, pp. 1–3 (2021).

[22] B. R. Bird, W. E. Stewart, E. N. Lightfoot, Transport Phonemena, John Wiley & Sons, 1960.

[23] M. Massoudi, Remarks on Constitutive Modeling of Granular Materials, Eng, Vol. 4, pp. 2856–2878 (2023).

[24] J. C. Richards, The Storage and Recovery of Particulate Solids: A Report of a Working Party of the Institution of Chemical Engineers, Institution of Chemical Engineers, 1966.

[25] R. L. Brown, J. C. Richards, Principles of Powder Mechanics: Essays on the Packing and Flow of Powders and Bulk Solids, Pergamon Press, 1970.

[26] D. Geldart, Types of gas fluidization, Powder Technology, Vol. 7, pp. 285–292 (1973).

[27] R. Cocco, J. W. Chew, 50 years of Geldart classification, Powder Technology, Vol. 428, 118861 (2023).

[28] G. Bonifazi, F. L. Marca, P. Massacci, Characterization of bulk particles in real time, Particle and Particle Systems Characterization, Vol. 19, pp. 240–246 (2002).

[29] D. Schulze, J. Schwedes, J. W. Carson, Powders and bulk solids: Behavior, characterization, storage and flow, Springer Berlin Heidelberg, 2008.

[30] M. L. Tan, I. Goldhirsch, Rapid Granular Flows as Mesoscopic Systems, Physical Review Letters, Vol. 81, pp. 3022–3025 (1998).

[31] S. A. Dunatunga, A framework for continuum simulation of granular flow, PhD dissertation, Massachusetts Institute of Technology, 2017.

[32] D. Fenistein, M. V. Hecke, Wide shear zones in granular bulk flow, Nature, Vol. 425, pp. 256–256 (2003).

[33] D. Fenistein, J. W. V. D. Meent, M. V. Hecke, Universal and wide shear zones in granular bulk flow, Physical Review Letters, Vol. 92, 094301 (2004).

[34] S. Shioji, K. Tokami, H. Yamamoto, A. Suganuma, Control of the bulk flow of granular materials by an aeration technique, Powder Technology, Vol. 72, pp. 215–221 (1992).

[35] H. M. Jaeger, S. R. Nagel, R. P. Behringer, The Physics of Granular Materials, Physics Today, Vol. 49, pp. 32–38 (1996).

[36] I. Goldhirsch, Stress, stress asymmetry and couple stress: From discrete particles to continuous fields, Granular Matter, Vol. 12, pp. 239–252 (2010).

[37] J. Dettmar, C. Miehe, Alternative Definitions of Micro-to-Macro Transitions in Particle Aggregates of Granular Materials, PAMM, Vol. 3, pp. 264–265 (2003).

[38] C. Miehe, J. Dettmar, A framework for micro-macro transitions in periodic particle aggregates of granular materials, Computer Methods in Applied Mechanics and Engineering, Vol. 193, pp. 225–256 (2004).

[39] S. Roy, A. Singh, S. Luding, T. Weinhart, Micro-macro transition and simplified contact models for wet granular materials, Computational Particle Mechanics, Vol. 3, pp. 449–462 (2016).

[40] H. Hertz, Miscellaneous Papers, London: Macmillan, 1896.

[41] R. D. Mindlin, H. Deresiewicz, Elastic Spheres in Contact Under Varying Oblique Forces, Journal of Applied Mechanics, Vol. 20, pp. 327–344 (1953).

[42] J. H. D. Boer, The influence of van der Waals' forces and primary bonds on binding energy, strength and orientation, with special reference to some artificial resins, Transactions of the Faraday Society, Vol. 32, pp. 10–37 (1936).

[43] F. London, The general theory of molecular forces, Transactions of the Faraday Society, Vol. 33, pp. 8–26 (1937).

[44] K. L. Johnson, K. Kendall, A. D. Roberts, Surface energy and the contact of elastic solids, Proceedings of the Royal Society of London. A. Mathematical and Physical Sciences, Vol. 324, pp. 301–313 (1971).

[45] J. Hærvig, U. Kleinhans, C. Wieland, H. Spliethoff, A. L. Jensen, K. Sørensen, T. J. Condra, On the adhesive JKR contact and rolling models for reduced particle stiffness discrete element simulations, Powder Technology, Vol. 319, pp. 472–482 (2017).

[46] S. Lin, J. Menig, L. Lachman, Interdependence of physiological surfactant and drug particle size on the dissolution behavior of water-insoluble drugs, Journal of Pharmaceutical Sciences, Vol. 57, pp. 2143–2148 (1968).

[47] A. G. Bailey, Electrostatic phenomena during powder handling, Powder Technology, Vol. 37, pp. 71–85 (1984).

[48] H. Eliasen, H. G. Kristensen, T. Schæfer, Electrostatic charging during a melt agglomeration process, International Journal of Pharmaceutics, Vol. 184, pp. 85–96 (1999).

[49] J. Peart, Powder Electrostatics: Theory, Techniques and Applications, KONA Powder and Particle Journal, Vol. 19, pp. 34–45 (2001).

[50] M. J. Adams, V. Perchard, The cohesive forces between particles with interstitial liquid, Institute of Chemical Engineering Symposium, Vol. 91, pp. 147–160 (1985).

[51] G. Lian, C. Thornton, M. J. Adams, A theoretical study of the liquid bridge forces between two rigid spherical bodies, Journal of Colloid And Interface Science, Vol. 161, pp. 138–147 (1993).

[52] O. Pitois, P. Moucheront, X. Chateau, Liquid bridge between two moving spheres: An experimental study of viscosity effects, Journal of Colloid and Interface Science, Vol. 231, pp. 26–31 (2000).

[53] Y. I. Rabinovich, M. S. Esayanur, B. M. Moudgil, Capillary forces between two spheres with a fixed volume liquid bridge: Theory and experiment, Langmuir, Vol. 21, pp. 10992–10997 (2005).

[54] M. E. Plesha, G. L. Gray, F. Costanzo, Engineering mechanics : statics, McGraw-Hill Higher Education, 2010.

[55] K. L. Johnson, Contact Mechanics, Cambridge University Press, 1985.

[56] J. N. Israelachvili, Intermolecular and Surface Forces, Third Edition, Elsevier, 2010.

[57] R. A. Bowling, A Theoretical Review of Particle Adhesion, Springer, Boston, MA, 1988, pp. 129–142.

[58] Y. S. Chu, S. Dufour, J. P. Thiery, E. Perez, F. Pincet, Johnson-Kendall-Roberts theory applied to living cells, Physical Review Letters, Vol. 94, 028102 (2005).

[59] S. Li, J. S. Marshall, G. Liu, Q. Yao, Adhesive particulate flow: The discrete-element method and its application in energy and environmental engineering, Progress in Energy and Combustion Science, Vol. 37, pp. 633–668 (2011).

[60] M. Balashanmugam, Y. S. Cheong, M. J. Hounslow, A. D. Salman, Semi-solid Paste Binder Dispersion in a Moving Powder Bed, Procedia Engineering, Vol. 102, pp. 626–633 (2015).

[61] K. Washino, E. L. Chan, T. Matsumoto, S. Hashino, T. Tsuji, T. Tanaka, Normal viscous force of pendular liquid bridge between two relatively moving particles, Journal of Colloid and Interface Science, Vol. 494, pp. 255–265 (2017).

[62] K. Washino, E. L. Chan, H. Midou, T. Tsuji, T. Tanaka, Tangential viscous force models for pendular liquid bridge of Newtonian fluid between moving particles, Chemical Engineering Science, Vol. 174, pp. 365–373 (2017).

[63] P. S. Laplace, Traité de Mécanique Céleste, Vol. 4, 1805.

[64] T. Young, An essay on the cohesion of fluids, Philosophical Transactions of the Royal Society of London, Vol. 95, pp. 65–87 (1805).

[65] C. Dominik, A. G. Tielens, Resistance to rolling in the adhesive contact of two elastic spheres, Philosophical Magazine A: Physics of Condensed Matter, Structure, Defects and Mechanical Properties, Vol. 72, pp. 783–803 (1995).

[66] D. V. Konvisarov, A. A. Pokrovskaia, Influence of the radii of curvature of cylindrical bodies on their resistance to rolling under different loads, Proc. Sib. Phys.-Tech. Inst, Vol. 34, pp. 62–79 (1955).

[67] J. J. Kalker, Three-Dimensional Elastic Bodies in Rolling Contact, Vol. 2, Kluwer Academic Publishers, 1990.

[68] K. R. Eldredge, D. Tabor, The mechanism of rolling friction. I. The plastic range, Proceedings of the Royal Society of London. Series A. Mathematical and Physical Sciences, Vol. 229, pp. 181–198 (1955).

[69] D. G. Flom, A. M. Bueche, Theory of Rolling Friction for Spheres, Journal of Applied Physics, Vol. 30, pp. 1725–1730 (1959).

[70] W. D. May, E. L. Morris, D. Atack, Rolling Friction of a Hard Cylinder over a Viscoelastic Material, Journal of Applied Physics, Vol. 30, pp. 1713–1724 (1959).

[71] K. C. Ludema, D. Tabor, The friction and visco-elastic properties of polymeric solids, Wear, Vol. 9, pp. 329–348 (1966).

[72] J. T. Oden, T. L. Lin, On the general rolling contact problem for finite deformations of a viscoelastic cylinder, Computer Methods in Applied Mechanics and Engineering, Vol. 57, pp. 297–367 (1986).

[73] I. Goryacheva, F. Sadeghi, Contact characteristics of a rolling/sliding cylinder and a viscoelastic layer bonded to an elastic substrate, Wear, Vol. 184, pp. 125–132 (1995).

[74] N. V. Brilliantov, T. Pöschel, Rolling friction of a viscous sphere on a hard plane, Europhysics Letters, Vol. 42, pp. 511–516 (1998).

[75] N. V. Brilliantov, T. Pöschel, Rolling as a "continuing collision", European Physical Journal B, Vol. 12, pp. 299–301 (1999).

[76] T. Pöschel, T. Schwager, N. V. Brilliantov, Rolling friction of a hard cylinder on a viscous plane, European Physical Journal B, Vol. 10, pp. 169–174 (1999).

[77] J. Tomlinson, A molecular theory of friction, The London, Edinburgh, and Dublin Philosophical Magazine and Journal of Science, Vol. 7, pp. 905–939 (1929).

[78] A. Doménech, T. Doménech, J. Cebrián, Introduction to the study of rolling friction, American Journal of Physics, Vol. 55, pp. 231–235 (1987).

[79] J. C. Charmet, M. Barquins, Adhesive contact and rolling of a rigid cylinder under the pull of gravity on the underside of a smooth-surfaced sheet of rubber, International Journal of Adhesion and Adhesives, Vol. 16, pp. 249–254 (1996).

[80] F. Robbe-Valloire, M. Barquins, Adhesive contact and kinetics of adherence between a rigid cylinder and an elastomeric solid, International Journal of Adhesion and Adhesives, Vol. 18, pp. 29–34 (1998).

[81] S. Hao, L. M. Keer, Rolling Contact Between Rigid Cylinder and Semi-Infinite Elastic Body With Sliding and Adhesion, Journal of Tribology, Vol. 129, pp. 481–494 (2007).

[82] J. Ai, J. F. Chen, J. M. Rotter, J. Y. Ooi, Assessment of rolling resistance models in discrete element simulations, Powder Technology, Vol. 206, pp. 269–282 (2011).

[83] H. Y. Sohn, C. Moreland, The effect of particle size distribution on packing density, The Canadian Journal of Chemical Engineering, Vol. 46, pp. 162–167 (1968).

[84] N. H. Minh, Y. P. Cheng, A DEM investigation of the effect of particle-size distribution on one-dimensional compression, Geotechnique, Vol. 63, pp. 44–53 (2013).

[85] D. Liu, C. O'sullivan, J. A. H. Carraro, The influence of particle size distribution on the stress distribution in granular materials, Geotechnique, Vol. 73, pp. 250–264 (2023).

[86] C. Li, T. Honeyands, D. O'Dea, R. Moreno-Atanasio, The angle of repose and size segregation of iron ore granules: DEM analysis and experimental investigation, Powder Technology, Vol. 320, pp. 257–272 (2017).

[87] T. T. Vo, T. L. Vu, P. Mutabaruka, Effects of size polydispersity on segregation of spherical particles in rotating drum, European Physical Journal E, Vol. 44, pp. 1–10 (2021).

[88] Z. Zuo, J. Wang, X. Wu, S. Gong, J. Zhang, X. Lu, Segregation dynamics of the binary-size granular system in a split rotary drum, Powder Technology, Vol. 404, 117480 (2022).

[89] A. K. Jha, V. M. Puri, Percolation segregation of multi-size and multi-component particulate materials, Powder Technology, Vol. 197, pp. 274–282 (2010).

[90] Y. Yu, A. Westerlund, T. Paananen, H. Saxén, Inter-particle percolation segregation during burden descent in the blast furnace, ISIJ International, Vol. 51, pp. 1050–1056 (2011).

[91] T. B. Anderson, R. Jackson, Fluid mechanical description of fluidized beds: Equations of Motion, Industrial and Engineering Chemistry Fundamentals, Vol. 6, pp. 527–539 (1967).

[92] Y. Tsuji, T. Tanaka, T. Ishida, Lagrangian numerical simulation of plug flow of cohesionless particles in a horizontal pipe, Powder Technology, Vol. 71, pp. 239–250 (1992).

[93] J. A. Kuipers, K. J. V. Duin, F. P. V. Beckum, W. P. V. Swaaij, A numerical model of gas-fluidized beds, Chemical Engineering Science, Vol. 47, pp. 1913–1924 (1992).

[94] Y. Tsuji, T. Kawaguchi, T. Tanaka, Discrete particle simulation of two-dimensional fluidized bed, Powder Technology, Vol. 77, pp. 79–87 (1993).

[95] D. Gidaspow, Multiphase Flow and Fluidization: Continuum and Kinetic Theory Descriptions, Academic Press, 2012.

[96] T. Mikami, H. Kamiya, M. Horio, Numerical simulation of cohesive powder behavior in a fluidized bed, Chemical Engineering Science, Vol. 53, pp. 1927–1940 (1998).

[97] A. H. Park, H. Bi, J. R. Grace, Reduction of electrostatic charges in gas-solid fluidized beds, Chemical Engineering Science, Vol. 57, pp. 153–162 (2002).

[98] R. Jackson, The mechanics of fluidized beds, Trans. Instn. Chem. Engnr., Vol. 41, pp. 22–48 (1963).

[99] T. B. Anderson, R. Jackson, Fluid Mechanical Description of Fluidized Beds. Stability of State of Uniform Fluidization, Industrial and Engineering Chemistry Fundamentals, Vol. 7, pp. 12–21 (1968).

[100] D. A. Drew, Mathematical Modeling of Two-Phase Flow, Annual Review of Fluid Mechanics, Vol. 15, pp. 261–291 (1983).

[101] D. Gidaspow, J. Jung, R. K. Singh, Hydrodynamics of fluidization using kinetic theory: an emerging paradigm: 2002 Flour-Daniel lecture, Powder Technology, Vol. 148, pp. 123–141 (2004).

[102] A. Vakilzadeh, A. B. Sarvestani, R. Osloob, R. Kamali, Sensitivity analysis of kinetic theory of granular flow (KTGF) and mixture models in terms of involved elemental parameters for two-phase gas-solid flow, Particulate Science and Technology, Vol. 41, pp. 1156–1169 (2023).

[103] C. R. K. Windows-Yule, S. Benyahia, P. Toson, H. Che, A. L. Nicuşan, Numerical Modelling and Imaging of Industrial-Scale Particulate Systems: A Review of Contemporary Challenges and Solutions, KONA Powder and Particle Journal, 2025007 (2024).

[104] S. B. Savage, K. Hutter, The motion of a finite mass of granular material down a rough incline, Journal of Fluid Mechanics, Vol. 199, pp. 177–215 (1989).

[105] K. G. Anderson, R. Jackson, A comparison of the solutions of some proposed equations of motion of granular materials for fully developed flow down inclined planes, Journal of Fluid Mechanics, Vol. 241, pp. 145–168 (1992).

[106] O. Pouliquen, Scaling laws in granular flows down rough inclined planes, Physics of Fluids, Vol. 11, pp. 542–548 (1999).

[107] E. Lajeunesse, J. B. Monnier, G. M. Homsy, Granular slumping on a horizontal surface, Physics of Fluids, Vol. 17, 103302 (2005).

[108] S. Larsson, Particle Methods for Modelling Granular Material Flow, Doctoral thesis, Luleå University of Technology, 2019.

[109] Z. Lu, S. C. Negi, J. C. Jofriet, A Numerical Model for Flow of Granular Materials in Silos. Part 1: Model Development, Journal of Agricultural Engineering Research, Vol. 68, pp. 223–229 (1997).

[110] Q. Meng, J. C. Jofriet, S. C. Negi, Finite Element Analysis of Bulk Solids Flow: Part 1, Development of a Model Based on a Secant Constitutive Relationship, Journal of Agricultural Engineering Research, Vol. 67, pp. 141–150 (1997).

[111] T. Karlsson, M. Klisinski, K. Runesson, Finite element simulation of granular material flow in plane silos with complicated geometry, Powder Technology, Vol. 99, pp. 29–39 (1998).

[112] S. A. Elaskar, L. A. Godoy, D. D. Gray, J. M. Stiles, A viscoplastic approach to model the flow of granular solids, International Journal of Solids and Structures, Vol. 37, pp. 2185–2214 (2000).

[113] E. Gallego, A. Ruiz, P. J. Aguado, Simulation of silo filling and discharge using ANSYS and comparison with experimental data, Computers and Electronics in Agriculture, Vol. 118, pp. 281–289 (2015).

[114] Q. J. Zheng, A. B. Yu, Finite element investigation of the flow and stress patterns in conical hopper during discharge, Chemical Engineering Science, Vol. 129, pp. 49–57 (2015).

[115] J. M. Rotter, J. M. Holst, J. Y. Ooi, A. M. Sanad, Silo pressure predictions using discrete-element and finite-element analyses, Philosophical Transactions of the Royal Society A: Mathematical, Physical and Engineering Sciences, Vol. 356, pp. 2685–2712 (1998).

[116] J. M. F. G. Holst, J. Y. Ooi, J. M. Rotter, G. H. Rong, Numerical Modeling of Silo Filling. I: Continuum Analyses, Journal of Engineering Mechanics, Vol. 125, pp. 94–103 (1999).

[117] S. Masson, J. Martinez, Effect of particle mechanical properties on silo flow and stresses from distinct element simulations, Powder Technology, Vol. 109, pp. 164–178 (2000).

[118] P. A. Langston, M. A. Al-Awamleh, F. Y. Fraige, B. N. Asmar, Distinct element modelling of non-spherical frictionless particle flow, Chemical Engineering Science, Vol. 59, pp. 425–435 (2004).

[119] R. Kobyłka, M. Molenda, DEM modelling of silo load asymmetry due to eccentric filling and discharge, Powder Technology, Vol. 233, pp. 65–71 (2013).

[120] Y. Forterre, O. Pouliquen, Flows of dense granular media, Annual Review of Fluid Mechanics, Vol. 40, pp. 1–24 (2008).

[121] J. D. Goddard, Continuum modeling of granular media, Applied Mechanics Reviews, Vol. 66, 050801 (2014).

[122] P. A. Cundall, O. D. Strack, A discrete numerical model for granular assemblies, Geotechnique, Vol. 29, pp. 47–65 (1979).

[123] S. Luding, Cohesive, frictional powders: Contact models for tension, Granular Matter, Vol. 10, pp. 235–246 (2008).

[124] A. Gladkyy, R. Schwarze, Comparison of different capillary bridge models for application in the discrete element method, Granular Matter, Vol. 16, pp. 911–920 (2014).

[125] J. P. Wang, X. Li, H. S. Yu, A micro–macro investigation of the capillary strengthening effect in wet granular materials, Acta Geotechnica, Vol. 13, pp. 513–533 (2018).

[126] S. Roy, M. Y. Shaheen, T. Pöschel, Effect of cohesion on structure of powder layers in additive manufacturing, Granular Matter, Vol. 25, pp. 1–13 (2023).

[127] R. Beetstra, M. A. van der Hoef, J. A. Kuipers, Numerical study of segregation using a new drag force correlation for polydisperse systems derived from lattice-Boltzmann simulations, Chemical Engineering Science, Vol. 62, pp. 246–255 (2007).

[128] R. L. Stewart, J. Bridgwater, Y. C. Zhou, A. B. Yu, Simulated and measured flow of granules in a bladed mixer—A detailed comparison, Chemical Engineering Science, Vol. 56, pp. 5457–5471 (2001).

[129] Y. Li, Y. Xu, C. Thornton, A comparison of discrete element simulations and experiments for 'sandpiles' composed of spherical particles, Powder Technology, Vol. 160, pp. 219–228 (2005).

[130] Y. Muguruma, T. Tanaka, Y. Tsuji, Numerical simulation of particulate flow with liquid bridge between particles (simulation of centrifugal tumbling granulator), Powder Technology, Vol. 109, pp. 49–57 (2000).

[131] P. Lambert, A. Chau, A. Delchambre, S. Régnier, Comparison between two capillary forces models, Langmuir, Vol. 24, pp. 3157–3163 (2008).

[132] A. J. Goldman, R. G. Cox, H. Brenner, Slow viscous motion of a sphere parallel to a plane wall-I Motion through a quiescent fluid, Chemical Engineering Science, Vol. 22, pp. 637–651 (1967).

[133] B. V. Derjaguin, V. M. Muller, Y. P. Toporov, Effect of contact deformations on the adhesion of particles, Progress in Surface Science, Vol. 45, pp. 131–143 (1994).

[134] D. Maugis, Adhesion of spheres: The JKR-DMT transition using a dugdale model, Journal of Colloid And Interface Science, Vol. 150, pp. 243–269 (1992).

[135] B. K. Mishra, C. Thornton, Impact breakage of particle agglomerates, International Journal of Mineral Processing, Vol. 61, pp. 225–239 (2001).

[136] A. Hassanpour, S. J. Antony, M. Ghadiri, Effect of size ratio on the behaviour of agglomerates embedded in a bed of particles subjected to shearing: DEM analysis, Chemical Engineering Science, Vol. 62, pp. 935–942 (2007).

[137] J. Yang, C. Y. Wu, M. Adams, DEM analysis of the effect of electrostatic interaction on particle mixing for carrier-based dry powder inhaler formulations, Particuology, Vol. 23, pp. 25–30 (2015).

[138] C. Pei, C. Y. Wu, M. Adams, DEM-CFD analysis of contact electrification and electrostatic interactions during fluidization, Powder Technology, Vol. 304, pp. 208–217 (2016).

[139] C. Bierwisch, T. Kraft, H. Riedel, M. Moseler, Three-dimensional discrete element models for the granular statics and dynamics of powders in cavity filling, Journal of the Mechanics and Physics of Solids, Vol. 57, pp. 10–31 (2009).

[140] T. Roessler, A. Katterfeld, Scaling of the angle of repose test and its influence on the calibration of DEM parameters using upscaled particles, Powder Technology, Vol. 330, pp. 58–66 (2018).

[141] M. Jiang, W. Zhang, DEM analyses of shear band in granular materials, Engineering Computations (Swansea, Wales), Vol. 32, pp. 985–1005 (2015).

[142] H. Tang, X. Zhang, X. Chu, DEM Simulation for the Effect of Rolling Resistance on Shear Band, Applied Mechanics and Materials, Vol. 204-208, pp. 246–249 (2012).

[143] C. M. Wensrich, A. Katterfeld, Rolling friction as a technique for modelling particle shape in DEM, Powder Technology, Vol. 217, pp. 409–417 (2012).

[144] Y. C. Zhou, B. D. Wright, R. Y. Yang, B. H. Xu, A. B. Yu, Rolling friction in the dynamic simulation of sandpile formation, Physica A: Statistical Mechanics and its Applications, Vol. 269, pp. 536–553 (1999).

[145] K. Iwashita, M. Oda, Rolling Resistance at Contacts in Simulation of Shear Band Development by DEM, Journal of Engineering Mechanics, Vol. 124, pp. 285–292 (1998).

[146] M. J. Jiang, H. S. Yu, D. Harris, A novel discrete model for granular material incorporating rolling resistance, Computers and Geotechnics, Vol. 32, pp. 340–357 (2005).

[147] J. Feng, H. H. Hu, D. D. Joseph, Direct simulation of initial value problems for the motion of solid bodies in a Newtonian fluid Part 1. Sedimentation, Journal of Fluid Mechanics, Vol. 261, pp. 95–134 (1994).

[148] K. J. Berger, C. M. Hrenya, Challenges of DEM: II. Wide particle size distributions, Powder Technology, Vol. 264, pp. 627–633 (2014).

[149] Y. He, T. J. Evans, A. B. Yu, R. Y. Yang, A GPU-based DEM for modelling large scale powder compaction with wide size distributions, Powder Technology, Vol. 333, pp. 219–228 (2018).

[150] Y. Zhao, R. A. Cocco, S. Yang, J. W. Chew, DEM Study on the effect of particle-size distribution on jamming in a 3D conical hopper, AIChE Journal, Vol. 65, pp. 512–519 (2019).

[151] J. G. Qian, W. Y. Li, Z. Y. Yin, Y. Yang, Influences of buried depth and grain size distribution on seepage erosion in granular soils around tunnel by coupled CFD-DEM approach, Transportation Geotechnics, Vol. 29, 100574 (2021).

[152] L. L. Zhao, C. L. Duan, H. S. Jiang, H. X. Li, Y. M. Zhao, Q. J. Zheng, DEM simulation of size segregation of binary mixtures of cohesive particles under a horizontal swirling vibration, Powder Technology, Vol. 404, 117456 (2022).

[153] Y. Xie, J. Yang, X. Zheng, T. Qu, C. Zhang, J. Fu, Effect of Particle Size Distributions (PSDs) on ground responses induced by tunnelling in dense coarse-grained soils: A DEM investigation, Computers and Geotechnics, Vol. 163, 105763 (2023).

[154] Y. Hu, E. L. Chan, J. ichi Watanabe, M. Takezawa, T. Tsuji, T. Tanaka, K. Washino, Inter-particle torque scaling in coarse grained DEM with rolling resistance and particle size distributions, Powder Technology, Vol. 438, 119612 (2024).

[155] N. Govender, D. N. Wilke, C. Y. Wu, R. Rajamani, J. Khinast, B. J. Glasser, Large-scale GPU based DEM modeling of mixing using irregularly shaped particles, Advanced Powder Technology, Vol. 29, pp. 2476–2490 (2018).

[156] Y. He, F. Muller, A. Hassanpour, A. E. Bayly, A CPU-GPU cross-platform coupled CFD-DEM approach for complex particle-fluid flows, Chemical Engineering Science, Vol. 223, 115712 (2020).

[157] C. Zheng, L. Li, B. J. Nitert, N. Govender, T. Chamberlain, L. Zhang, C. Y. Wu, Investigation of granular dynamics in a continuous blender using the GPU-enhanced discrete element method, Powder Technology, Vol. 412, 117968 (2022).

[158] T. Tsuji, K. Yabumoto, T. Tanaka, Spontaneous structures in three-dimensional bubbling gas-fluidized bed by parallel DEM-CFD coupling simulation, Powder Technology, Vol. 184, pp. 132–140 (2008).

[159] H. Mio, R. Higuchi, W. Ishimaru, A. Shimosaka, Y. Shirakawa, J. Hidaka, Effect of paddle rotational speed on particle mixing behavior in electrophotographic system by using parallel discrete element method, Advanced Powder Technology, Vol. 20, pp. 406–415 (2009).

[160] T. Kobayashi, T. Tanaka, N. Shimada, T. Kawaguchi, DEM-CFD analysis of fluidization behavior of Geldart Group A particles using a dynamic adhesion force model, Powder Technology, Vol. 248, pp. 143–152 (2013).

[161] K. Washino, E. L. Chan, T. Tanaka, DEM with attraction forces using reduced particle stiffness, Powder Technology, Vol. 325, pp. 202–208 (2018).

[162] S. Chen, W. Liu, S. Li, A fast adhesive discrete element method for random packings of fine particles, Chemical Engineering Science, Vol. 193, pp. 336–345 (2019).

[163] Y. He, A. Hassanpour, M. A. Behjani, A. E. Bayly, A novel stiffness scaling methodology for discrete element modelling of cohesive fine powders, Applied Mathematical Modelling, Vol. 90, pp. 817–844 (2021).

[164] K. Washino, S. Nakae, R. Yamagami, E. L. Chan, T. Tsuji, T. Tanaka, Scaling of attraction force and rolling resistance in DEM with reduced particle stiffness, Chemical Engineering Research and Design, Vol. 203, pp. 501–519 (2024).

[165] M. Sakai, S. Koshizuka, Large-scale discrete element modeling in pneumatic conveying, Chemical Engineering Science, Vol. 64, pp. 533–539 (2009).

[166] M. Sakai, H. Takahashi, C. C. Pain, J. P. Latham, J. Xiang, Study on a large-scale discrete element model for fine particles in a fluidized bed, Advanced Powder Technology, Vol. 23, pp. 673–681 (2012).

[167] M. Sakai, M. Abe, Y. Shigeto, S. Mizutani, H. Takahashi, A. Viré, J. R. Percival, J. Xiang, C. C. Pain, Verification and validation of a coarse grain model of the DEM in a bubbling fluidized bed, Chemical Engineering Journal, Vol. 244, pp. 33–43 (2014).

[168] S. C. Thakur, J. Y. Ooi, H. Ahmadian, Scaling of discrete element model parameters for cohesionless and cohesive solid, Powder Technology, Vol. 293, pp. 130–137 (2016).

[169] K. Chu, J. Chen, A. Yu, Applicability of a coarse-grained CFD−DEM model on dense medium cyclone, Minerals Engineering, Vol. 90, pp. 43–54 (2016).

[170] K. Takabatake, Y. Mori, J. G. Khinast, M. Sakai, Numerical investigation of a coarse-grain discrete element method in solid mixing in a spouted bed, Chemical Engineering Journal, Vol. 346, pp. 416–426 (2018).

[171] P. M. Widartiningsih, Y. Mori, K. Takabatake, C. Y. Wu, K. Yokoi, A. Yamaguchi, M. Sakai, Coarse graining DEM simulations of a powder die-filling system, Powder Technology, Vol. 371, pp. 83–95 (2020).

[172] H. Che, D. Werner, J. Seville, T. K. Wheldon, K. Windows-Yule, Evaluation of coarse-grained CFD-DEM models with the validation of PEPT measurements, Particuology, Vol. 82, pp. 48–63 (2023).

[173] E. L. Chan, K. Washino, Coarse grain model for DEM simulation of dense and dynamic particle flow with liquid bridge forces, Chemical Engineering Research and Design, Vol. 132, pp. 1060–1069 (2018).

[174] Z. Jiang, K. Rai, T. Tsuji, K. Washino, T. Tanaka, J. Oshitani, Upscaled DEM-CFD model for vibrated fluidized bed based on particle-scale similarities, Advanced Powder Technology, Vol. 31, pp. 4598–4618 (2020).

[175] Y. Kosaku, Y. Tsunazawa, C. Tokoro, A coarse grain model with parameter scaling of adhesion forces from liquid bridge forces and JKR theory in the discrete element method, Chemical Engineering Science, Vol. 268, 118428 (2023).

[176] K. Washino, E. L. Chan, T. Kaji, Y. Matsuno, T. Tanaka, On large scale CFD-DEM simulation for gas-liquid-solid three-phase flows, Particuology, Vol. 59, pp. 2–15 (2021).

[177] Y. Hu, E. L. Chan, T. Tsuji, T. Tanaka, K. Washino, Geometric similarity on interparticle force evaluation for scaled-up DEM particles, Powder Technology, Vol. 404, 117483 (2022).

[178] K. Washino, E. L. Chan, Y. Nishida, T. Tsuji, Coarse grained DEM simulation of non-spherical and poly-dispersed particles using Scaled-Up Particle (SUP) model, Powder Technology, Vol. 426, 118676 (2023).

[179] B. J. Alder, T. E. Wainwright, Phase Transition for a Hard Sphere System, The Journal of Chemical Physics, Vol. 27, pp. 1208–1209 (1957).

[180] C. S. Campbell, C. E. Brennen, Computer simulation of granular shear flows, Journal of Fluid Mechanics, Vol. 151, pp. 167–188 (1985).

[181] P. Kosinski, B. V. Balakin, A. Kosinska, Extension of the hard-sphere model for particle-flow simulations, Physical Review E, Vol. 102, 022909 (2020).

[182] W. J. Stronge, Impact Mechanics: Second Edition, Cambridge University Press, 2018.

[183] W. J. Stronge, Smooth dynamics of oblique impact with friction, International Journal of Impact Engineering, Vol. 51, pp. 36–49 (2013).

[184] S. Djerassi, Collision with friction; Part A: Newton's hypothesis, Multibody System Dynamics, Vol. 21, pp. 37–54 (2009).

[185] S. Djerassi, Collision with friction; Part B: Poisson's and Stornge's hypotheses, Multibody System Dynamics, Vol. 21, pp. 55–70 (2009).

[186] R. M. Brach, Friction, Restitution, and Energy Loss in Planar Collisions, Journal of Applied Mechanics, Transactions ASME, Vol. 51, pp. 164–170 (1984).

[187] R. M. Brach, Rigid Body Collisions, Journal of Applied Mechanics, Transactions ASME, Vol. 56, pp. 133–138 (1989).

[188] J. B. Keller, Impact With Friction, Journal of Applied Mechanics, Transactions ASME, Vol. 53, pp. 1–4 (1986).

[189] S. F. Foerster, M. Y. Louge, H. Chang, K. Allia, Measurements of the collision properties of small spheres, Physics of Fluids, Vol. 6, pp. 1108–1115 (1994).

[190] B. P. Hoomans, J. A. Kuipers, W. J. Briels, W. P. V. Swaaij, Discrete particle simulation of bubble and slug formation in a two-dimensional gas-fluidised bed: A hard-sphere approach, Chemical Engineering Science, Vol. 51, pp. 99–118 (1996).

[191] P. Kosinski, A. C. Hoffmann, Extension of the hard-sphere particle-wall collision model to account for particle deposition, Physical Review E, Vol. 79, 061302 (2009).

[192] J. Shäfer, S. Dippel, D. E. Wolf, Force Schemes in Simulations of Granular Materials, Journal de Physique I, Vol. 6, pp. 5–20 (1996).

[193] A. B. Stevens, C. M. Hrenya, Comparison of soft-sphere models to measurements of collision properties during normal impacts, Powder Technology, Vol. 154, pp. 99–109 (2005).

[194] W. Goldsmith, J. T. Frasier, Impact: The Theory and Physical Behavior of Colliding Solids, Journal of Applied Mechanics, Vol. 28, pp. 639–639 (1961).

[195] X. Deng, J. V. Scicolone, R. N. Davé, Discrete element method simulation of cohesive particles mixing under magnetically assisted impaction, Powder Technology, Vol. 243, pp. 96–109 (2013).

[196] E. J. Parteli, J. Schmidt, C. Blümel, K. E. Wirth, W. Peukert, T. Pöschel, Attractive particle interaction forces and packing density of fine glass powders, Scientific Reports, Vol. 4, pp. 1–7 (2014).

[197] C. Thornton, Interparticle sliding in the presence of adhesion, Journal of Physics D: Applied Physics, Vol. 24, pp. 1942–1946 (1991).

[198] J. S. Marshall, Discrete-element modeling of particulate aerosol flows, Journal of Computational Physics, Vol. 228, pp. 1541–1561 (2009).

[199] M. L. Anderson, A. P. Bassom, N. Fowkes, Exact solutions of the Laplace-Young equation, Proceedings of the Royal Society A: Mathematical, Physical and Engineering Sciences, Vol. 462, pp. 3645–3656 (2006).

[200] R. A. Fisher, On the capillary forces in an ideal soil; correction of formulae given by W. B. Haines, The Journal of Agricultural Science, Vol. 16, pp. 492–505 (1926).

[201] C. D. Willett, M. J. Adams, S. A. Johnson, J. P. Seville, Capillary Bridges between Two Spherical Bodies, Langmuir, Vol. 16, pp. 9396–9405 (2000).

[202] L. Yang, M. Sega, J. Harting, Capillary-bridge forces between solid particles: Insights from lattice Boltzmann simulations, AIChE Journal, Vol. 67, e17350 (2021).

[203] D. Tabor, Surface forces and surface interactions, Journal of Colloid And Interface Science, Vol. 58, pp. 2–13 (1977).

[204] M. Pasha, C. Hare, A. Hassanpour, M. Ghadiri, Analysis of ball indentation on cohesive powder beds using distinct element modelling, Powder Technology, Vol. 233, pp. 80–90 (2013).

[205] C. Goniva, C. Kloss, N. G. Deen, J. A. Kuipers, S. Pirker, Influence of rolling friction on single spout fluidized bed simulation, Particuology, Vol. 10, pp. 582–591 (2012).

[206] K. Samiei, Implicit and explicit algorithms in discrete element method, Lambert Academic Publishing, 2014.

[207] W. C. Swope, H. C. Andersen, P. H. Berens, K. R. Wilson, A computer simulation method for the calculation of equilibrium constants for the formation of physical clusters of molecules: Application to small water clusters, The Journal of Chemical Physics, Vol. 76, pp. 637–649 (1982).

[208] A. E. Sáez, C. J. Otero, I. Rusinek, The effective homogeneous behavior of heterogeneous porous media, Transport in Porous Media, Vol. 4, pp. 213–238 (1989).

[209] A. Bourgeat, M. Jurak, A two level scaling-up method for multiphase flow in porous media; numerical validation and comparison with other methods, Computational Geosciences, Vol. 14, pp. 1–14 (2010).

[210] R. Sun, H. Xiao, Diffusion-based coarse graining in hybrid continuum-discrete solvers: Applications in CFD-DEM, International Journal of Multiphase Flow, Vol. 72, pp. 233–247 (2015).

[211] J. S. Ramaker, M. A. Jelgersma, P. Vonk, N. W. Kossen, Scale-down of a high-shear pelletisation process: Flow profile and growth kinetics, International Journal of Pharmaceutics, Vol. 166, pp. 89–97 (1998).

[212] E. L. Chan, K. Washino, G. K. Reynolds, B. Gururajan, M. J. Hounslow, A. D. Salman, Blade-granule bed stress in a cylindrical high shear granulator: Further characterisation using DEM, Powder Technology, Vol. 300, pp. 92–106 (2016).

[213] H. M. B. Al-Hashemi, O. S. B. Al-Amoudi, A review on the angle of repose of granular materials, Powder Technology, Vol. 330, pp. 397–417 (2018).